Electrodéposition et la caractérisation de nanofilms palladium sur Au (111) pour le stockage d'hydrogène Electro-deposition and characterization of palladium nanofilms on Au (111) for hydrogen storage

Liang Wang

UNIVERSITÉ DE GRENOBLE

THÈSE

Pour obtenir le grade de

DOCTEUR DE GRENOBLE-INP

Spécialité : **Matériaux, Mécanique, Génie Civil, Électrochimie**

Arrêté ministériel : 7 août 2006

Présentée par

Liang WANG

Thèse dirigée par **Yvonne Soldo-Olivier**
codirigée par **Eric Sibert**
préparée au sein du **Laboratoire d'Electrochimie et de Physico-chimie des Matériaux et des Interfaces**
dans l'**École Doctorale Ingénierie-Matériau Mécanique Énergétique Environnement procédés Production**

Électrodéposition et caractérisation de nanofilms de palladium sur Au(111) pour le stockage d'hydrogène

Electro-deposition and characterization of palladium nanofilms on Au(111) for hydrogen storage

Thèse soutenue publiquement le **21 Décembre 2012**, devant le jury composé de :

M. Ricardo NOGUEIRA
Professeur à Grenoble-INP, Président

M. Pierre MILLET
Professeur à l'Université de Paris Sud XI, Rapporteur

M. Thierry PAUPORTE
Directeur de Recherche CNRS, ENSCP, Paris, Rapporteur

M. Emmanuel MAISONHAUTE
Professeur à l'Université Pierre et Marie Curie, Paris, Examinateur

Mme. Yvonne SOLDO-OLIVIER
Chargée de Recherche CNRS, Directrice de thèse

M. Eric SIBERT
Chargé de Recherche CNRS, Co-directeur de thèse

Résumé en français

I.1 Introduction

Avec le développement de la société humaine, la demande en énergie a drastiquement augmenté durant les dernières décennies. Malheureusement, les ressources fossiles ne constituent pas une énergie renouvelable. La limitation des réserves de combustibles fossiles impose le recours à des énergies alternatives, comme les énergies renouvelables (solaire, géothermie, vent, hydroélectricité,…), l'énergie nucléaire dans ses versions les plus avancées (Génération IV) ou la fusion contrôlée. La combustion de combustibles fossiles induit par ailleurs de graves pollutions de l'environnement. Durant ces dernières années, la concentration en CO_2 de l'atmosphère n'a pas cessé d'augmenter, conduisant à un réchauffement global. Le SO_2, la suie, les poussières produites industriellement, les oxydes d'azote et la pollution due au pétrole représentent d'autres sources majeures de contamination.

Actuellement il y a deux stratégies différentes pour le développement énergétique mondial :

- satisfaire la demande croissante en énergie de la population mondiale, population qui aspire naturellement à son développement social et économique. Avec le taux actuel de croissance, le temps de doublement de la consommation énergétique mondiale est d'environ 50 ans.

- diminuer les émissions humaines polluantes en développant des ressources énergétiques respectueuses de l'environnement. L'activité humaine libère en ce moment deux fois plus de CO_2 que la nature ne peut en absorber.

Dans ce contexte, la recherche de vecteurs d'énergie autre que le courant électrique et la chaleur, capable de produire un stockage massif et un transport économique sur des grandes distances, est d'importance primordiale. En effet, le courant électrique ne peut pas être la seule source d'énergie, à cause de ses coûts de transport et de distribution importants. De plus, actuellement, il n'y a pas de stockage massif pour cette forme d'énergie.

Pour toutes ces raisons, l'hydrogène, qui peut être converti en électricité et chaleur grâce aux piles à combustibles, aura un rôle très important dans le futur énergétique de notre planète.

William Grove a proposé le premier en 1839 le concept de pile à combustible [1], processus dans lequel la conversion de flux d'hydrogène et oxygène en eau est accompagnée par la production d'électricité. L'efficacité de conversion théorique est égal à 83%, une valeur largement supérieure à celle du moteur thermique, sujet aux limitations du cycle de Carnot [2]. Néanmoins, deux problèmes majeurs doivent être résolus pour pouvoir utiliser l'hydrogène comme vecteur d'énergie sur large échelle.

Le premier est lié à sa production, pour laquelle les méthodes actuelles ne sont pas optimisées et sont encore très coûteuses. Même si l'hydrogène est abondant sur terre, il existe seulement sous la forme de composés et doit être extrait avant d'être utilisé. L'hydrogène pur peut être facilement obtenu par électrolyse de l'eau, mais ce processus est caractérisé par une efficacité médiocre et une grande consommation d'énergie. Par exemple, la production d'hydrogène par électrolyse de l'eau nécessaire pour l'ensemble de véhicules en circulation en France représenterait la quantité d'électricité totale consommé par la France [3]. La décomposition de l'eau par électrolyse ou par réaction chimique à haute température et la décomposition thermochimique de la biomasse sont des sujets de recherches en plein essor.

Le deuxième problème à surmonter pour l'utilisation généralisée de l'hydrogène comme vecteur d'énergie est son stockage. L'hydrogène, dans sa phase gazeuse, est inflammable et explosif. Les problèmes liés à la sécurité pendant le stockage et le transport doivent être résolus. Le stockage à haute pression (> 350 bar) a vu le développement de réservoirs composites (fibres de carbone et polymères), plus légers que les réservoirs métalliques. Néanmoins, le problème de la compression au-delà de 350 bars reste d'actualité, à cause de l'important coût de cette opération (25% de la capacité de stockage perdu par rapport à la compression d'un gaz idéal) [3]. Le stockage de l'hydrogène liquide (hydrogène gazeux refroidi à -253 ^{0}C) nécessite d'excellents dispositifs d'isolation pour éviter la vaporisation.

L'adsorption de l'hydrogène (adsorption physique et chimique) représente une autre technologie potentiellement plus sûre et très efficace, dans laquelle des nanomatériaux comme les nanotubes de carbone [4,5] et les carbonitrures [6] sont utilisés comme adsorbants.

Les hydrures chimiques [7] sont aussi étudiés. Ils sont caractérisés par des liaisons chimiques avec l'hydrogène [8] ioniques (NaH, CaH_2,…) ou covalentes (CH_4,…). Nous devons citer aussi les matériaux organométalliques, constitués par des ions ou des clusters métalliques coordonnés à des molécules organiques [9,10,11].

Les hydrures métalliques (alliages métal-hydrogène), capable d'absorber l'hydrogène de manière réversible, offrent une autre option intéressante. Plusieurs hydrures métalliques à haute capacité de stockage ont été testés ($LaNi_5$ [12], TiNi [13], $NaAlH_4$ [14],…). La densité d_H de l'hydrogène stocké par unité de volume peut être 1000 fois plus grande que pour l'hydrogène gazeux dans les mêmes conditions de température et pression, et peut même dépasser la densité de l'hydrogène liquide (c.à.d. d_H=96,7 $Kg \cdot m^{-3}$ dans $LiAlH_4$, d_H=70,8 $Kg \cdot m^{-3}$ dans l'hydrogène liquide) [15].

Néanmoins, le comportement physico-chimiques et les mécanismes d'insertion/désorption dans les hydrures métalliques restent un défi scientifique [16]. Plus spécifiquement, ces matériaux, et plus particulièrement les alliages à base de magnésium et les alanates [a], peuvent présenter une réactivité chimique importante et devrons probablement être encapsulés [17,18,19, 20]. Une solution peut être la réalisation de dépôts nanometric sur ces alliages [21]. Cette technologie est d'autant plus intéressante qu'elle recouvre plusieurs autres applications, comme les verres optiques fonctionnels [22, 23], de nouveaux types d'électrodes [24] ou les detecteurs de gaz [25,26].

Dans ce contexte, les films ultra minces de palladium déposés sur une surface monocristalline représentent un modèle intéressant non seulement pour étudier les propriétés du Pd vis-à-vis de l'insertion/désinsertion de l'hydrogène à l'échelle nanométrique, qui peut révéler des propriétés originales par rapport au palladium massif, mais aussi en considérant le caractère monocristallin du film, qui élimine les joints de grains et ainsi les courts-circuits de diffusion.

Le system palladium–hydrogène a été très étudié parmi les différents hydrures disponibles [27,28]. Grâce à ses propriétés mécaniques, sa grande capacité d'absorption et sa

[a] Les **Alanates** sont des composés qui contiennent de l'aluminium, de l'hydrogène (stocké) et un métal comme le sodium ou le lithium.

haute pureté, le palladium est souvent utilisé comme modèle pour l'étude des propriétés thermodynamiques et cinétiques des systèmes métal-hydrogène ou des alliages intermétalliques. Le rôle catalytique (dissociation du dihydrogène) et la cinétique rapide pour l'insertion/désinsertion de l'hydrogène représentent aussi un vrai atout.

L'étude que nous présentons concerne l'élaboration et la caractérisation de films de Pd sur Au(111) et l'électro-insertion de l'hydrogène dans ceux-ci. Le chapitre I porte sur l'étude bibliographique. Dans le chapitre II nous discutons les résultats obtenus sur le dépôt électrochimique et la caractérisation des films Pd/Au(111). Le chapitre III concerne l'étude des mécanismes de croissance, en particulier pour la première couche UPD (Under Potential Deposition) de Pd. Des expériences sur des transitoires de courant et des mesures de diffraction de surface de rayons X *in situ* sont discutées. Le dernier chapitre est dédié à la détermination expérimentale des isothermes d'insertion électrochimique pour des dépôts de Pd de différentes épaisseurs.

I.2 Isothermes électrochimiques du système H-$Pd_{x\ MC}$/Au(111)

Notre objectif global est d'étudier l'effet de différents paramètres sur l'insertion d'hydrogène dans le Pd. Nous nous concentrons principalement sur les nanofilms de Pd déposés sur différents substrats bien définis et plus particulièrement sur Au(111) dans la présente étude. Même dans ce cas particulier, nous pourrions observer plusieurs comportements pour différentes épaisseurs de film. Les isothermes d'insertion de l'hydrogène sont un outil puissant pour de telles études. En phase gaz, elles décrivent la quantité d'hydrogène inséré dans Pd suivant la pression appliquée de H_2. Cette quantité est habituellement exprimée comme un rapport entre le nombre d'atomes d'hydrogène et de palladium : H/Pd. Elle est sensible à la température. En milieu électrochimique, la pression de H_2 est remplacée par le potentiel électrochimique. L'électro-insertion d'hydrogène présente de nombreux avantages comme le faible coût des équipements électrochimiques, des gains de temps grâce à des réponses courant-tension rapides mais aussi une meilleure sécurité en l'absence de hautes pressions [29]. Grâce à une relation bien établie entre le potentiel électrochimique et la pression partielle d'hydrogène [1], il est possible de déduire l'isotherme en phase gaz de celle mesurée par voie électrochimique [30] . Nous avons mesuré des isothermes statiques, où chaque point correspond à un état d'équilibre du système Pd-H au potentiel choisi.

Nous allons commencer par un aperçu du comportement des nanofilms de Pd sur Au(111) en milieu acide pour identifier les caractéristiques qui pourraient être exploitée pour les mesurer les isothermes. La Figure I.1 montre le voltampérogramme de $Pd_{10\ MC}$/Au(111) dans 0.1 M H_2SO_4.

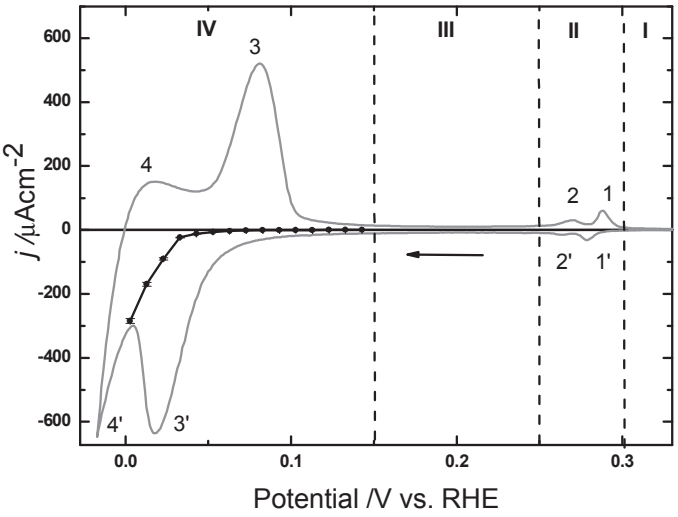

Figure I.1: Voltampérogramme de $Pd_{10\ MC}$/Au(111) dans 0,1 M H_2SO_4. Balayage : 10 mV·s^{-1}. L'évaluation du dégagement d'hydrogène est aussi présenté (cercles pleins avec la ligne noire), correspondant à la mesure du courant à l'état stationnaire suivant le potentiel appliqué.

Quatre régions peuvent être identifiées même si elles ne sont pas nécessairement séparées par des frontières strictes :

I Zone de double-couche.

II Hydrogène/(bi)sulfates adsorption/désorption associés à des arrangements d'anions en surface. Très sensible à la morphologie du dépôt et à la nature des couches de Pd en contact avec la solution (pics 1/1' : 2ème couche de Pd ; pics 2/2' :3ème et suivantes couches de Pd).

III Zone d'adsorption peu sensible à la morphologie et l'épaisseur du dépôt. Nous considérons qu'il s'agit d'adsorption d'hydrogène suivant une isotherme de Frumkin [31].

IV Zone d'absorption/desorption d'hydrogène. Il est important de noter que la réaction de dégagement d'hydrogène (HER : hydrogen evolution reaction) se superpose au processus d'insertion aux plus bas potentiels [32,33].

Afin d'estimer la contribution de l'HER, le courant a été mesuré pour différents potentiels, à l'état stationnaire, pour lequel la seule réaction faradique est le dégagement d'hydrogène (voir Figure I.1). La valeur du courant est quasi nulle au dessus de 0,02 V *vs.* ERH, indiquant que dans cette région de potentiel, le processus de dégagement d'hydrogène est négligeable. Ce n'est pas le cas pour les potentiels plus bas, où la contribution de l'HER doit être prise en compte. En suivant cette description, les pics 4/4' sont principalement dus à l'HER/HOR (hydrogen oxidation reaction : réaction d'oxydation de l'hydrogène) et les pics 3/3' sont majoritairement attribués à l'insertion/desorption de l'hydrogène. Alors que le pic 3' est clairement combiné avec le pic 4', le pic 3 de désorption de l'hydrogène est décalé vers de plus hauts potentiels, où le dégagement d'hydrogène peut être négligé. Pour cette raison, le balayage positif peut plus facilement être exploité pour évaluer la quantité d'hydrogène absorbé.

Finalement, le domaine de potentiel considéré pour les mesures d'isotherme s'étend de 0,153 V *vs.* ERH to 0 V *vs.* ERH. Nous ne pouvons quand même pas exclure un peu d'adsorption d'hydrogène dans la même gamme de potentiel. Ceci pourrait affecter marginalement le calcul du ratio H/Pd, particulièrement pour les films de Pd les plus fins.

Les branches d'absorption et de désorption ont été mesurées dans le même domaine de potentiel pour différentes épaisseurs de Pd et ont été comparées avec le Pd massif, les films Pd/Pt(111) et les nanoparticules de Pd.

I.2.1 **Mode opératoire**

Isotherme d'insertion électrochimique

La Figure I.2 montre schématiquement la procédure suivie pour déterminer la quantité d'hydrogène absorbée en fonction du potentiel appliqué.

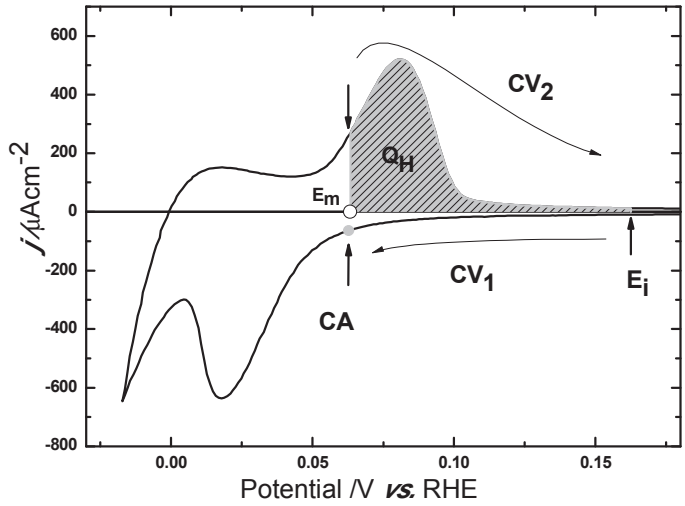

Figure I.2: Représentation schématique de la procédure suivie pour mesurer la branche d'insertion de l'isotherme d'insertion de l'hydrogène, 0,1 M H_2SO_4. Balayages à 10 mV·s^{-1}.

Après une caractérisation électrochimique dans 0,1 M H_2SO_4 et la région de potentiel [0,1 ; 0,4] V *vs.* ERH, le potentiel est initialement fixé dans la zone d'adsorption de l'hydrogène, E_i=0,15 V *vs.* ERH. Un balayage négatif (CV_1) est alors réalisé jusqu'au potentiel considéré pour la mesure de l'isotherme, E_m,. Le potentiel est maintenu (CA) jusqu'à l'obtention d'un état stationnaire.

La charge correspondant à la désorption de l'hydrogène est évaluée grâce à l'intégrale de la charge Q_H durant le balayage positif CV_2 où chaque électron transféré correspond à un atome d'hydrogène inséré :

$$Q_H = \int_{Em}^{E_i} \frac{i}{\nu} dE \qquad \text{Équation 1}$$

La Figure I.3 montre des balayages positifs typiques des courbes obtenues pour le calcul de l'isotherme d'absorption.

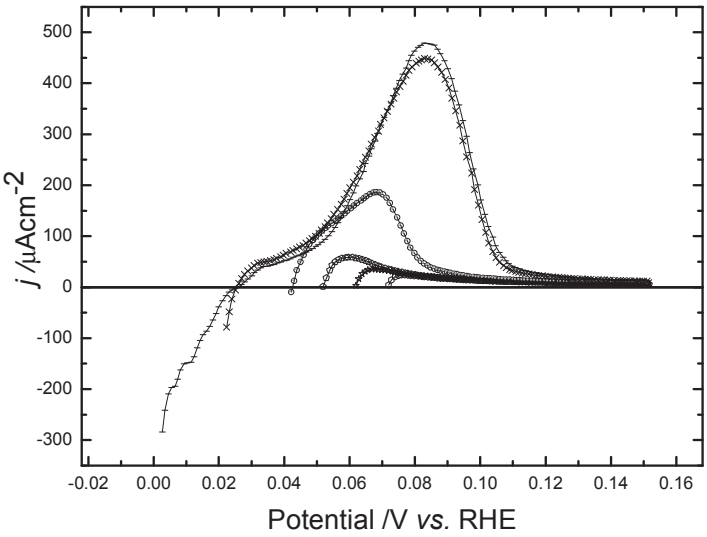

Figure I.3: Calcul de l'isotherme d'absorption : balayages positifs mesurés pour $Pd_{15\ MC}$/Au(111), 10 mV·s^{-1}.

Comme cela a déjà été discuté, le dégagement d'hydrogène joue un rôle de plus en plus important à mesure que le potentiel baisse sous les 0,02 V *vs.* ERH. Sa contribution est mise en relief sur la Figure I.1 par les courants négatifs. Afin de ne considérer que la charge associée au processus d'insertion de l'hydrogène, seul le domaine de courant positif est pris en compte pour le calcul de Q_H suivant l'équation 1.

Les points expérimentaux pour la détermination des isothermes sont pris tous les 10 mV. Afin de minimiser les interférences avec l'hydrogène gazeux, la solution est agitée durant les mesures [34].

Isotherme de désorption électrochimique

Nous rappelons que les isothermes comportent deux branches, une d'insertion et l'autre de désorption. Pour la mesure de la branche de désorption, le potentiel est initialement fixé dans la zone d'adsorption de l'hydrogène puis scanné négativement jusqu'à E_F=-0,02 V *vs.* ERH (CV_1), valeur en dessous de laquelle toute insertion ultérieure peut être considérée comme négligeable. Une fois l'état stationnaire atteint (CA_1), le potentiel est scanné positivement (CV_2) jusqu'au potentiel d'insertion considéré E_m, où il est de nouveau maintenu jusqu'à l'état stationnaire (CA_2). Q_H est alors évalué durant un nouveau balayage (CV_3) comme montré sur la Figure I.4.

Les points de la branche de désorption sont mesurés tous les 10 mV depuis le plus bas potentiel E_F jusqu'à 0,15 V *vs.* ERH. Comme pour la branche d'insertion, l'électrolyte est agité durant toutes les mesures.

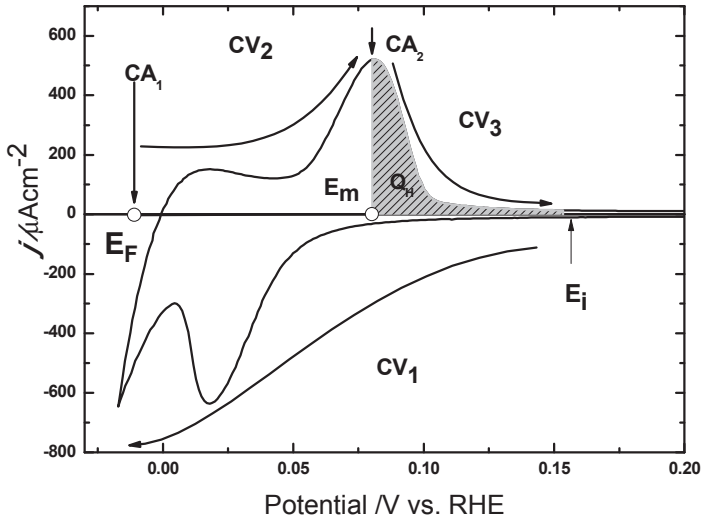

Figure I.4: Représentation schématique de la procédure suivie pour mesurer la branche de désorption de l'isotherme d'insertion de l'hydrogène, 0,1 M H_2SO_4. Balayages à 10 mV·s^{-1}.

I.2.2 **Résultats et discussion**

Isotherme dans Pd_{15MC}/Au(111)

La Figure I.5 montre l'isotherme complète d'un échantillon $Pd_{15\ MC}$/Au(111).

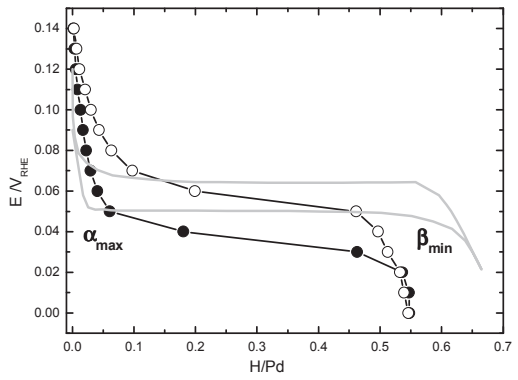

Figure I.5: Isotherme d'absorption électrochimique de l'hydrogène dans un échantillon de $Pd_{15\ MC}$/Au(111), 0,1 M H_2SO_4. Cercles pleins : branche d'insertion ; cercles creux : branche de désorption ; ligne grise : Pd massif [35].

Comparée à Pd massif, l'isotherme du film présente toujours le plateau bi-phasique mais il est plus petit et possède une pente. La capacité de stockage de l'hydrogène est plus petite $(H/Pd)_{max} \approx 0,55$. Les mêmes caractéristiques ont été trouvées pour les isothermes de H-Pd/Pt(111) et ont été attribuées aux contraintes provoquées par le substrat [7,36], qui induisent la présence de sites d'insertion non équivalents. À l'intérieur de cette description, les valeurs de α_{max} et β_{min} ne sont pas aussi bien définies que pour Pd massif. En fait, les limites entre les différentes régions (phase α, domaine bi-phasique, phase β) ne sont probablement pas bien marquées dans les films supportés de Pd, comme le suggère l'analogie avec le comportement de Pd/Pt(111). Les paramètres α_{max} and β_{min} n'ont probablement pas la même signification que pour Pd massif.

Pour cette raison, nous allons seulement décrire leurs tendances en fonction de différents paramètres (support, épaisseur…) mais nous ne réaliserons aucune interprétation quantitative. Comme le montre la Figure I.5, α_{max} semble être plus grand pour Pd_{15MC}/Au(111), correspond à un élargissement du domaine de la phase α dans les nano-films Pd/Au(111).

L'isotherme montre clairement la présence d'une hystérèse entre les branches d'insertion et de désorption. Les mesures sur des films plus minces montrent que l'hystérèse est présent jusqu'à des épaisseurs équivalentes à 5 MC. Ce résultat conforte l'idée que l'hystérèse ne dépend pas de l'épaisseur. Nos résultats sont en accord avec ceux de Pundt *et al.* [37], qui ont montré la présence d'hystérèse dans les mesures d'isothermes en phase gaz sur des nanoparticules de Pd de 3 nm de diamètre.

Influence de l'épaisseur sur la solubilité de l'hydrogène

La Figure I.6 compare les isothermes d'insertion obtenues pour des échantillons de différentes épaisseurs. Les taux d'insertion correspondent à la moyenne de plusieurs échantillons possédant la même épaisseur équivalente de Pd. Les barres d'erreur sont extraites de l'écart-type. Comme cela a été montré dans le chapitre III, seules les deux premières couches atomiques ont une croissance bidimensionnelle alors que les couches suivantes sont caractérisées par une croissance 3D. Ceci induit une moins bonne reproductibilité de la morphologie locale des films avec l'augmentation d'épaisseur, conduisant à des barres d'erreur plus importantes pour les échantillons les plus épais (10 MC et 15 MC).

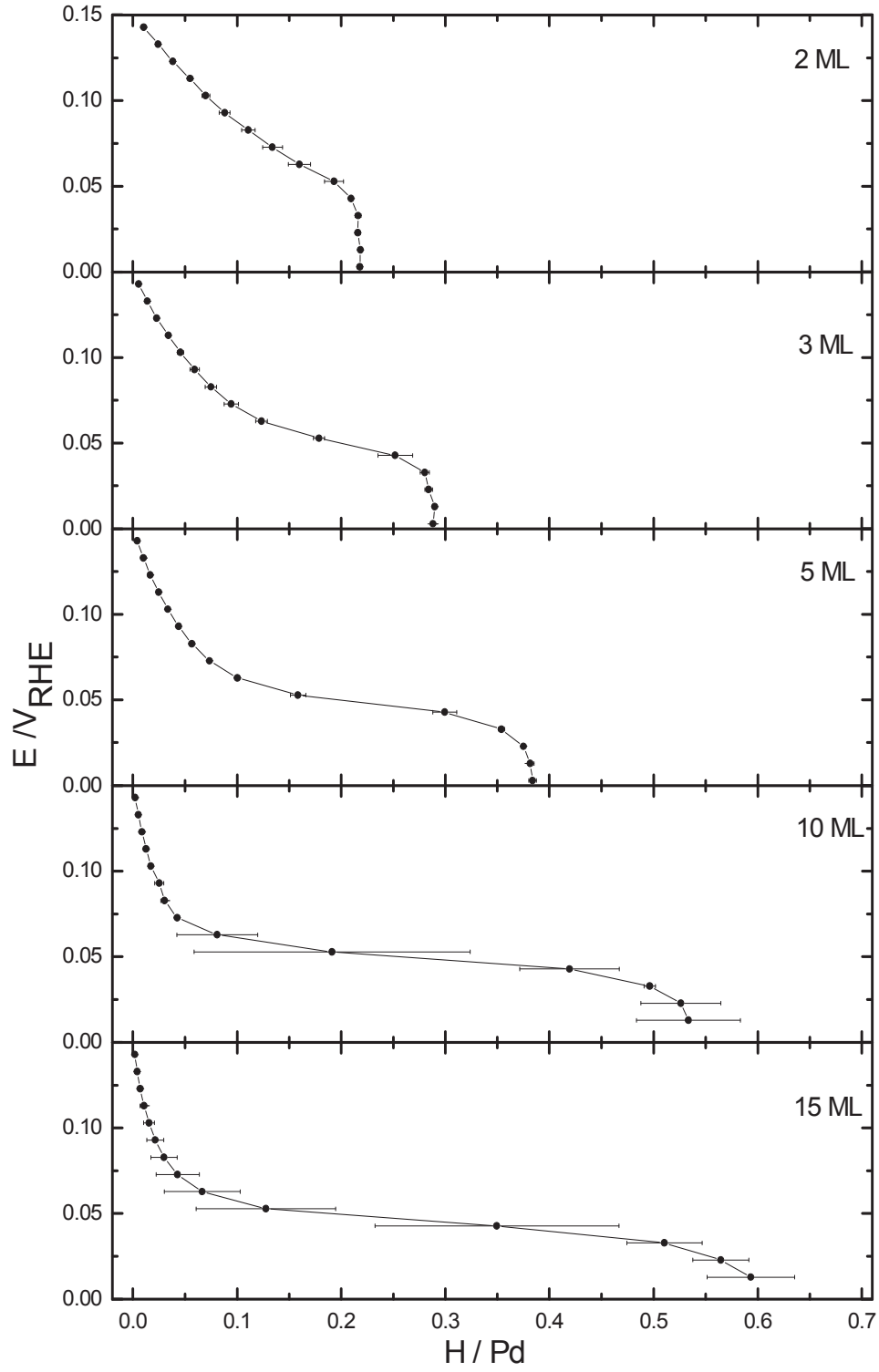

Figure I.6: Isothermes d'insertion électrochimiques pour les films $Pd_{x\ MC}$/Au(111), 0,1 M H_2SO_4.

La solubilité maximum $(H/Pd)_{max}$ est grandement modifiée par l'épaisseur des films, diminuant d'un facteur 3 en passant de 15 MC à 2 MC (cf. Figure I.7). Sa valeur est plus proche de Pd massif [38] pour les films plus épais, alors qu'elle est d'environ 0,2 pour

Pd_{2MC}/Au(111). Ces résultats montrent que le substrat joue un rôle majeur, son influence étant plus importante pour les films les plus minces.

À l'inverse de Pd/Pt(111), l'insertion d'hydrogène peut être observée pour 2 MC.

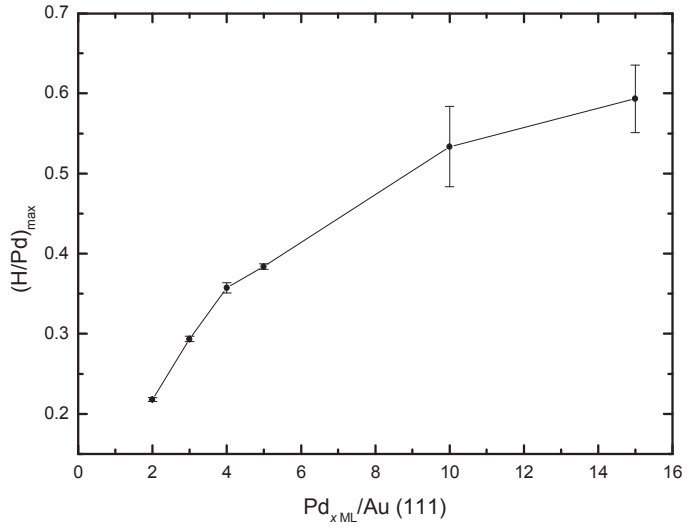

Figure I.7: Taux d'insertion maximum de l'hydrogène $(H/Pd)_{max}$ suivant l'épaisseur des films de Pd/Au(111).

La largeur du plateau bi-phasique décroît avec l'épaisseur et disparaît complètement pour $Pd_{2\,MC}$/Au(111). Sa pente se comporte de manière opposée, celle-ci étant plus prononcée pour les dépôts les plus fins. Cette observation confirme le fait que la pente est principalement due à l'effet du substrat : plus le film est mince et plus forte est l'influence du substrat.

Comme discuté dans le paragraphe précédent, les valeurs α_{max} et β_{min} ne sont pas aussi bien définies que pour Pd massif et la difficulté à déterminer une valeur univoque augmente avec la diminution d'épaisseur des films. Pour 2 MC, elles ne sont carrément pas définies, de même que le plateau a disparu. Néanmoins, les courbes des isothermes semblent montrer que les valeurs de α_{max} et β_{min} tendent respectivement à augmenter et diminuer avec la diminution d'épaisseur.

Nous remarquerons aussi que le plateau de l'isotherme de $Pd_{2\,MC}$/Au(111) ne montre aucun plateau, rappelant le comportement des alliages AuPd [39,40]. Ce résultat pourrait

suggérer la formation d'un alliage à l'interface Au/Pd même si nous ne pouvons rien conclure de définitif là-dessus.

Dans le paragraphe suivant, nous allons montrer que la comparaison avec les résultats obtenus pour les nanofilms Pd/Pt(111) et les nanoparticules de Pd non supportées permet une compréhension plus profonde du comportement des isothermes de Pd/Au(111).

Comparaison avec les nanofilms de Pd/Pt(111)

La Figure I.8 montre la comparaison des isothermes d'insertion de l'hydrogène dans des films de Pd d'épaisseurs équivalentes sur Au(111) et Pt(111) :

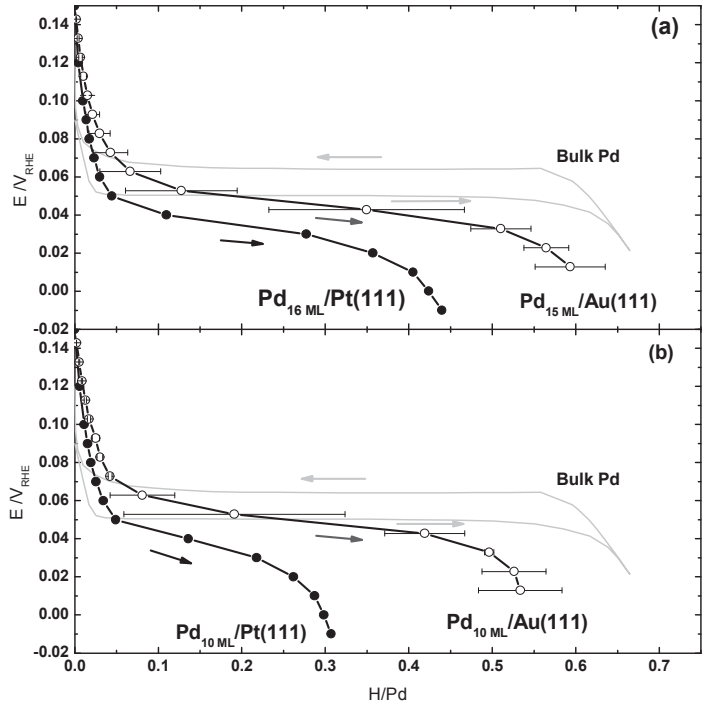

Figure I.8: Isothermes d'insertion de H dans Pd massif [35] (ligne grise), $Pd_{x\ MC}$/Au(111) (cercles creux) et $Pd_{x\ MC}$/Pt(111) [7] (cercles pleins) pour 15 MC (a) et 10 MC (b) d'épaisseur équivalente.

Nous observons trois changements importants. Premièrement, la solubilité totale de l'hydrogène est plus élevée dans Pd/Au(111) comparée à Pd/Pt(111). Deuxièmement, la pente du plateau est beaucoup plus faible. Enfin, l'insertion d'hydrogène se produit à potentiel plus élevé. Grâce à ce potentiel plus élevé, nous avons été capable de mesurer l'insertion d'hydrogène dans Pd/Au(111) jusqu'à 2 MC sans perturbation importante de

l'HER, à l'inverse de Pd/Pt(111) où le dégagement de H_2 masquait complètement l'insertion d'hydrogène pour les épaisseurs inférieures à 10 MC.

Le substrat joue certainement un rôle clé dans le comportement des isothermes observé. La modification par effets géométriques et de ligand du processus d'adsorption a déjà été prédite théoriquement [41]. Plus précisément, Roudgar *et al.* ont réalisé une étude théorique sur l'adsorption de H sur des couches plates de Pd sur Au(111) et Au(100) [42]. À notre connaissance, aucun travail théorique n'a été mené sur l'effet de substrat pour l'insertion d'hydrogène dans les films de Pd.

En fait, des structures bien différentes pour les films Pd/Pt(111) [8] et Pd/Au(111) (voir chapitre III) ont été mises en évidence par diffraction de surface des rayons X. L'influence du substrat Pt(111) sur la structure des films de Pd déposés s'étend sur un grand nombre de couches atomiques. Les dépôts de Pd sont assez plats, indépendamment de l'épaisseur des films et ne relaxent vers Pd massif qu'au-delà d'une dizaine de couches pseudomorphes.

L'influence du substrat conduisant à un gradient sur un grand nombre de couche et induisant une fraction importante de sites d'insertion non-équivalents, peut largement contribuer à la pente accentuée du plateau pour Pd/Pt(111). Inversement, l'effet du substrat Au(111) disparaît rapidement avec l'épaisseur. Les films de Pd sur Au(111) n'ont une croissance couche par couche que pour les deux premières couches atomiques. Dès la troisième couche, la croissance devient tri-dimensionnelle avec une relaxation des distances interatomiques vers celles du Pd massif.

La morphologie et plus spécifiquement l'épaisseur de la zone contrainte, semblent avoir un effet important sur le taux d'insertion de l'hydrogène, particulièrement avec la diminution de l'épaisseur du dépôt. Par ailleurs, les paramètres de maille des deux métaux, le support et le dépôt de Pd, sont très proches dans le cas du platine avec un disaccord $(a_{Pt} - a_{Pd})/a_{Pt} = 0.0086$, alors que pour l'or, il est de $(a_{Au} - a_{Pd})/a_{Au} = 0.046$. Ceci conduit au fait que les premières couches de Pd, qui sont pseudomorphes, sont plus étirées dans le plan sur Au(111) que sur Pt(111), conduisant certainement au comportement différents des isothermes des deux systèmes.

Le taux d'insertion maximum d'hydrogène pour les dépôts plus épais est la combinaison des contributions d'une partie similaire au matériau massif et des couches contraintes. Les dépôts Pd/Au(111) tendent plus rapidement vers le comportement du Pd massif avec l'augmentation de l'épaisseur. Ceci pourrait contribuer à expliquer le taux plus élevé de $(H/Pd)_{max}$, de même que le potentiel plus élevé d'insertion et la plus faible pente du plateau.

Effet de la taille nanométrique

Comme l'ont montré les différents paragraphes, les films de Pd supportés ont des caractéristiques qui peuvent différer significativement de celles des matériaux massifs. Afin d'essayer de séparer les effets de substrat de ceux de l'effet de taille nanométrique, il est intéressant de faire une comparaison avec des nanoparticules non supportées.

La Figure I.9 montre les isothermes de différents systèmes de Pd : Pd massif, nanoparticules commerciales non-supportées [1] et films minces de Pd déposés sur des surfaces monocristallines.

Il faut remarquer que les dimensions caractéristiques des films supportés (épaisseur équivalente de 15 MC) et des nanoparticules (taille moyenne de 3,6 nm) sont proches, permettant une comparaison directe de leurs isothermes. La contribution de l'adsorption dans les isothermes ne peut être négligée dans le cas des nanoparticules de Pd (effet de surface). Malheureusement, la chimisorption de l'hydrogène ne peut pas être distinguée de l'absorption lors des mesures en phase gaz. Aussi, pour comparer les isothermes des deux nanosystèmes (films et nanoparticules), nous devons recalibrer les isothermes des nanofilms en incluant la charge d'adsorption d'hydrogène.

Comparé à Pd massif, les deux systèmes nanométriques (films et nanoparticles) sont caractérisés par une plus faible valeur de $(H/Pd)_{max}$ et un domaine bi-phasique restreint. Au delà des différences de valeur de $(H/Pd)_{max}$, qui ont déjà été discutées au paragraphe précédent, l'inclinaison du plateau est présente dans les deux films supportés alors qu'elle est absente pour les nanoparticules non supportées. Ceci confirme que le comportement spécifique de l'isotherme est dû aux contraintes induites par le substrat et non par la taille

nanométrique du système, comme cela a déjà été discuté par Soldo *et al.* [8] pour l'insertion d'hydrogène dans Pd/Pt(111).

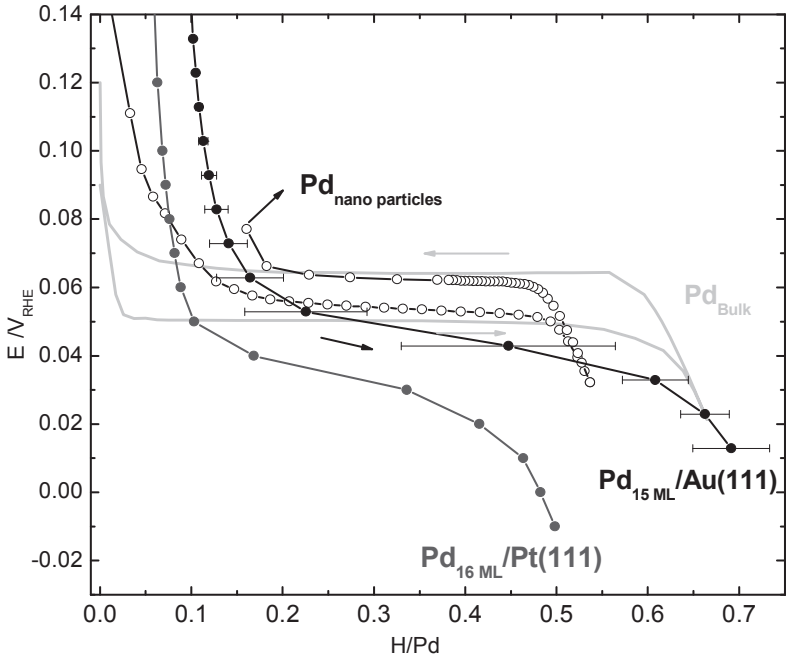

Figure I.9: Isotherme de H dans Pd massif, des nanoparticules de Pd non-supportées (taille moyenne 3,6 nm) [7, 43] et des nanofilms de Pd : Pd_{15MC}/Au(111) et $Pd_{16\ MC}$/Pt (111) b).

Vieillissement des échantillons

Le palladium massif subit des transformations structurales irréversibles après des cycles d'insertion/désorption d'hydrogène. Ce vieillissement est attribué au large désaccord entre les paramètres de maille du Pd seul et de la phase β, caractérisée par une expansion d'environ 3,5%. Il est intéressant de vérifier si un tel comportement est toujours observé dans les films minces supportés de Pd, où la taille nanométrique pourrait modifier l'effet des cycles successifs sur le vieillissement. La Figure I.10 montre le résultat d'une expérience de vieillissement, où les mesures d'isothermes d'insertion ont été répétées plusieurs fois sur deux dépôts différents : $Pd_{7\ MC}$/Au(111) et $Pd_{10\ MC}$/Au(111).

[b] La contribution de l'adsorption d'hydrogène a été incluse aussi bien pour les nanoparticules que les films.

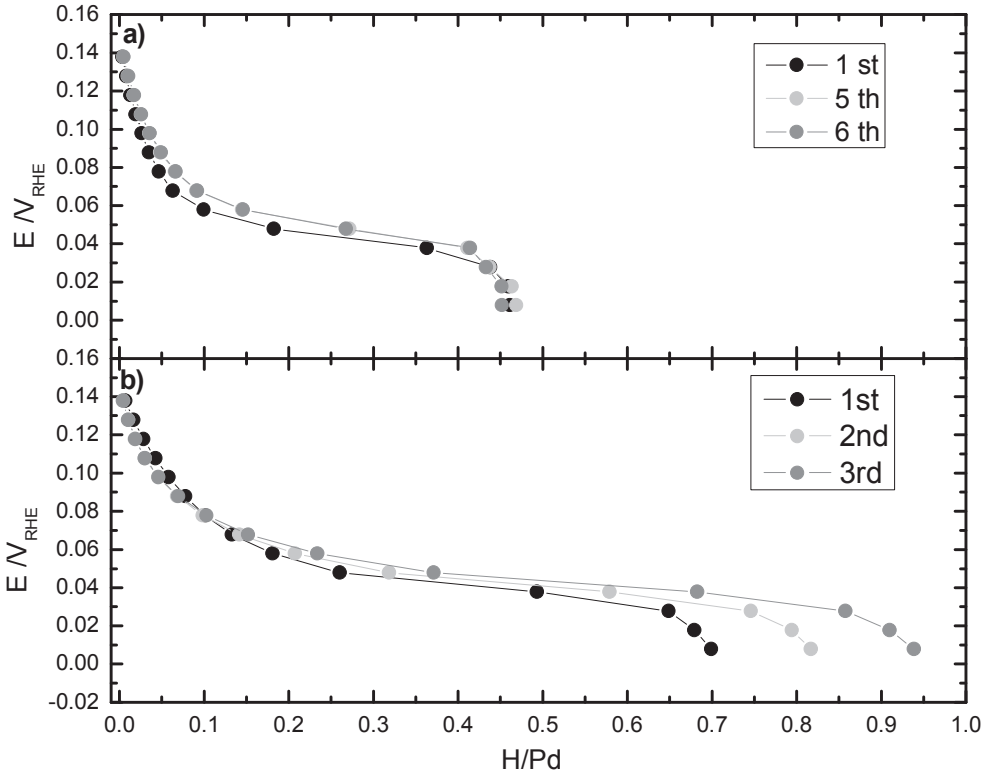

Figure I.10: Branches d'absorption des isothermes d'insertion de H dans 0,1 M H_2SO_4 durant des expériences de vieillissement sur a) $Pd_{7\ MC}$/Au(111); b) $Pd_{10\ MC}$/Au(111).

Les isothermes d'insertion de l'hydrogène révèlent que les films de Pd subissent une modification structurale durant les cycles d'insertion/désorption de l'hydrogène. Avec le vieillissement, α_{max} augmente légèrement et le potentiel correspondant au domaine bi-phasique est plus élevé. Des caractérisations physiques seraient nécessaires, afin d'établir un lien direct avec l'évolution structurale du film. En particulier, la formation éventuelle d'un alliage de surface Pd-Au devrait être vérifiée, un comportement similaire ayant été observé avec des alliages massifs. Plus spécifiquement, des techniques potentiostatiques appliquées sur des électrodes d'alliage Ag-Pd[c] durant l'absorption d'hydrogène depuis une solution aqueuse ont montré que α_{max} augmentait et la solubilité maximum d'hydrogène diminuait avec la charge en argent [44].

[c] L'argent et l'or ont des paramètres de maille très proches (a_{Ag}=4,0853Å, a_{Au}=4,09Å)

On remarque que l'effet de la procédure de vieillissement augmente avec l'épaisseur du dépôt. Alors que l'isotherme de $Pd_{7\ MC}$/Au(111) ne semble que faiblement affectée, α_{max} et H/Pd_{max} changent significativement avec le vieillissement pour les épaisseurs les plus importantes comme 10 MC.

Nous pensons que ce comportement trouve son explication principale dans la façon les contraintes induites par le substrat s'étendent à travers l'épaisseur du film. Comme expliqué dans le paragraphe précédent, l'influence du substrat décroît rapidement pour Pd/Au(111), le film de Pd devenant de plus en plus rugueux et relaxé (croissance 3D) avec l'épaisseur. Ils présentent rapidement un comportement du Pd massif, montrant au vieillissement des déformations morphologiques irréversibles, au-delà de la limite élastique.

I.2.3 **Conclusions**

Nous avons obtenu des isothermes électrochimiques de l'insertion d'hydrogène dans des films de Pd/Au(111) pour des épaisseurs allant de 2 à 15 MC.

Comparé au Pd massif, le taux d'insertion maximum est plus petit, même pour le film de le plus épais Pd_{15MC}/Au(111). Les isothermes présentent aussi une pente dans la région biphasique. Nous avons pu mettre en avant l'influence de l'épaisseur du film sur le taux d'insertion maximum $(H/Pd)_{max}$ qui décroît d'un facteur trois de 15 MC à 2 MC. La largeur du plateau biphasique diminue et disparaît complètement pour $Pd_{2\ MC}$/Au(111), alors que sa pente se comporte de manière inverse, celle-ci étant plus prononcé pour les films les plus minces.

Comparé au films Pd/Pt(111) de même épaisseur équivalente, les isothermes se rapprochent plus vite du comportement du Pd massif avec un taux $(H/Pd)_{max}$ plus élevé et une pente plus faible du plateau biphasique. D'après les mesures sur les films Pd/Pt(111) discutés dans la thèse de Chrystelle Lebouin, ces résultats sont principalement reliés aux effets de substrats et sont très différents entre l'or et le platine. Les effets géométriques et électroniques doivent être considérés pour prendre en compte la plus grande solubilité de l'hydrogène et la largeur plus importante du domaine biphasique dans les isothermes de Pd/Au(111) comparées à Pd/Pt(111). En particulier, $(H/Pd)_{max}$ ne dépend pas uniquement

de la taille nanométrique du système mais aussi de sa morphologie et en particulier des zones 2D contraintes ou relaxées 3D.

La comparaison avec les nanoparticules non-supportées de Pd confirment que la pente est principalement due aux contraintes induites par le substrat, qui conduit à des sites d'absorption non équivalents.

La présence d'hystérèse entre les branches d'insertion et de désorption pour $Pd_{15\ MC}$/Au(111) suggère que l'hystérèse ne disparaît pas dans les films minces, au moins jusqu'à cette épaisseur.

Les cycles d'insertion/désorption d'hydrogène dans les films de Pd/Au(111) créent des déformations inélastiques irréversibles induisant des évolutions des isothermes avec le vieillissement, ce phénomènes étant renforcé avec l'épaisseur.

I.3 Conclusions général

Les films ultra minces de palladium déposés sur une surface monocristalline représentent un modèle très intéressant pour l'étude des propriétés du palladium vis-à-vis de l'insertion/désinsertion de l'hydrogène à l'échelle nanométrique. Dans ce cas, des propriétés originales peuvent apparaître par rapport au palladium massif. Ces dépôts peuvent présenter un caractère monocristallin, qui permet d'éliminer les joints de grains et ainsi les courts-circuits de diffusion.

Cette thèse concerne l'élaboration et la caractérisation des films de Pd déposés sur Au(111) et l'électro-insertion d'hydrogène dans ceux-ci.

Les films ont été caractérisés par voie électrochimique en milieu acide (0,1 M H_2SO_4). Seules des vitesses de balayage inferieure à environ 1 $mV \cdot s^{-1}$ permettent de séparer correctement les différentes contributions observées dans le voltampérogramme. Nous avons pu attribuer les différents pics à des réactions d'adsorption sur des couches spécifiques du dépôt, en particulier sur les surfaces libres de la première et de la seconde couche et des couches suivantes qui sont relaxées. L'évolution des signatures électrochimiques en fonction de l'épaisseur est en accord avec une croissance pseudomorphe des deux premières couches atomiques puis le dépôt d'une troisième couche qui démarre avant le solde de la deuxième.

L'attribution des pics est en accord avec le modèle structural proposé par la caractérisation des films par SXRD *in situ*. Dans ce modèle la croissance 3D au-delà de la deuxième couche est caractérisée par la présence de « tours » hautes d'une vingtaine de couches mais qui n'occupent environ qu'un dixième de la surface de la deuxième couche jusqu'à 10 MC. Le désaccord entre les paramètres de maille du substrat et de couches déposées est probablement la raison principale de cette perte rapide de pseudomorphisme par rapport au système Pd/Pt(111).

Les mesures de transitoires de courant ont montré que le mécanisme de dépôt UPD du Pd est caractérisé par deux étapes : l'adsorption avec décharge partielle est suivie par une nucléation instantanée et une croissance bidimensionnelle. Ce modèle est en accord avec les résultats des caractérisations *in situ* SXRD et les mesures électrochimiques.

Nous avons obtenu les isothermes électrochimiques des films Pd/Au(111) pour différentes épaisseurs, de 2 MC à 15 MC. Le taux maximum d'insertion d'hydrogène $(H/Pd)_{max}$ est plus faible que celui du Pd massif et les isothermes présentent une pente dans le domaine biphasé. Nous avons pu mettre en exergue l'influence de l'épaisseur du film sur le processus d'insertion de l'hydrogène: $(H/Pd)_{max}$ diminue d'environ un facteur 3 de 15 MC à 2 MC. Nos résultats confirment la présence d'insertion d'hydrogène dans les films les plus minces, Pd_{2MC}/Au(111). La largeur du plateau biphasique diminue aussi avec l'épaisseur et disparaît complètement pour Pd_{2MC}/Au(111). La pente a un comportement opposé, étant plus prononcée pour les films les plus minces.

Par rapport aux films Pd/Pt(111) de la même épaisseur, l'isotherme se rapproche plus rapidement du comportement de Pd massif, avec une insertion de l'hydrogène à potentiel plus haut, des valeurs pour $(H/Pd)_{max}$ plus grandes et une pente du plateau biphasique moins importante. La comparaison avec les nanoparticules non supportées de Pd montre que la pente du plateau est principalement due aux contraints induites par le substrat, qui conduisent à la présence de sites d'insertion non équivalents.

La présence d'une hystérèse entre les branches d'insertion et de désinsertion confirme l'idée que l'hystérèse ne dépend pas de l'épaisseur, au moins jusqu'à 15 MC.

Une succession de cycles d'insertion/désinsertion d'hydrogène induit des déformations inélastiques irréversibles, ce phénomène s'accentuant avec l'épaisseur.

Références:

1 A. J. Appleby, J. Power Sour., 29 (1990), 3.

2 J. Larminie & A. Dicks, Fuel Cell Systems Explained (2nd), Chichester: John Wiley & Sons, 2000, 25.

3 L'hydrogène, les nouvelles technologies de l'énergie, Clefs, CEA, 50/51, Hiver 2004-2005.

4 Y. Ye, C. C. Ahn, C. Witham, B. Fultz, J. Liu, A. G. Rinzler, D. Colbert, K. A. Smith, R. E. Smalley, Appl. Phy. Lett., 74 (1999), 2307.

5 S. M. Lee, K. H. An, Y. H. Lee, G. Seifert, T. Frauenheim, J. Am. Chem. Soc., 123 (2001), 5059.

6 R. Z. Ma, Y. Bando, H. W. Zhu, T. Sato , C. L. Xu, D. H. Wu, J. Am. Chem. Soc., 124 (2002), 7672.

7 P. Chen, Z. T. Xiong, J. Z. Luo, J. Y. Lin, K. L. Tan, Nature, 420 (2002), 302.

8 H. Kabashima, S. Futamura, Fuel Chemistry Division Preprints, 47 (2002), 661

9 N. L. Rosi, J. Eckert, M. Eddaoudi, D. T. Vodak, J. Kim, M. O'Keeffet, O. M. Yaghi, Science, 300 (2003), 1127.

10 J. L. Mendoza-Corte, S. S. Han, W. A. Goddard, J. Phys. Chem. A, 116 (2012), 1621.

11 S. S. Han, J. L. Mendoza-Cortes, W. A. Goddard, Chem. Soc. Rev., 38 (2009), 1460.

12 J. H. N. Van Vucht, F. A. Kuijpers, H. C. A. M. Bruning, Philips Res. Rep., 25 (1970), 133.

13 N. V. Krstajić, B. N. Grgur, N. S. Mladenović, M. V. Vojnović, M. M. Jakšić, Electrochim. Acta, 42 (1997), 323.

14 A. Hamaed, T. K. A. Hoang, M. Trudeau, D. M. Antonelli, J. Organomet. Chem., 694 (2009), 2793.

15 D. B. Ravnsbæk, T. R. Jensen, J. Phy. Chem. Sol., 71 (2010), 1144.

16 P. Chen, M. Zhu, Mater. Today, 11 (2008), 36.

17 D. R. Barsellini, A. Visintin, W. E. Triaca, M. P. Soriaga, J. Power Sour., 124 (2003), 309.

18 P. Kumar, L. K. Malhotra, Electrochim. Acta, 49 (2004), 3355.

19 R. C. Ambrosio, E. A. Ticianelli, Surf. Coat. Tech., 197 (2005), 215.

20 M. P. Pitt, D. Blanchard, B. C. Hauback, H. Fjellvåg, W. G. Marshall, Phys. Rev. B, 72 (2005), 214113.

21 J. Chen, H. B. Yang, Y. Y. Xia, Y. Y. Xia, N. Kuriyama, Q. Xu, T. Sakai, Chem. Mater., 14 (2002), 2834.

22 J. N. Huiberts, R. Griessen, Nature, 380 (1996), 231.

23 F. Flory, L. Escoubas, Prog. Quant. Electron., 28 (2004), 89.

24 J. Pettersson, B. Ramsey, D. Harrison, J. Power Sour., 157 (2006), 28.

25 F. Favier, E. C. Walter, M. P. Zach, T. Benter, R. M. Penne, Science, 293 (2001), 2227.

26 L. Boon-Brett, J. Bousek, P. Castello, O. Salyk, F. Harskamp, L. Aldea, F. Tinaut, Int. J. Hydrogen Energ., 33 (2008), 7648.

27 T. B. Flanagan, Annu. Rev. Mater. Sci., 21 (1991), 269.

28 M. V. Goltsova, Int. J. Hydrogen Energ., 31 (2006), 223.

29 S. Bliznakov, E. Lefterova, N. Dimitrov, Int. J. Hydrogen Energ., 33 (2008), 5789.

30 I. Jain, M. Abu Dakka, Int. J. Hydrogen Energ., 27 (2002), 395.

31 M. Eriksson, I. Lundström, L. G. Ekedahl, J. Appl. Phys. 82 (1997) 3143.

32 M. Enyo, T. Maoka, Surf. Technol., 4(1976), 277.

33 M. Bhardwaj, Int. J. Hydrogen Energ., 34(2009), 1655.

34 L. Birry, A. Lasia, Electrochim. Acta, 51 (2006), 3356.

35 C. Lebouin, Y. Soldo-Olivier, E. Sibert, P. Millet, M. Maret, R. Faure, J. Electroanal. Chem., 626 (2009), 59.

36 Y. Soldo-Olivier, M. C. Lafouresse, M. De Santis, C. Lebouin, M. de Boissieu, E. Sibert, J. Phys. Chem. C, 115 (2011), 12041.

37 A. Pundt, M. Suleiman, C. Bähtz, M.T. Reetz, R. Kirchheim, N.M. Jisrawi, Mater. Sci. Eng. B, 108 (2004), 19.

38 M. Baldauf, D. M. Kolb, Electrochim. Acta, 38 (1993), 2145.

39 A. Sieverts, E. Jurisch and A. Metz, Z. Anorg. Chem., 92 (1915), 329.

40 F. A. Lewis, Platinum Metals Rev., 5 (1961), 21.

41 J. R. Kitchin, J. K. Nørskov, M. A. Barteau, and J. G. Chen, Phys. Rev. Lett., 93 (2004), 156801.

42 A. Roudgar, A. Groβ, J. Electroanal. Chem. 548 (2003),121.

43 C. Lebouin, Y. Soldo-Olivier, E. Sibert, M. De Santis, F. Maillard, R .Faure, Langmuir, 25 (2009), 4251.

44 A. C. Makrides, J. Phys. Chem., 68 (1964), 2160.

Acknowledgement

It would not have been possible to complete this dissertation without the guidance and the help from several individuals, friends, issues and family who in one way or another contributed and extended their valuable assistance in this work.

First, I would like to express my sincere gratitude to my advisor, Dr. Y. Soldo-Olivier, for her guidance, caring, patience, and providing me with a good condition for doing research. Her excellence specialty and works in SXRD experiment is the key for the solution of many basic questions in this thesis.

Second, I would like to thank Dr. E. Sibert a lot, the co-advisor, who is good at both experiment and theory, and let me experience the research of electrochemistry and practical issues beyond the textbooks, patiently corrected my writing. He together with Dr. Y. Soldo-Olivier were guiding my research for the past several years and helping me to develop my background in physicochemistry and electrochemistry.

Then I would like to thank Dr. T. Pauporté and Dr. P. Millet, who is willing to participate the committee as a reviewer, as well as Prof. E. Maisonhaute as an examinator.

Deep thanks go to Prof. R. Nogueira, who was willing to participate in my final defense committee as president.

Many thanks to M. Maurizio De Santis (Néel Institute) and to the staff of the French CRG D2AM beamline at the ESRF, as well as to the other members in ESME team and to the workers in ESRF, their works and experiences accumulated in relative domains helped me a lot. My research would not have been possible without their help.

Special thanks go to Prof. G. Feng and to prof. J. Fouletier. Prof. G. Feng introduced me to the LEPMI laboratory and negotiated between us together with director J. Fouletier when we encountered communication problems. They were always willing to give help and suggestions to the work.

And I would like to thank M. Z. Z. Zhao, who as a good friend was always willing to help and give his best suggestions. It would have been a lonely lab without him.

More, I would also like to thank my parents and elder brother. They were always supporting me and encouraging me with their best wishes. They were always there cheering me up and stood by me through the good times and bad.

Finally, I would like to thank China Scholarship Council (CSC), who financially supported my study in France, and Chinese Embassy in France, who facilities my life in France.

Table of Contents

Introduction

With the progress of human society, the demand for energy has been tremendously growing in the last decades. Unfortunately, fossil fuels are not a renewable energy resource. The limitation of ultimate reserves of fossil fuels - currently 80% of primary energy consumed in the world - imposes to resort to alternative energies, such as renewable energy (solar, geothermal, wind, hydropower, ...), nuclear power in its most advanced sectors (Generation IV) or controlled fusion. Moreover, the burning of fossil fuels induces large amounts of pollution. Over the past years, the CO_2 content in the air continually raised, leading to an important global warming. SO_2, soot, industrial dust, nitrogen oxides and oil pollution stagnation in the environment represent important sources of contamination, as well.

Nowadays, there are two main tasks for worldwide energy development strategy:

- to satisfy the increasing energy demand of the growing world population, population who naturally aspires to its economic and social development. With the current growth rate, doubling time of global energy consumption is around 50 years.

- to diminish the human pollutant emissions, developing environment-friendly energy resources. For the time being, at the global level we issue two times more CO_2 than nature can absorb.

In this context, research in energy carriers other than electricity and heat, capable to produce massive storage and economic transport over large distances, is of primary importance. Indeed, the electric current can’t be the only energy source, because of the important costs for transportation and distribution; moreover, at present no way for mass storage of this form of energy is known.

For these reasons, hydrogen, which can be converted into electricity and heat using fuel cells, will play a major role in the energetic future of our planet.

William Grove first proposed in 1839 the concept of fuel cells [1], where flows of hydrogen and oxygen are converted into water, process which is accompanied by electricity production. The theoretical energy conversion efficiency is as high as 83%, which is much higher than the internal combustion engine, subjected to Carnot cycle limitations [2]. Practically, the energy efficiency of fuel cells are generally between 40-60% [3].

Nevertheless, two major problems must be solved in order to use hydrogen as energy vector on a very large scale.

The first is related to its production, for which current methods are not optimized and still present high cost. Though there is abundant hydrogen on earth, it only exists in the form of compounds and must be extracted before being used. Pure hydrogen can be easily produced by electrolysis of water, but this process is characterized by low efficiency and high energy consumption. For example, the production of hydrogen by water electrolysis needed to operate the fleet of vehicles in circulation in France would require the same amount of electricity corresponding to the current French consumption [4]. Decomposition of water by electrolysis or by chemical reactions at high temperature and thermochemical decomposition of biomass are more and more developing research topics.

The second problem to be overcome for the generalized use of hydrogen as energy vector concerns its storage. Hydrogen in gaseous form is flammable, explosive and easy to spread. Problems relied to its safe and efficient storage and transportation must therefore be solved.

Storage under high pressure (> 350 bar) has seen the development of composite tanks (carbon fibers and polymers), lighter than metal ones. Nevertheless, the problem of compression beyond 350 bars still remains, because of the high cost of this operation (25% of storage capacity lost compared to the compression of an ideal gas) [4].

Liquid hydrogen storage, where gaseous hydrogen is cooled down to -253 ^{0}C, needs excellent insulation devices in order to prevent vaporization.

Adsorption of hydrogen (physical and chemical adsorption) represents another safe and high efficient technology, where nano-materials such as carbon nano-tubes (NTs) [5,6] and carbonitride NTs [7] as new adsorbent are used. For example, hydrogen adsorption on crystalline ropes of carbon single-walled nanotubes (SWNT) was found to exceed 8wt.% [5].

Chemical hydrides [8] have also been developed, involving ionic (NaH, CaH_2,…) or covalent (CH_4,…) chemical bonds with hydrogen [9], as well as metal-organic-frameworks (MOF), consisting of metal ions or clusters coordinated to organic molecules [10,11,12].

Metallic hydrides (metal-hydrogen alloys), able to absorb hydrogen in a reversible way, offer another interesting option. Several light metallic hydrides with high storage capacity have been tested ($LaNi_5$ [13], TiNi [14], $NaAlH_4$ [15],…). The density of stored hydrogen d_H per unit volume can be 1000 times higher than gaseous hydrogen at the same temperature and pressure conditions and can be equal or even exceed the liquid hydrogen density (eg. d_H=96.7 Kg·m^{-3} in $LiAlH_4$, d_H=70.8 Kg·m^{-3} in liquid hydrogen) [16].

Nevertheless, physicochemical behavior and insertion-desorption mechanisms in metallic hydrides are still a scientific challenge [17]. In particular, these materials, and especially magnesium based alloys and alanates[a], can exhibit significant chemical reactivity and will probably be encapsulated [18,19,20,21]. One possibility could be the realization of nanometric deposits on these alloys [22]. Thin-film metal hydride hydrogen storage technology is all the more interesting that it covers several other applications, like functional optical glass [23,24], new type electrodes [25] or gas sensors [26,27].

[a] **Alanates** are compounds that contain aluminium, (stored) hydrogen, and a metal like sodium or lithium.

In this context, ultra-thin films of palladium deposited on a mono-crystalline surface represent an interesting model not only to study the properties of palladium towards the insertion/removal of hydrogen at the nano-scale, which may reveal specific properties compared to solid palladium samples, but also because of the mono-crystalline character of the film, which eliminates grain boundaries and thus short-circuit diffusion paths.

The palladium–hydrogen system has been most widely studied among the different hydrides available [28,29]. Thanks to its good mechanical properties, a high absorption capacity and its high purity, palladium is often used as a model for the study of thermodynamic and kinetic properties of metal-hydrogen systems (M-H) or intermetallic alloys. The catalytic role (dissociation of di-hydrogen) and the high kinetic of hydrogen insertion/removal in palladium is also a real asset.

The present study concerns the elaboration and characterization of Pd films on Au(111) and the electro-insertion of hydrogen. Chapter I present the bibliographic study. In chapter II we discuss the results obtained on the electrochemical deposition and characterization of Pd/Au(111) films. Chapter III concerns the study of the growth mechanisms, in particular for the first under potentially deposited Pd layer; transient current and *in situ* Surface X-Ray diffraction experiments are discussed. Chapter IV is dedicated to the experimental determination of the electrochemical insertion isotherms for Pd deposits with various thicknesses. The last chapter gives a summary of the whole thesis, as well as an outlook in this field.

Reference:

1 A. J. Appleby, J. Power Sour., 29 (1990), 3.

2 J. Larminie & A. Dicks, Fuel Cell Systems Explained (2nd), Chichester: John Wiley & Sons, 2000, 25.

3 S. Mekhilef, R. Saidur, A. Safari, Renew. Sust. Energ. Rev., 16 (2012), 981.

4 L'hydrogène, les nouvelles technologies de l'énergie, Clefs, CEA, 50/51, Hiver 2004-2005.

5 Y. Ye, C. C. Ahn, C. Witham, B. Fultz, J. Liu, A. G. Rinzler, D. Colbert, K. A. Smith, R. E. Smalley, Appl. Phy. Lett., 74 (1999), 2307.

6 S. M. Lee, K. H. An, Y. H. Lee, G. Seifert, T. Frauenheim, J. Am. Chem. Soc., 123 (2001), 5059.

7 R. Z. Ma, Y. Bando, H. W. Zhu, T. Sato , C. L. Xu, D. H. Wu, J. Am. Chem. Soc., 124 (2002), 7672.

8 P. Chen, Z. T. Xiong, J. Z. Luo, J. Y. Lin, K. L. Tan, Nature, 420 (2002), 302.

9 H. Kabashima, S. Futamura, Fuel Chemistry Division Preprints, 47 (2002), 661.

10 N. L. Rosi, J. Eckert, M. Eddaoudi, D. T. Vodak, J. Kim, M. O'Keeffet, O. M. Yaghi, Science, 300 (2003), 1127.

11 J. L. Mendoza-Corte, S. S. Han, W. A. Goddard, J. Phys. Chem. A, 116 (2012), 1621.

12 S. S. Han, J. L. Mendoza-Cortes, W. A. Goddard, Chem. Soc. Rev., 38 (2009), 1460.

13 J. H. N. Van Vucht, F. A. Kuijpers, H. C. A. M. Bruning, Philips Res. Rep., 25 (1970), 133.

14 N. V. Krstajić, B. N. Grgur, N. S. Mladenović, M. V. Vojnović, M. M. Jakšić, Electrochim. Acta, 42 (1997), 323.

15 A. Hamaed, T. K. A. Hoang, M. Trudeau, D. M. Antonelli, J. Organomet. Chem., 694 (2009), 2793.

16 D. B. Ravnsbæk, T. R. Jensen, J. Phy. Chem. Sol., 71 (2010), 1144.

17 P. Chen, M. Zhu, Mater. Today, 11 (2008), 36.

18 D. R. Barsellini, A. Visintin, W. E. Triaca, M. P. Soriaga, J. Power Sour., 124 (2003), 309.

19 P. Kumar, L. K. Malhotra, Electrochim. Acta, 49 (2004), 3355.

20 R. C. Ambrosio, E. A. Ticianelli, Surf. Coat. Tech., 197 (2005), 215.

21 M. P. Pitt, D. Blanchard, B. C. Hauback, H. Fjellvåg, W. G. Marshall, Phys. Rev. B, 72 (2005), 214113.

22 J. Chen, H. B. Yang, Y. Y. Xia, Y. Y. Xia, N. Kuriyama, Q. Xu, T. Sakai, Chem. Mater., 14 (2002), 2834.

23 J. N. Huiberts, R. Griessen, Nature, 380 (1996), 231.

24 F. Flory, L. Escoubas, Prog. Quant. Electron., 28 (2004), 89.

25 J. Pettersson, B. Ramsey, D. Harrison, J. Power Sour., 157 (2006), 28.

26 F. Favier, E. C. Walter, M. P. Zach, T. Benter, R. M. Penne, Science, 293 (2001), 2227.

27 L. Boon-Brett, J. Bousek, P. Castello, O. Salyk, F. Harskamp, L. Aldea, F. Tinaut, Int. J. Hydrogen Energ., 33 (2008), 7648.

28 T. B. Flanagan, Annu. Rev. Mater. Sci., 21 (1991), 269.

29 M. V. Goltsova, Int. J. Hydrogen Energ., 31 (2006), 223.

Chapter I. Bibliographic study on ultrathin Pd film deposition on Au(111) and hydrogen electro-insertion

In this chapter the prominent results present in the literature are presented, concerning Pd deposition onto Au(111), electrochemical and physical characterization of the Pd films, electrocatalytic properties and hydrogen isotherms.

I.1 Ultra-thin Pd film deposition onto Au(111)

Metal electro-deposition requires a detailed knowledge of the influence of all the deposition parameters including substrate structure and electrolyte composition. The initial stages of metal deposition are of particular interest as they play a decisive role in the growth behaviour and in the emerging morphology of the adlayers [1]. Moreover, studies on the growth mechanism at the atomic level are essential to well understand the adlayer's activity.

Palladium has been deposited on several single crystal surfaces, like Au(hkl) [2,3,4], Pt(hkl) [5,6,7,8,9,10], W(hkl) [11,12] and Rh(hkl) [13,14,15]. The physical and chemical properties of Pd thin film were found not only to be different compared to polycrystalline substrate, but also to vary with the substrate and its orientation.

Pd/Pt(111) deposits have been recently studied by the ESME team in LEPMI [16,17,18]. Indeed, platinum is a very interesting substrate for ultra-thin palladium film deposition. Their lattice parameters are very close (a_{Pt}= 3.9242 Å, a_{Pd}= 3.8907 Å; both elements have fcc structure) and it is therefore possible to obtain Pd pseudomorphic deposits up to more than 10 layers [18]. The cyclic voltammetry experiments show the strong influence of chloride concentration on the deposition process, characterized by a slow kinetics and by complex deposition mechanisms [16].

Contrarily to Pt, Au lattice parameter is larger compared to Pd (a_{Au}=4.0782 Å). Important electronic and geometric effects are expected, inducing different growth

mechanisms and final structure of the deposited Pd/Au(111) ultra-thin films, as well as new properties for the Pd-H system.

I.1.1 Deposition in ultra high vacuum (UHV) conditions

Cherns and Stowell [19] directly observed with transmission electron microscopy (TEM) the growth of Pd on Au(111) substrates carried out in UHV. They found that Pd films grow pseudomorphic up to a mean deposit thickness of about 6 Å, when a continuous misfit dislocation network begins to grow.

Gold is the only fcc metal that exhibits a reconstruction of the close packed (111) surface [20], with a different atomic arrangement from cleaved-bulk configuration. This herringbone surface reconstruction (see Figure I.1), also referred to as striped phase, results from the spontaneous formation of stress domains. It corresponds to a uniaxial surface dislocation network typically referred to as ($p\times\sqrt{3}$) structure, where p≈22, and is characterized by an average contraction of the reconstructed Au surface layer of 4.5% [21].

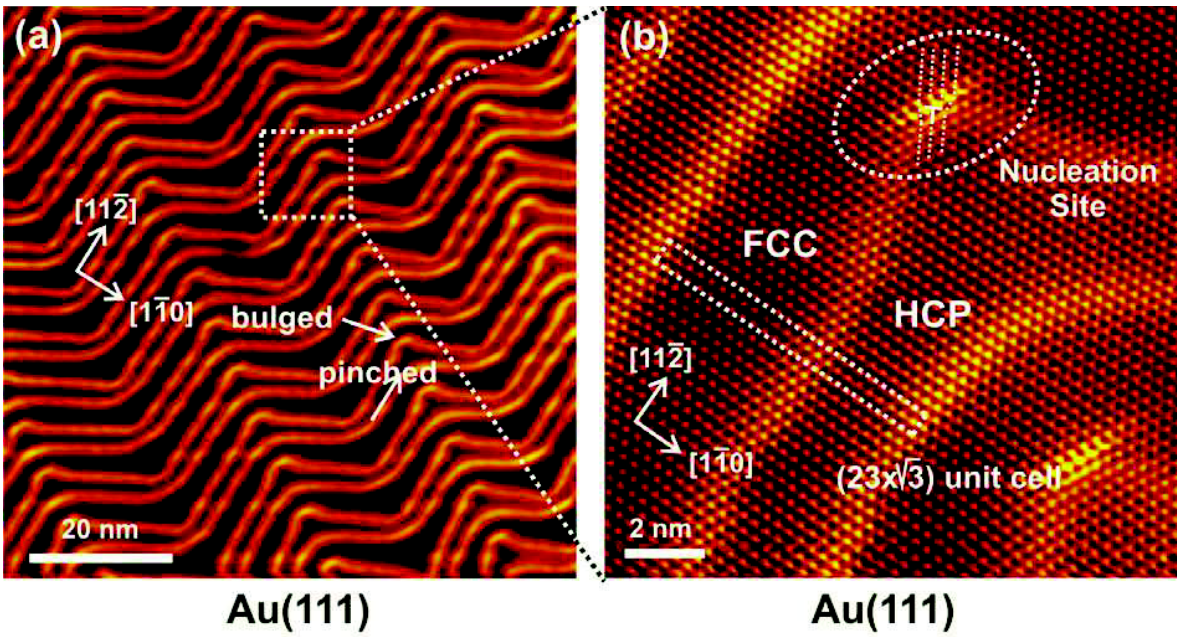

Figure I.1 [22]: STM images of the herringbone reconstruction on Au(111). (a) 80×80 nm^2; (b) Atom-resolved image, 14×14 nm^2.

Yagi *et al.* [23] observed with Scanning Tunneling Microscopy (STM) the broadening of the fringes spacing after less than one monolayer Pd deposition onto reconstructed Au(111)-(22 $\times\sqrt{3}$) surface. Depositing one or two Pd monolayer, the fringes disappear, and further deposition produces misfit dislocations.

Stephenson *et al.* [24] characterized with UHV-STM the Pd film deposited onto Au(111)-($\sqrt{3}$ $\times$22) from 0.07 monolayer (ML) up to around 2 ML. Nucleation and growth initially occur at sites near the surface edge dislocation. The reconstructed structure of Au substrate is maintained at very low Pd coverage, while it is distorted for about 0.35 ML, where the redirection of partial surface dislocation (PSD) ridges on Au surface is observed. Such Au surface modification affects the morphology of Pd islands in turn, where PSD ridges appear to run "underneath" some of the mono-atomic Pd islands. The images of mono-atomic high bi-dimensional Pd islands at the surface show that they are well ordered and close packed. No layer-by-layer growth is observed and the second Pd layer starts at ~0.5 ML from the polygonal islands of underlying layer, inducing a pronounced roughened Pd surface.

I.1.2 Electrochemical deposition

Electrochemical deposition of a metal onto single crystals is a very interesting way to obtain pseudomorphic thin films. It allows controlling the deposited quantity with good precision and its implementation is relatively easy.

Palladium deposition can be obtained in electrolytes containing Pd ions by linearly changing the applied potential (voltammetry), by fixing the potential value (chronoamperometry, CA), or by applying a constant current (chronopotentiometry, CP). Of course, a mixing of these methods can be used as well.

Pd deposition with voltammetry is shown in Figure I.2 [25]. Deposition starts at about 0.6 V *vs.* SCE, at a higher potential than the equilibrium value for Pd^{2+}/Pd, followed by a first peak corresponding to the so called under potential deposition (UPD)[a]. At lower potential than Nernst value, UPD is followed by bulk deposition. Under potential deposition peak can be well separated from bulk contribution by slowing the potential speed rate down to 1 $mV \cdot s^{-1}$ [25]. The spikes around 0.42 V *vs.* SCE have been ascribed to the phase transition of $[PdCl_4]^{2-}$ adlayer on Au (111). They only appear when there are both Pd^{2+} and Cl^- ions in the solution and decay as Pd coverage increases.

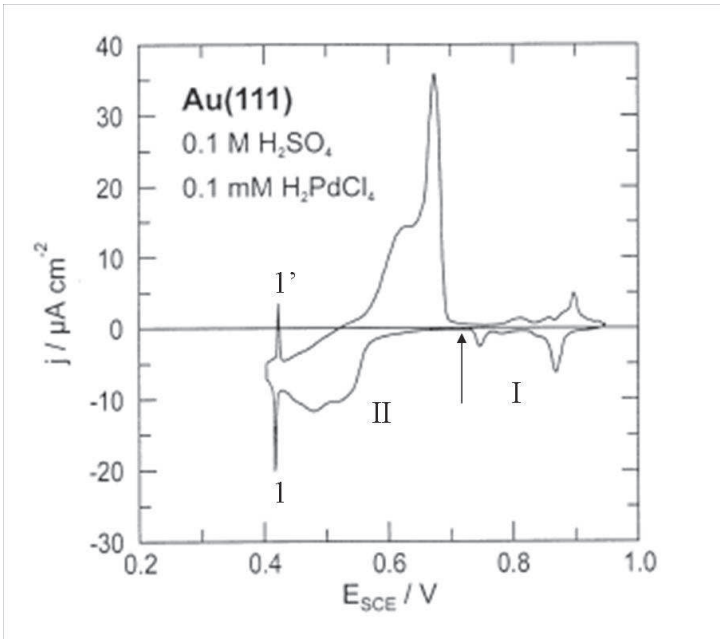

Figure I.2 [25]: Cyclic voltamperometry for Au(111) in 0.1 M H_2SO_4+0.1 mM H_2PdCl_4. The initial potential is indicated by an arrow. Scan rate: 5 $mV \cdot s^{-1}$.

[a] During the electrochemical deposition of a metal, it is not uncommon to find the Under Potential Deposition phenomenon, especially when the substrate is a metal M_{sub} nobler than the metal M which is deposited. It corresponds to the deposition at a more positive potential than the thermodynamic Nernst potential for the couple M^{n+}/M.

While the potential sweeps back, Pd dissolution occurs from 0.51 V to 0.72 V *vs.* SCE. The equilibrium potential is found to be 0.51 V *vs.* SCE. The peaks in region I have been tentatively ascribed to a gradual replacement of the Pd chloro complex by Cl^- ions.

Electrochemical deposition in presence of chloride

In situ STM images of Pd deposition in 0.1 M H_2SO_4 + 0.1 mM H_2PdCl_4 solution onto Au(111) [25] show that the two first Pd layers grow bi-dimensionally. The 3rd Pd layer is found to partly grow in two dimensions and partly as three dimensional clusters. The fourth Pd layer begins to deposit before the 3rd layer has been completed. Pd ions begin to nucleate around gold atomic step at 0.55 V *vs.* SCE, forming small mono-atomic high islands. The islands, growing up in a 2D mode, tend to merge, covering the entire Au(111) surface. These results confirm that the morphology of the overlayers changes with increasing Pd coverage, from flat and well-ordered for the first two monolayers to increasingly rough and defect-rich for higher thicknesses. Pseudomorphic growth of Pd is maintained up to four layers, followed by the appearance of a hexagonal Moiré pattern[b] on the fifth layer. Nevertheless, Pd (111) characteristics in cyclic voltammetry are retained up to at least 10 monolayers.

Electrochemical quartz crystal microbalance (EQCM) can accurately measure the deposited Pd mass by monitoring the change in frequency of a quartz crystal resonator. As frequency measurements can be very accurate, the deposited mass can be estimated with high precision. Naohara *et al.* [26,27] investigated with EQCM and *in situ* STM the electrochemical reduction of the tetrachloropalladate complex $(PdCl_4)^{2-}$ on a Au(111) electrode in a 0.05 M H_2SO_4 + 0.5 mM $[PdCl_4]^{2-}$ solution. They observed that Pd electrochemical deposition at potential values higher than about +0.3 V *vs.* RHE proceeds

[b] **Moiré pattern** is an interference pattern created by the presence of lattice-mismatched systems.

following a bi-dimensional growth mode up to about 4.3 ML. At more negative potentials an abrupt creation of Pd nuclei is present, probably due to the presence of hydrogen adsorption. The comparison with the results of Kibler *et al.* [25], who pointed out a layer-by-layer growth only up to 2 ML in 0.1 M H_2SO_4+0.1 mM H_2PdCl_4 solution, seems to indicate an influence of chloride concentration in the bi-dimensional growth mode of Pd films.

Takahasi [28,29] *et al.* studied with surface X-ray diffraction (SXRD) the structure of a Pd monolayer electrochemically deposited onto Au(111) from 0.1 M H_2SO_4 +1 mM $[PdCl_4]^{2-}$ solution. They find that Pd keeps the fcc stacking sequence of the Au substrate and forms a pseudomorphic smooth monolayer. The spacing between the Au and Pd adlayer is equal to 2.27 Å, while Pd-Au bond length at the Pd/Au(111) interface has been found to be 2.82 Å. Their results suggest that $[PdCl_4]^{2-}$ does not fully cover the deposited Pd monolayer surface. Pd on Au(001) is found to be pseudomorphic as well, even if the Au-Pd interlayer distance is smaller than for Au(111) and is equal to 1.93 Å. For coverage greater than 2 ML, Pd films show different growth modes on Au(111) and Au(100) [30]. Contrarily to STM results [25], Pd adlayers on Au(111) are relaxed beyond the first pseudomorphic layer. Pseudomorphic character is maintained over 10 ML for Pd/Au(001).

Takakusagi *et al.* [31] studied with *in situ* STM the electrochemical deposition of Pd in a 1 mM K_2PdCl_4 + 50 mM H_2SO_4 solution on a ($22\times\sqrt{3}$) reconstructed Au(111) surface. Pd deposition at +0.3 V *vs.* Ag/AgCl was found to proceed in 3D growth mode after preferential nucleation at the elbow sites of the gold surface.

Electrochemical deposition in absence of chloride

In disagreement with the results of Naohara *et al.* [26, 27] supporting the model that $[PdCl_4]^{2-}$ complex plays an important role to inhibit the three-dimensional growth, it has been shown with *in situ* STM microscopy [32, 33] that the growth is two dimensional up to

two layers regardless of the anion in solution in sulfate, nitrate and perchlorate solution. The nature of the anions neither has any effect on the nucleation behavior, Pd atoms preferring to deposit at the mono-atomic-high step-sites of the gold islands' rims. It does, however, influence the shape of the emerging Pd islands simply by affecting surface atom mobility. In the solution with chloride, the 1st monolayer 2D islands have a round shape [25], while in Tang's experiment [32] they are triangular. The situation is opposite for the formation of 2nd Pd monolayer. It was ascribed to the opposite influence of anions on the diffusion of Pd atom on Pd and on Au surfaces.

Pd deposition studied by cyclic voltammetry in 0.1 M H_2SO_4+0.1mM $PdSO_4$ shows two pronounced deposition peaks for high quality gold crystals, attributed to the first and second layer [32]. Contrarily to chloride containing solution, STM images from the same authors show that Pd forms tremendously huge deposits at stepped sites for higher coverage than two layers. Hence chloride-free solution seems to show a higher tendency for three dimensional Pd growth beyond two layers.

Kontje *et al.* [33] find that the Pd UPD and bulk deposition are well separated in 0.1 M HNO_3 + 0.2 mM $Pd(NO_3)_2$ solution. Nevertheless, very slow deposition kinetics is suggested by the fact that bulk deposition begins only around 0.35 V *vs.* SCE instead of 0.53 V *vs.* SCE, the Nernst potential value.

I.1.3 **Alloy formation**

Low Energy Electron Diffraction (LEED) and Auger Electron Spectroscopy (AES) experiments on Pd overlayers deposited in UHV environment on Au(111) show that the onset of intermixing is detectable between 200 and 300 K, with the formation of a stable surface alloy for annealing temperatures in the range 400-525 K [34].

The UHV STM images and LEIS (Low Energy Ion Scattering) results of Stephenson *et al.* [24] give no evidence for Pd/Au(111) intermixing at 300 K. On the contrary, evidence

of alloy formation at 300 K is found by Koel *et al.* [35]. Their LEIS data show that it is not possible to grow a pure Pd monolayer film at this temperature: alloying (segregation of Au to the surface or diffusion of Pd into the subsurface) occurs. Pd diffusion into Au(111) crystal during Pd/Au(111) surface preparation in UHV by vapour deposition is also observed by Schmidt *et al.* [36].

In electrochemical deposition, Kibler *et al.* [25, 37] do not find from *in situ* STM results any alloy formation on Pd/Au(111). The same conclusion is obtained with cyclic voltammetry by Naohara *et al.* [26]. Controversy remains the Pd/Au intermixing on Pd/Au(001). Kibler *et al.* [37] indicate the presence of surface alloy while Takahasi *et al.* [28, 29, 30] show with *in situ* SXRD that, if alloying occurs, it is less than 10%.

I.1.4 Pd film growth: kinetics

Kibler *et al.* [25] studied the kinetics of Pd deposition in 0.1 M H_2SO_4+1 mM H_2PdCl_4 solution by current transient measurements. For Pd deposition, they only obtained exponentially decaying current-time curves. On the contrary, rising transients were observed for the dissolution of a full Pd monolayer and the corresponding charge decreases steadily with increasing defect density. Unfortunately, standard nucleation models were not suitable for fitting the transient, because the time scale was so large that influences of migration and convection could no longer be excluded.

Anions in the electrolytic solution seem to play a role in the kinetics of deposition for the first Pd layer [38]. It is much faster in the deposition process from perchlorate than from sulphate solution. They propose that the adsorbed sulphate layer on Au(111) inhibits the first monolayer Pd deposition. This result is contradicted by Kontje *et al.* [33], who did not observe any inhibiting effect of the adsorbed sulfate layer.

Very slow Pd dissolution kinetics in chloride-free solutions has been evidenced [32], confirming the strong influence of chlorides. Even sweeping from 0.9 V *vs.* SCE, 200 mV

above Pd oxidation, it takes four oxidation-reduction cycles for the Pd coverage drop from 1 ML to 0.2 ML.

Slow kinetics is characteristic of the deposition process, as well. Tang and co-workers [32] observed in 0.1 M sulfuric acid solution that the sweep rate must be at least 1 $mV \cdot s^{-1}$ in order to separate Pd deposition on steps from Pd deposition on terraces [38]. The current-potential curve for palladium deposition onto Au(111) from 0.1 M HNO_3 + 0.2 mM $Pd(NO_3)_2$ solution indicates under potential deposition of the first monolayer [33]. The large over-potential for bulk deposition suggests very slow deposition kinetics in nitrate solution. The same authors conclude that anions (chloride, sulphate and nitrate) have no effects on nucleation behavior, but influence the shape of the emerging Pd islands simply by affecting surface atom mobility.

The initial nucleation and growth mechanism of palladium have been studied with potentiostatic transient measurement by Quayum *et al.* [39]. Their results show that palladium deposition on Au(111) in 0.1 M H_2SO_4 + 0.1 mM $[PdCl_4]^{2-}$ up to about 0.3 ML are in agreement with the instantaneous nucleation and 2D growth model. Discrepancy between this theoretical model and experimental results was observed in solutions containing a higher concentration of $[PdCl_4]^{2-}$. However, their results should be cautious, since their potential ever jumped to OPD range but only got around 0.3 ML deposition during whole procedure. Thus more detailed investigations are necessary to understand the effects of concentration on the growth mode of palladium.

I.2 Electro-catalytic properties of Pd/Au(111) nano-film

It is well known that physical and chemical properties of metals can be considerably modified by the deposition of a thin hetero-metallic film. This modification can improve the (electro)catalytic activity and selectivity of the electrode towards certain reactions. We will give a very brief review of the effect of Pd film deposited onto Au(111) on some main reactions.

I.2.1 The potential of zero charge (pzc)

The potential of zero charge (pzc) corresponds to the condition of electrical charge density on the surface equal to zero and represents a fundamental property of the metal – electrolyte interface. Its knowledge is important in the study of electrode reactions' kinetics, in the selection of corrosion inhibitors, and more generally when it is important to consider the adsorption of components on metal surfaces. For solid surfaces its value is usually obtained by double-layer capacity measurements in dilute solutions, where a pronounced minimum appears in correspondence of the pzc (Gouy – Chapman minimum) [40]. Following this last method, the pzc of 1 ML, 2 ML and 5 ML Pd/Au(111) in dilute NaF solutions has been found to be -0.09 V, -0.10 V, -0.122 V *vs.* SCE, respectively [41]. These values are to be compared with -0.124 V *vs.* SCE for massive Pd(111) electrode. The authors ascribe the pzc potential shift observed for the thinnest Pd films to a slightly different water structure induced by the pseudomorphic character of the Pd first layers.

I.2.2 Oxygen reduction reaction (ORR)

Naohara *et al.* [42] studied the electrochemical reduction of oxygen on epitaxially grown ultra-thin Pd layers on Au(111) and Au (100) in 50 mM $HClO_4$ solution saturated by oxygen. They find that electrocatalytic properties are strongly dependent on the surface structure and on the thickness of the Pd layers. The ORR activity increases with the decrease of the Pd amount on Au(111) and undergoes a maximum for 0.9 ML of Pd. Their results also show that oxygen reduction starts at more positive potential compared to gold single crystal surfaces even in presence of only a submonolayer of Pd.

I.2.3 CO oxidation

El Aziz [43] *et al.* find two potential regions for CO oxidation on Pd(111), related to different adsorption sites, mono-atomic high steps and large terraces with long range

order, respectively. The step sites show a higher catalytic activity with an oxidation peak shift by 200 mV towards more negative values compared to large terraces. Pd/Au(111) nano-films (≤ 5ML) show a slight decrease in reactivity towards CO oxidation compared to massive Pd (111) electrodes, due to geometric and electronic modification induced by the substrate.

Schmidt *et al.* [36] studied CO electro-oxidation on alloyed films (ca. 65 wt.% and 38 wt.% Pd) obtained by Pd vapour deposition in UHV environment. Their results show that oxidation of hydrogen is about one order of magnitude slower as compared with Pt(111). The continuous CO oxidation in CO saturated 0.1 M $HClO_4$ solution at potentials below 0.2 V *vs.* RHE has finite and stable activity, with a positive reaction order with respect to solution phase CO ($j = k_E(P_{CO})^n$, where j is the oxidation current, k_E is constant reaction rate, P_{CO} is the partial pressure of CO in solution phase, n is the reaction order). The oxidation of 1000 ppm CO in H_2 (in 0.1 M $HClO_4$ solution saturated by the mixed gas) at potentials below 0.2 V *vs.* RHE is governed by slow kinetics of hydrogen oxidation. At potentials above 0.2 V *vs.* RHE, however, the oxidation rate of 1000 ppm CO/H_2 on alloyed Pd/Au(111) can reach the stable value of a high-surface area $Pd_{0.45}Au_{0.55}$/Carbon catalyst, demonstrating the high catalyst activity of the Pd-Au system.

I.2.4 Organic molecules

Pd/Au(111) electrode was found to have a higher electrocatalytic activity for the oxidation of formaldehyde than bare Au (111), even in correspondence of a small amount of Pd (eg. 0.4 ML). The activity is even larger for Pd/Au(100) [44]. The anodic peaks due to formaldehyde oxidation are shifted down to the negative potential region as the thickness increases on both Pd/Au(111) and Pd/Au (100). The highest catalytic activity for the oxidation of formaldehyde is obtained for $Pd_{10.1\ ML}$/Au(111) and $Pd_{0.5\ ML}$/Au (100), respectively.

Baldauf *et al.* [2] studied the oxidation of formic acid on thin, epitaxially-grown Pd overlayers on Au and Pt single crystal electrodes (low index single crystalline surface including (111), (110), (001)), Pd deposition from chloride containing solution). The electrocatalytic properties of the Pd overlayers are found to be markedly dependent on their thickness and on their crystallographic orientation. Pd (100) shows the highest catalytic activity of all three low-index faces. Pd/Pt (*hkl*) generally exhibits a much higher activity than Pd/Au (*hkl*) or massive Pd (*hkl*). In all cases a high resistivity of the Pd surfaces against poisoning by CO is observed.

According to the study of Stephenson *et al.* [24], the yield of benzene from the trimerisation of ethyne on Pd/Au(111) was found to have a maximum at around 0.6 ML. The catalytic activity decreases for lower and higher coverage and is found to be critically dependent on the availability of defect-free (111) islands.

I.2.5 Hydrogen evolution reaction

The hydrogen evolution reaction (HER) on Pd/Au(111) has been systematically studied by Kibler *et al.* [45]. The exchange current density[c], whose value is relied to the electro-catalytic activity, has been found to increase in the following order 2ML Pd < 1ML Pd < bulk Pd (more than 2 ML). At the same time, density functional theory (DFT) calculations show that the H-Pd/Au(111) bonding energy [46] behaves in the opposite order. Hence, while the strongest hydrogen bond is on the second Pd monolayer (ML), the respective catalytic activity is the poorest. Consequently, a clear correlation between the electro-catalytic activity and the binding energy of adsorbed hydrogen could be established. Indeed, the ligand (electronic) effect, the geometric effect due to the pseudomorphic growth and the surface defect density represent the most crucial

[c] At the equilibrium potential for a redox reaction, cathodic current is balanced by anodic current. This ongoing current in both directions is called the exchange current.

parameters governing the relation between the structure of the electrode surface and its electrocatalytic activity.

The kinetics of HER on Pd/Au(111) has also been studied by Pandelov *et al.* [38]. It is found to greatly depend on the Pd film thickness. The hydrogen reduction rate increases by a factor of three decreasing the number of layers from 4 to about 1 ML. It is then enhanced by two orders of magnitude for partial coverage down to 0.035 ML and quickly reaches the bare Au(111) for lower amounts of deposited Pd. The effects of partial Pd coverage on HER are explained by a spillover-effect. Hydrogen, preferentially adsorbed on the Pd nano-island, tends to diffuse on the surface and spillover to Au substrate. They finally recombine on Au(111) to generate gas. Au(111) seems to play an important role in HER, even if a refined theory is still required.

I.2.6 H adsorption and absorption

Figure I.3 [47] shows the electrochemical cyclic voltammetry of $Pd_{2\ ML}$/Au(111) in 0.1 M H_2SO_4. Peak 1/1' is ascribed to the reduction/oxidation of Pd. Peaks 2/2' are related to hydrogen/sulphate adsorption/desorption reactions on the surface, while peaks 3/3' correspond to hydrogen insertion/desorption. Compared to bulk Pd, hydrogen adsorption is well separated from hydrogen absorption, which is shifted down to lower potential by about 220 mV. Thus, the hydrogen adsorption and absorption becomes distinguishable on Pd/Au(111) thin films, due to a substrate effect. Moreover, the oxidation potential is advanced (peak 1'), showing that Pd film is more active than bulk Pd.

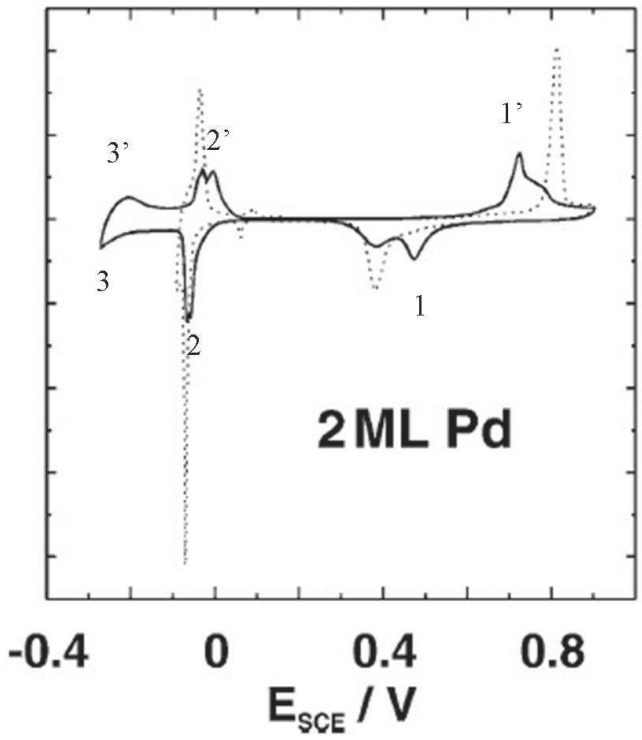

Figure I.3 [47]: Current–potential curves for $Pd_{2\ ML}$/Au(111) in 0.1 M H_2SO_4 after deposition from chloride-containing solution. Scan rate: 10 mV·s^{-1}. The curve for massive Pd(111) is shown as dotted line for comparison.

Baldauf and Kolb [3] studied hydrogen adsorption and absorption on ultrathin Pd overlayers deposited on Au(111) and Au (100) from chloride containing solution. Hydrogen adsorption behavior is strongly influenced by the two surface orientations as well as by the various film thicknesses. The amount of adsorbed hydrogen on the first Pd layer is only about 2/3 of a full monolayer. Hydrogen adsorption is also strongly influenced by the anion in solution: sharp and energetically well confined adsorption peaks are seen in sulfate-containing electrolytes, whereas in perchlorate solutions a rather broad and unstructured adsorption behavior emerges. The voltammograms acquired in 0.1 M H_2SO_4 solution at 5 mV·s^{-1} show that a two monolayers thick Pd films does not absorb hydrogen to any appreciable amount for both Pd/Au(111) and Pd/Au(100). The ability of Pd to absorb hydrogen starts with a thickness of three layers. The H/Pd ratio then increases with Pd film thickness and reaches a limiting value of 0.6 for 100 ML of Pd in acid solution.

Kibler *et al.* [47] compared the electrochemical properties of Pd/Au(111) films deposited from chloride-containing solutions with those of massive Pd(111). The features due to hydrogen desorption are very reproducible and show two peaks in the area -0.05 - 0.05 V *vs.* SCE. They have been attributed to hydrogen adsorption onto bulk Pd and onto pseudomorphic Pd/Au(111) layer. A gradual change to bulk properties has been observed with increasing Pd coverage. The altered electrochemical behavior of the over-layer has been ascribed to changes in the electronic structure due to the substrate induced lateral strains.

Using cyclic voltammetry, ac voltammetry and impedance spectroscopy, Duncan and Lasia [48] studied the hydrogen adsorption and absorption for thin Pd/Au(111) films (0.8–10ML). They found that hydrogen adsorption on palladium is thermodynamically easier in the perchloric than sulfuric acids, although the same total charges are observed in both acids. On the contrary, hydrogen adsorption is more reversible in sulfuric acid than in perchloric acid. Their results also suggest that hydrogen adsorption mechanism might proceed through the indirect and the direct paths, but direct path seems much faster. Contrarily to the results of Baldauf *et al.* [3], hydrogen absorption is found to start already at 2 ML.

The possibility of a direct absorption mechanism in sulfuric acid solution is suggested by Birry *et al.* [49].

Hydrogen adsorption and absorption reactions are indistinguishable for Pd/Au(111) in 0.1 M NaOH solution [50]. Compared to nanometric Pd films on polycrystalline gold substrate, the reactions start at more positive potential and are more reversible. These observations clearly reveal the effect of the substrate. In the presence of benzotriarole (BTA), hydrogen adsorption is partially blocked on Pd/Au (111), while hydrogen absorption kinetics is promoted. The results obtained in the presence of poison point out to the direct H absorption mechanism.

The impedance measurements show that Au substrate has an influence on the hydrogen sorption up to 5 monolayers in NaOH and NaOH + BTA solutions.

I.3 Electrochemical isotherms of H-Pd/Au(111) system

Electrochemical isotherm describes the quantity of absorbed hydrogen in the metallic electrode as a function of the applied potential. It reveals the key information on thermodynamic features of the material studied as well as the potential-composition behaviour. It is used for the assessment of the material's hydrogen storage capacity. Figure I.4 shows both the isotherm of bulk Pd.

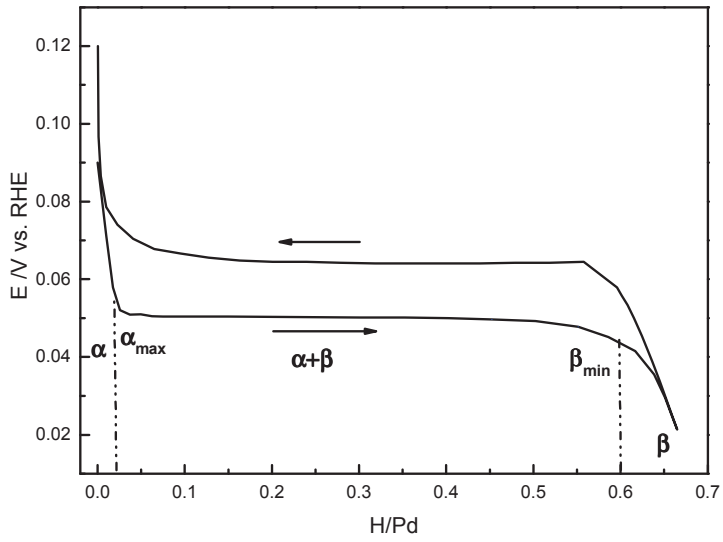

Figure I.4 [16]: Hydrogen absorption-desorption electrochemical isotherm of bulk Pd. α_{max}: maximum solid solution (α phase) solubility; β_{min}: end of the two-phase domain [51]. Arrows indicate reaction direction.

The isotherm is supposed to be a thermodynamic property of the material i.e. we should get a unique value for the inserted hydrogen quantity at a given potential. Indeed, for H insertion in bulk Pd, two values can be measured depending on the measurements is made coming from lower insertion rate (absorption branch) or from higher insertion rate (desorption branch).

Hydrogen absorption in the electrode starts at around +90 mV *vs.* RHE and slowly increases with the decrease of electrode potential down to about +50 mV *vs.* RHE. It corresponds to the formation of the hydrogen solid solution, called α phase. Point α_{max} corresponds to the maximum solid solution hydrogen solubility in the α phase ($\alpha_{max} \approx 0.015$ for bulk Pd) [51]. For higher hydrogen insertion rates, the potential remains constant and the hydride β phase begins. Hydrogen insertion rate reaches point β_{min}, when α phase is totally converted into β phase ($\beta_{min} \approx 0.607$ for bulk Pd) [51]. This last domain, described by a plateau in the isotherm, corresponds to the coexistence of the α and β phases and is referred to as the two-phase domain[d]. Beyond β_{min}, there is a significant decrease in the insertion potential and a solid solution in the β phase forms.

During a complete cycle of insertion/removal, the system Pd-H has a hysteresis phenomenon: the transformation phase desorption occurs at a higher potential (aqueous phase) or a lower equilibrium pressure (gas phase), with respect to the insertion. This behaviour seems to be due to the generation of defects such as dislocations, which can relax the constraints caused by the phase transformation. These constraints are probably caused by changes in the lattice parameter between α and β phases. Contrarily to α phase, corresponding to a lattice parameter expansion less than 2‰, the β phase is characterized by an expansion of about 3.5%.

Substrate can induce major changes in the isotherm behaviour of supported Pd films. Compared to bulk palladium isotherm, it has been shown that the solid solution domain (α phase) is enlarged and total hydrogen solubility is reduced for thin films Pd/Pt(111) [16]. These characteristics are similar to those observed for nano-particles and are hence clearly

[d] According to the Gibbs Phase Rule, $f=k+2-\varphi$, where f is the number of freedom degrees, k is the number of chemical components, ($k=2$ in the present case, for hydrogen and Pd) and φ is the number of phases in the system, ($\varphi=3$ in the present case). As $f=1$ in our system, the hydrogen insertion rate is the only independent parameter, and the potential remains constant in the whole two-phase domain, i. e. a plateau is present.

due to nanosize effects. On the contrary, the important slope measured in the two-phase domain for Pd nanofilms has been attributed to a substrate effect, as shown by the comparison with the isotherm measured for bulk palladium.

Birry *et al.* [49] studied hydrogen insertion into Pd foil and thin films Pd/Au(111) in 0.1 M H_2SO_4 solution. Transient and steady-state techniques are used to describe the hydrogen absorption process. Absorption isotherms have been obtained. The potential, initially fixed in the double layer zone, is cathodically swept down to the potential value in the hydrogen absorption region and hold until equilibrium is reached. The charge corresponding to absorbed hydrogen is evaluated during the anodic sweeping back. The presence of dissolved hydrogen in the solution, which may lead to errors (H_2 oxidation) in the determination of the isotherms, is underlined. Authors claim that the $(H/Pd)_{max}$ values obtained from measurements on Pd/Au(111) from 20 ML up to ~100 nm are similar for all the layers, even if a careful examination of the figure showing the isotherms indicates that hydrogen solubility is smaller for the lowest thickness of 20 ML. The crystal violet seems to have no effects on isotherms, even if kinetics of the hydrogen absorption is significantly enhanced.

Isotherms have also been measured by Martin *et al.* in alkaline solution, 0.1 M NaOH [50]. Contamination problems constrained the authors to “cleaning” and “pre-treatment” procedures before obtaining reproducible isotherms. Contrarily to the isotherms obtained in sulphuric solution, the two-phase plateau is hardly detectable for the thinnest films. No quantitative results on the $(H/Pd)_{max}$ values are reported and commented in the paper and the analysis of the presented isotherms curves does not allow to extract the solubility values for the different thicknesses. They also found that BTA has no effects on isotherm behaviour, in agreement with Birry *et al.* [49].

I.4 Conclusion

Though hydrogen is a promising energy vector for the future, its storage is still a challenge. Metallic hydrides represent an interesting solution. Pd/Au(111) provides a

model for studying hydrogen insertion/desorption process in nanometric systems. Electrochemical Pd deposition represents a relatively easy and reproducible way to obtain thin film. First two monolayers are found to grow layer-by-layer regardless of the anion in solution, even if some authors are not in agreement with such a finding. Chloride-free solution seems to show a higher tendency for three dimensional Pd growth beyond two layers. Contrarily to Pd/Pt(111), there is no clear and unambiguous assignment of the various peaks present in the electrochemical characterization of Pd/Au(111) films in 0.1 M H_2SO_4.

Compared to bulk palladium, Pd/Au(111) shows original (electro)catalytic properties towards various reactions, like ORR, HER, formic acid etc.,…, with activities which are sensitive to film thickness and to the crystal orientation. Hydrogen isotherms have been studied for thin Pd films down to about 10 ML, showing a narrower two-phase plateau and a smaller hydrogen total insertion. Hydrogen insertion into $Pd_{2\ ML}$/Au(111) remains controversial.

Reference:

1 E. Budevski, G. Staikov, W. J. Lorenz, Electrochim. Acta, 45 (2000), 2559.

2 M. Baldauf, D. M. Kolb, J. Phy. Chem., 100 (1996), 11375.

3 M. Baldauf, D. M. Kolb, Electrochim. Acta, 38 (1993), 2145.

4 R. Hoyer, L.A. Kibler, D.M. Kolb, Surf. Sci., 562 (2004), 275.

5 B. Alvarez, V. Climent, A. Rodes, J.M. Feliu, J. Electroanal. Chem., 497 (2001), 125.

6 G. A. Attard, R. Price, A. Al-Akl, Electrochim. Acta, 39 (1994), 1525.

7 N. M. Markovic, C. A. Lucas, V. Climent, V. Stamenkovic, P. N. Ross, Surf. Sci., 465 (2000), 103.

8 M. Arenz, V. Stamenkovic, T. J. Schmidt, V. Stamenkovic, P. N. Ross, Surf. Sci., 523 (2003), 199.

9 B. Alvarez, V. Climent, A. Rodes, J. M. Feliu, Phy. Chem. Chem. Phy., 3 (2001), 3269.

10 R. Hoyer, L. A. Kibler, D. M. Kolb, Electrochim. Acta, 49 (2003), 63.

11 J. Kolaczkiewicz, E. Bauer, Surf. Sci., 374 (1997), 95.

12 I. M. Abdelrehim, K. Pelhos, T. E. Madey, J. Eng, J. G. Chen, J. Mol. Catal. A-Chem., 131 (1998), 107.

13 R. Hoyer, L. A. Kibler, D. M. Kolb. Surf. Sci., 562 (2004), 275.

14 A. Beutler, A. Sandell, A. J. Jaworowski, M. Wiklund, R. Nyholm, J. N. Andersen, Surf. Sci., 418 (1998), 457.

15 A. Beutler, F. Strisland, A. Sandell, A. J. Jaworowski, R. Nyholm, M. Wiklund, J. N. Andersen. Surf. Sci., 411 (1998), 111.

16 C. Lebouin, Y. Soldo-Olivier, E. Sibert, P. Millet, M. Maret, R. Faure, J. Electroanal. Chem., 626 (2009), 59.

17 C. Lebouin, Y. Soldo-Olivier, E. Sibert, M. De Santis, F. Maillard, R. Faure, Langmuir, 25 (2009), 4251.

18 Y. Soldo-Olivier, M. C. Lafouresse, M. De Santis, C. Lebouin, M. de Boissieu, E. Sibert, J. Phys. Chem. C, 115 (2011), 12041.

19 D. Cherns, M. J. Stowell, Thin Solid Films, 29 (1975), 127.

20 J. V. Barth, H. Brune, G. Ertl, Phys. Rev. B, 42 (1990), 9307.

21 J. T. Sun, L. Gao, X. B. He, Z. H. Cheng, Z. T. Deng, X. Lin, H. Hu, S. X. Du, Feng Liu, H. J. Gao, Phy. Rev. B, 83 (2011), 115419.

22 F. Besenbacher, J. V. Lauritsen, T. R. Linderoth, E. Lægsgaard, R.T. Vang, S. Wendt, Surf. Sci., 603 (2009), 1315.

23 K. Yagi, K. Takayanagi, K. Kobayashi, N. Osakabe, Y. Tanishiro, G. Honjo, Surf. Sci., 86 (1979), 174.

24 A. W. Stephenson, C. J. Baddeley, M. S. Tikhov, R. M. Lambert, Surf. Sci., 398 (1998), 172.

25 L. A. Kibler, M. Kleinert, R. Randler, D. M. Kolb, Surf. Sci., 443 (1999),19.

26 H. Naohara, S. Ye, K. Uosaki, J. Phys. Chem. B, 102 (1998), 4366.

27 H. Naohara, S. Ye, K. Uosaki, Colloid Surface A, 154 (1999), 201.

28 M. Takahasi, Y. Hayashi, J. Mizuki, K. Tamura, T. Kondo, H. Naohara, K. Uosaki, Surf. Sci., 461 (2000), 213.

29 T. Kondo, K. Tamura, M. Takahasi, J. Mizuki, K. Uosaki, Electrochim. Acta.,47 (2002), 3075.

30 M. Takahasi, K. Tamiral, J. Mizuki, T. Kondo, K. Uosaki, J. Phys. Condens. Matter, 22 (2010), 474002.

31 S. Takakusagi, K. Kitamura, K. Uosaki, Electrochim. Acta, 54 (2009), 5137.

32 J. Tang, M. Petri, L. A. Kibler, D. M. Kolb, Electrochim. Acta, 51 (2005), 125.

33 C. Kontje, L. A. Kibler, D. M. Kolb, Electrochim. Acta, 54 (2009), 3830.

34 R. M. Ormerod, C. J. Baddeley, R. M. Lambert, Surf. Sci. 259 (1991), L709.

35 B. E. Koel, A. Selidj, M. T. Paffett, Phy. Rev. B, 46 (1992), 7846.

36 T. J. Schmidt, V. Stamenkovic, N. M. Markovic, P. N. Ross, Electrochim. Acta, 48 (2003), 3823.

37 L. A. Kibler, M. Kleinert, D. M. Kolb, Surf. Sci. 461 (2000), 155.

38 S. Pandelov, U. Stimming, Electrochim. Acta, 52 (2007), 5548.

39 M. E. Quayum, S. Ye, K. Uosaki, J. Electroanal. Chem., 520 (2002), 126.

40 A. J. Bard & L. R. Faulkner, Eds. D. Harris, E. Swain, E. Aiello, Electrochemical Methods: Fundamentals and Applications (2nd), New York: John Wiley & Sons, 2001, 564-551.

41 A. M. El-Aziz, L.A. Kibler, D. M. Kolb, Electrochem. Commun., 4 (2002), 535.

42 H. Naohara, S. Ye, K. Uosaki, Electrochim. Acta, 45 (2000), 3305.

43 A. M. El Aziz, L. A. Kibler, J. Electroanal. Chem., 534 (2002), 107.

44 H. Naohara, S. Ye, K. Uosaki, J. Electroanal. Chem., 500 (2001), 435.

45 L. A. Kibler, Electrochim. Acta, 53 (2008), 6824.

46 A. Roudgar, A. Groß, J. Electroanal. Chem., 548 (2003), 121.

47 L. A. Kibler, A. M. El-Aziz, D. M. Kolb, J. Mol. Catal. A, 199 (2003), 57.

48 H. Duncan, A. Lasia, Electrochim. Acta, 52 (2007), 6195.

49 L. Birry, A. Lasia, Electrochim. Acta, 51 (2006), 3356.

50 M. H. Martin, A. Lasia, Electrochim. Acta, 54 (2009), 5292.

51 B. D. Adams, A. Chen, Mater. Today, 14 (2011), 283.

Chapter II. Palladium deposition on Au(111)

Electrochemical deposition of Pd nanofilms onto Au(111) can be quite easily performed in a chemical laboratory in a reproducible way. This method was previously used by ESME team (Electrochimie des Systèmes Métalliques et Electrocatalyse) in LEPMI for Pd/Pt(111) films studies [1]. The signature obtained by cyclic voltammetry in sulphuric acid solution was used as a first tool to check the smoothness of the Pd deposit. We decided to use a similar approach for Pd deposition onto Au(111). After a review of the experimental methods and setup, we will first show in this chapter the electrochemical deposition and dissolution studies of Pd layers. We will then discuss the best parameters selection to perform nanofilms deposition. Electrochemical signatures of the films in sulphuric acid with and without chloride and also in perchlorate acid solutions will be shown. The assignment of the various features present in the cyclic voltamperometry to specific reactions after detailed qualitative and quantitative analysis of the electrochemical characterizations will be discussed.

II.1 Experimental setup

Experiments were performed with Par 273 A (EG&G, Princeton Applied Research) Potentiostat. A Saturated Calomel Electrode (SCE) was used as reference electrode (RE). For a better comparison, especially with reactions involving hydrogen, all potentials are quoted versus the Reversible Hydrogen Electrode (RHE)[a]. A Pt sphere electrode connected with the reference electrode through capacitors was used as auxiliary electrode (AE) to filter the noise in the circuit [2]. A Pt grid electrode was employed as counter

[a] $E\ (vs.\ RHE) = E\ (vs.\ SCE) + 0.2412\,V + 0.0591 \cdot pH$, where pH is a measure of the protons activity (activity is close to concentration for dilute solution). According to the corresponding equilibrium constant (K_2=1.2×10^{-2} at 298.15 K), the approximate value for [H^+] is 0.11 M in 0.1 M H_2SO_4 and 0.1 M in $HClO_4$. Hence $E\ (vs.\ RHE) = E\ (vs.\ SCE) + 0.2978\ V$ in 0.1 H_2SO_4 and $E\ (vs.\ RHE) = E\ (vs.\ SCE) + 0.3002\ V$ in 0.1 M $HClO_4$.

electrode (CE). Two classic glass (pyrex) electrolyte cells were used in the experiment, one for Pd deposition and the other for films characterization. Palladium ultra-thin films deposition onto single crystals is very sensitive to contamination. For this reason, all the containers and apparatus that are in contact with solution during the experiment were previously immersed into condensed chromate acid for more than one night, i.e. the two electrolytic cells (5 outlets), volumetric flasks (200 mL) for making up solutions, beakers (100 ml) and graduated pipette (1 ml, ±0.01 ml) for solution transferring, Pt counter and auxiliary electrodes and plastic nipper for handling crystal. After this procedure they were carefully rinsed with ultra-pure water and filled with or immersed in water to avoid contamination before their employing.

Ultra pure water (Milli-Q, 18.2 MΩ·cm, 3 ppb TOC [b]) was used for washing the apparatus and preparing solutions. We employed high purity reagents: H_2SO_4 (96%, Suprapur, Merck), $PdCl_2$ (Zur Synthese, Merck), HCl (30%, Suprapur, Merck) and $HClO_4$ (70%, Suprapur, Merck). 0.1 M H_2SO_4 + 0.1 mM $PdCl_2$ + 3 mM HCl and 0.1 M H_2SO_4 solutions were prepared for Pd deposition and characterization, respectively. Ar (>99.9999%, Messer) was used for deoxygenating the solution. Ar stream was charged into solution directly before experiment started, then it worked as a protection gas beyond solution. Cleanness of 0.1 M H_2SO_4 solution was checked by cyclic voltammetry using Pt polycrystalline electrode as working electrode. For a non-contaminated Pt electrode, the voltammogram should be the same as the referenced one.

One Au cylindrical single crystal (5 mm diameter and 4 mm height, MaTecK Jülich, Germany) was used as working electrode (WE). One surface of the cylinder is oriented along the (111) crystallographic direction better than 0.1° and polished down to 0.03 μm. The crystal was attached to a gold wire for an easier handling. To get a well ordered Au(111) surface, the crystal was flame annealed before each experiment. It was heated

[b] Total Organic Carbon

with a butane/air flame till it became red; this status was kept for ~2 minutes, and then it was cooled down in air. The crystal was then transferred to the electrolytic cell containing well deoxygenated 0.1 M H_2SO_4 solution for surface checking. It was dipped into the electrolyte and was heaved up until only the (111) surface were in contact with the electrolyte (Figure II.1).

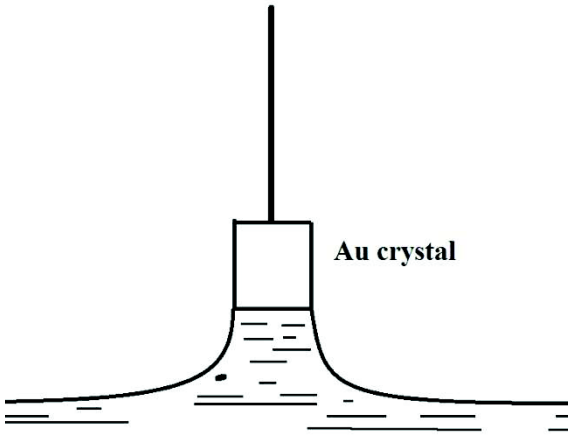

Figure II.1: Schematic of Au(111) surface contacts with solution.

Au(111) surface in electrochemical environment is unreconstructed at potentials more positive than a critical (electrolyte-dependent) potential, whereas at more negative potentials herringbone surface reconstruction is formed, as it is similarly observed under UHV conditions (see paragraph I.1) [3,4,5]. Theoretical studies suggest that this potential induced phase transition is due to the adsorption of anions [6].

A typical votammogram of annealed Au(111) in sulfate solution is shown in Figure II.2. The anodic peak 1 around 0.596 V is assigned to the reconstruction of the Au(111) surface from $\sqrt{3}$ ×22 to 1×1 and the corresponding peak 1' shows the reverse process. The anodic spike 2 at 1.096 V is associated to the adsorbed sulfate's phase transition from disordered to ($\sqrt{3}$ ×$\sqrt{7}$) R19.1° ordered structure. The two anodic peaks 1 and 2 are very sensitive to the presence of defects on the Au(111) surface, so they can be used as indicators for the quality of the electrode's surface [7]. While the number of defects on the

surface increases, peak 1 becomes broader and the amplitude decreases. Peak 2 intensity is relied to the average width of (111) terraces on the surface: the higher the spike, the larger the terraces' width. Figure II.2 shows the characterization of a crystal with a relatively high surface quality.

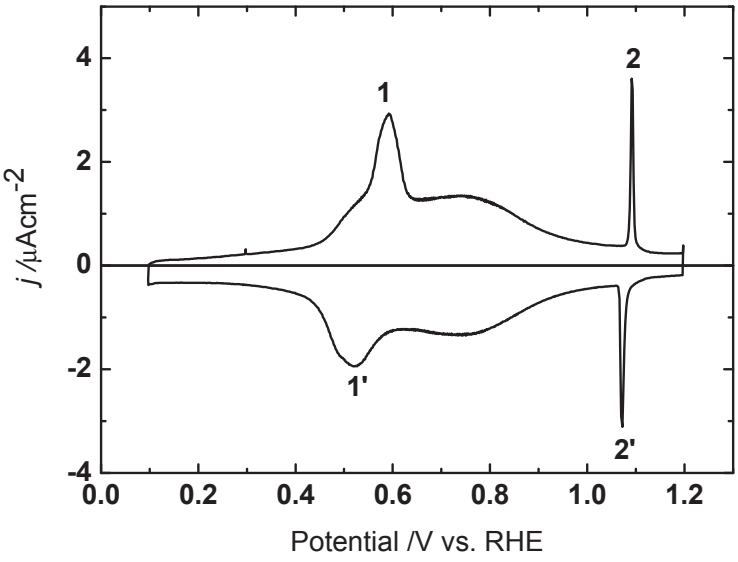

Figure II.2: Cyclic voltammogram of Au(111) in 0.1 M H_2SO_4 solution, scan rate 10 mV·s^{-1}.

After Au(111) surface electrochemical characterization, the crystal was transferred to the second electrolyte cell filled with solution containing $[PdCl_4]^{2-}$. Once Pd layers deposition completed, the crystal was moved out and rinsed carefully to remove $[PdCl_4]^{2-}$ and transferred for electrochemical characterization to the previous electrolyte cell, filled with 0.1 M H_2SO_4. Recorded voltammograms inform about the surface morphology of the Pd film. At the end of each experiment, Pd deposit was removed from Au(111) substrate by applying a potential of +3 V in 1 M $HClO_4$ solution and dissolving the surface oxide in 1 M HCl solution (this procedure is repeated three times).

The success of the experiment is made sure only carefully following step by step the described procedures.

All the experiments were performed at the room temperature.

II.2 Palladium deposition

In order to have an overview of the mechanisms underlying Pd electro-deposition, we studied cyclic voltammograms of Au(111) crystal in Pd^{2+} containing solution. We firstly focused on the first under potentially deposited Pd monolayer, which is expected to have a different mechanism compared to bulk deposition. Then, we have considered the deposition of several layers.

II.2.1 Cyclic voltammetry study

Information about mechanisms for both Pd deposition and dissolution can be extracted from cyclic voltammetries, as for example the potential values for under potential deposition or bulk deposition (also called over potential deposition, OPD).

According to the work of Kolb *et al.* [8], we considered a rather low value for the Pd deposition sweep rate (0.1 $mV \cdot s^{-1}$) in order to obtain a good description of each deposition/dissolution step. Figure II.3 shows the cyclic voltammogram of Au(111) in 0.1 M H_2SO_4 + 0.1 mM $PdCl_2$ +3 mM HCl. The crystal was dipped into the solution at 0.998 V *vs.* RHE. At this potential, Au(111) is unreconstructed with a (1x1) structure, as mentioned in the experimental paragraph. During the first cycle, potential decreases down to 0.667 V *vs.* RHE and goes back to 0.998 V *vs.* RHE. While potential sweeps back, the current curve crosses the line I = 0 A and this intersection point corresponds to the equilibrium Nernst potential[c]: E_{Nernst} = 0.778 V *vs.* RHE. Deposition occurring at higher potential than Nernst potential is ascribed to UPD, while deposition made at lower values is assigned to OPD.

[c] The value obtained here is not strictly equal to the Pd/Pd^{2+} Nernst potential, as the reaction does not probably reach equilibrium during the potential scan. Nevertheless, the sweep rate being very slow, the difference of Pd^{2+} concentration is very small between bulk solution and surface during the potential sweeping back to high potential. Thus the Nernst potential obtained by this method should be very close to the true value.

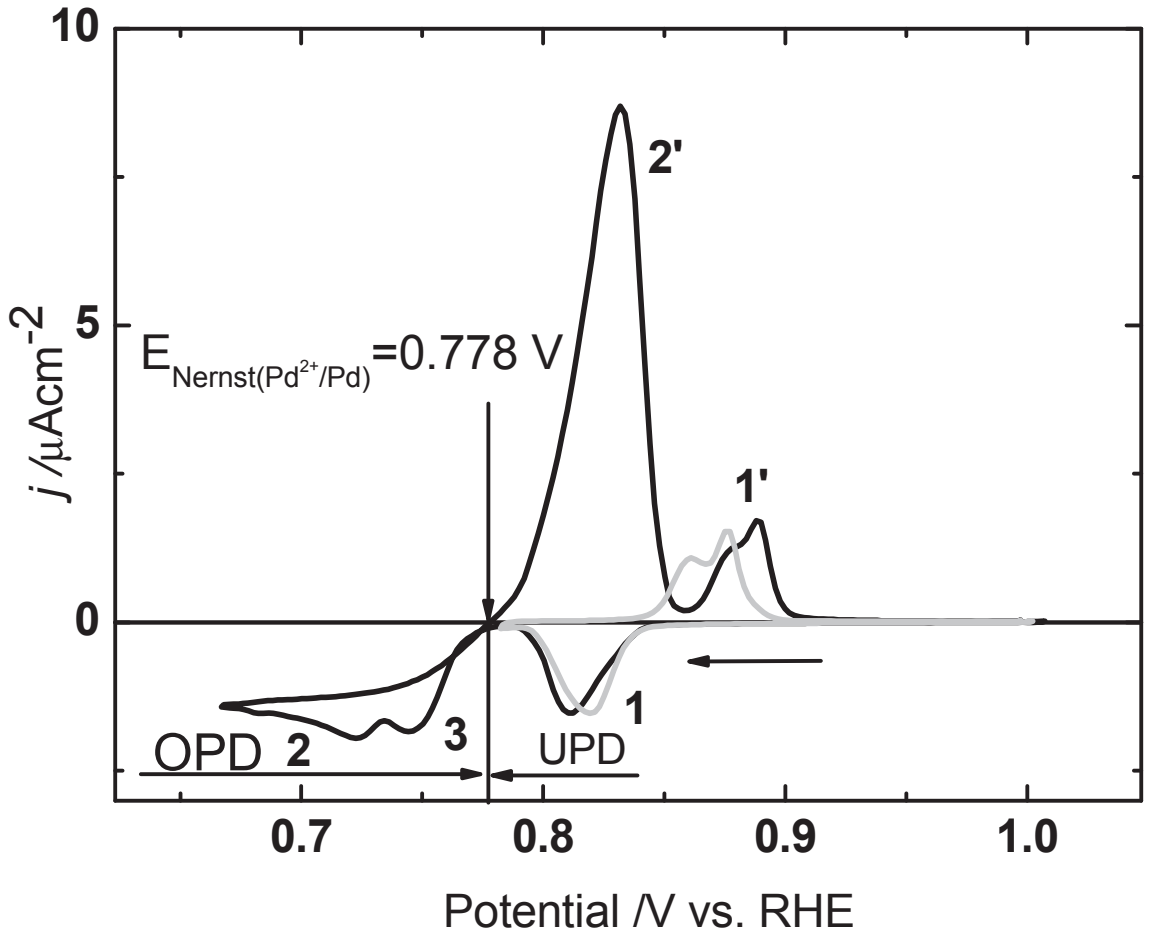

Figure II.3: Cyclic voltammograms of Au(111) in 0.1 M H_2SO_4 + 0.1 mM $PdCl_2$ + 3 mM HCl. Black line: 1st cycle; light grey line: 2nd cycle. Scan rate: 0.1 mV·s^{-1}.

At this very low scan rate (ν = 0.1 mV·s^{1}), three well-defined deposition peaks are present. One peak is in the UPD region, centered at about 0.812 V *vs.* RHE; while two peaks are well seen in the OPD region, at about 0.744 V *vs.* RHE and 0.722 V *vs.* RHE, corresponding to the presence of at least two different stages in bulk deposition. Deposition current reaches its limit, -1.5 μA·cm^{-2}, below 0.67 V *vs.* RHE. In the anodic scan, peaks 2' (0.831 V *vs.* RHE) and 1' (0.888 V *vs.* RHE) seem to correspond to the OPD and UPD dissolution, respectively. While the potential range is restricted to UPD regime (light gray line in Figure II.3), the peaks 1/1' (UPD deposition/dissolution) become more reversible. It seems like the reversibility of these peaks were affected by OPD deposition/dissolution in 1st cycle, maybe due to the presence of different adsorbed

species or to morphological modification of the substrate. It is also interesting to remark that there is a shoulder on peak 1', probably convoluted in peak 1 during the cathodic sweeping, which has already been observed by Kibler *et al.* [8] and attributed to dissolution/deposition on steps.

The quantity of deposited Pd atoms was monitored with the integral charge q measured at the electrode. One complete Pd monolayer corresponds to a charge q_{ML}=444.38 $\mu A \cdot cm^{-2}$, assuming a pseudomorphic deposition (1 Pd atom for each Au atom) and two exchanged electrons for each deposited Pd. In the following, palladium coverage will be expressed as an equivalent number x of complete monolayers corresponding to the measured charge $q=x \cdot q_{ML}$. Hence, x ML do not refer to the real number of fully deposited atomic layers. In the following, Pd deposits will be referred to as $Pd_{x\ ML}$/Au(111).

The current and charge variations with time during the 1st and 2nd cycle are displayed in Figure II.4 and Figure II.5, respectively. The charge density calculated under peak 1 corresponds very closely to the deposition charge for a complete pseudomorphic Pd monolayer on Au(111) in both cycles. Thus peak 1 is ascribed to the first complete adlayer deposition. Taking the boundary between peaks 2 and 3 at 2959 seconds (cf. Figure II.4, minimum current value), the integral charge under peak 2 is 495 $\mu C \cdot cm^{-2}$. Even if this charge estimation is affected by the overlap with higher layers (peak 3), it well corresponds to the deposition of the complete second Pd layer.

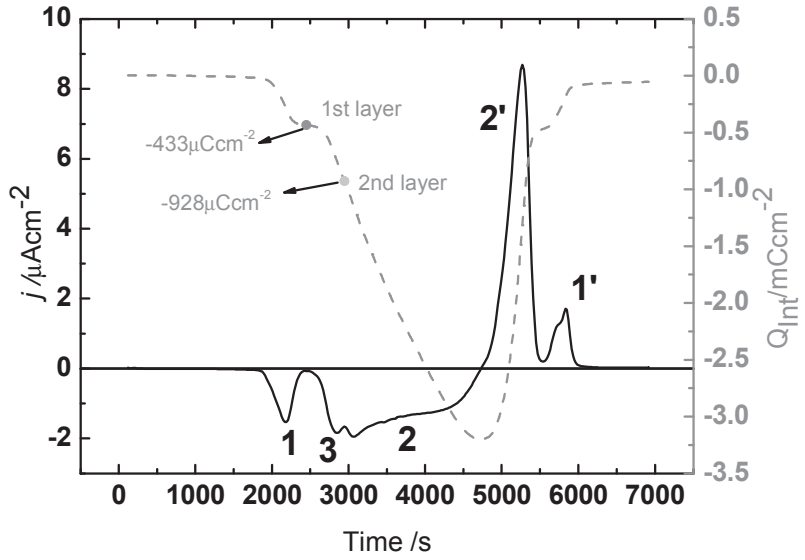

Figure II.4: Current and charge as a function of time during the first cycle in Figure II.3. Solid line: current; dashed line: charge.

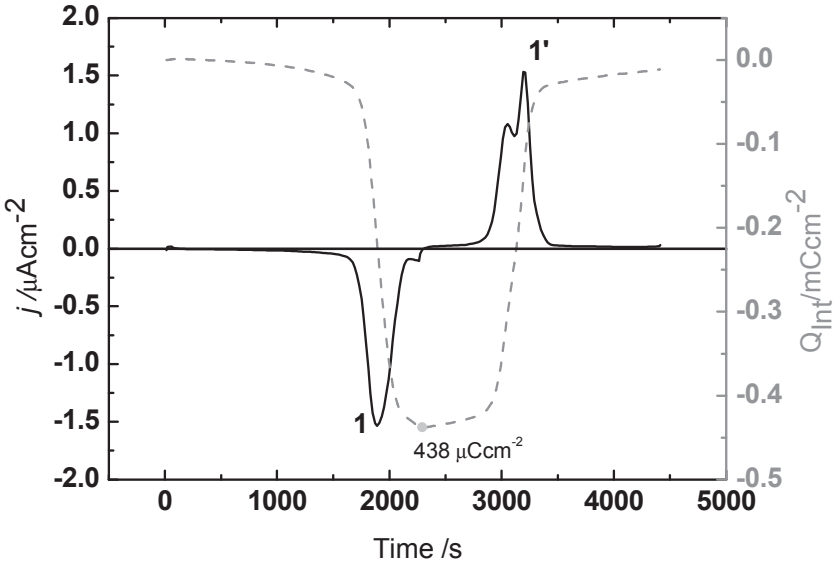

Figure II.5: Current and charge as a function of time for second cycle in Figure II.3. Solid line: current; dash line: charge.

The integrated charge under each peak in Figure II.3 is displayed in Table II.1.

		Cathodic /μC·cm^{-2}	Anodic /μC·cm^{-2}
1st monolayer	1st cycle	433	415
	2nd cycle	438	427
2nd monolayer		495	
OPD		2758	2730

Table II.1: Integral charge under each peak in Figure II.3.

The charges under anodic peaks are slightly smaller than for the corresponding cathodic peaks. We cannot exclude that the deposited Pd atoms have not completely been dissolved, but the experimental uncertainties and oxygen traces contribution amplified by slow scan rate do not allow concluding about that.

Figure II.6 shows Au(111) electrochemical characterization in 0.1 M H_2SO_4 before and after several palladium depositions and dissolutions (4 UPD deposition/dissolution and 1 UPD+OPD deposition/dissolution) in 0.1 mM $[PdCl_4]^{2-}$ containing solution.

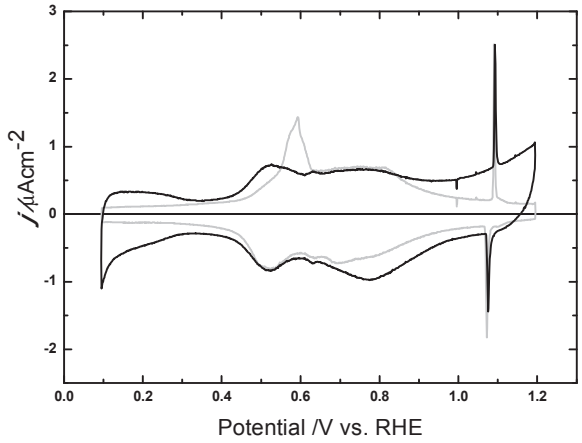

Figure II.6: Voltammograms of Au(111) in 0.1 M H_2SO_4. Light grey line: Au(111); black line: Au(111) after several palladium depositions and dissolutions in 0.1 M H_2SO_4 + 0.1 mM $PdCl_2$ + 3 mM HCl. Scan rate: 5 mV·s^{-1}.

The comparison reveals that Au(111) surface is modified after cycling, nevertheless well ordered (1x1) terraces must still be present on the Au surface. Indeed, even if the Au surface reconstruction peak around 0.60 V *vs.* RHE is deeply reduced and shifted, the adsorbed sulfate phase transition spike around 1.09 V *vs.* RHE is still pronounced.

An important difference between voltammetries is observed in the 0.1-0.42 V *vs.* RHE region. The capacitance of this area for Au(111) is about 25 $\mu F \cdot cm^{-2}$ and can be easily ascribed to the double layer capacitance (usually 20~60 $\mu F \cdot cm^{-2}$). After Pd deposition/dissolution cycles the integrated cathodic charge (0.15~0.4 V *vs.* RHE) significantly increases by a factor ~2.6, from ~7.3. $\mu C \cdot cm^{-2}$ up to ~18.7 $\mu C \cdot cm^{-2}$. This finding cannot be simply assigned to an important increase of the active surface, which would result in the disappearance of the adsorbed sulfate transition spike. We think that the measured current is due to hydrogen adsorption onto Pd atoms, which are not completely removed after the dissolution procedure. Tang *et al.* pointed out that $[PdCl_4]^{2-}$ may be still adsorbed on the Au surface after deposition/dissolution cycle from chloride solution, even with thorough rinsing by water [9]. Incomplete Pd dissolution or Pd-Au alloy formation cannot be excluded, as well. Considering that one hydrogen atoms adsorption involves only one Pd atom, we can estimate from the integrated charge that Pd atoms occupy about 4% of the gold surface. However, we underline that the estimated Pd coverage may change from one experiment to another. The presence of Pd atoms on the gold surface is also supported by the observation that a cathodic current tends to appear at the lowest potentials, possibly corresponding to hydrogen evolution reaction (HER).

Pd atoms can also modify the gold surface reconstruction, as shown by Stephenson *et al.* [10]. They studied the nucleation and growth of Pd films on reconstructed $22\times\sqrt{3}$ Au(111) substrates during deposition in UHV and demonstrated that there exist important interactions between deposited layer and substrate, modifying each other's structure. In particular, they find that Pd deposition induces the partial redirection of surface ridges on Au surface, which affects the morphology of Pd islands in turn.

In order to observe the effects of surface structural evolution due to Pd desorption/dissolution cycles on Pd deposition itself, we recorded successive cyclic voltammograms of Au(111) in 0.1 M H_2SO_4 + 0.1 mM $PdCl_2$ + 3 mM HCl (Figure II.7).

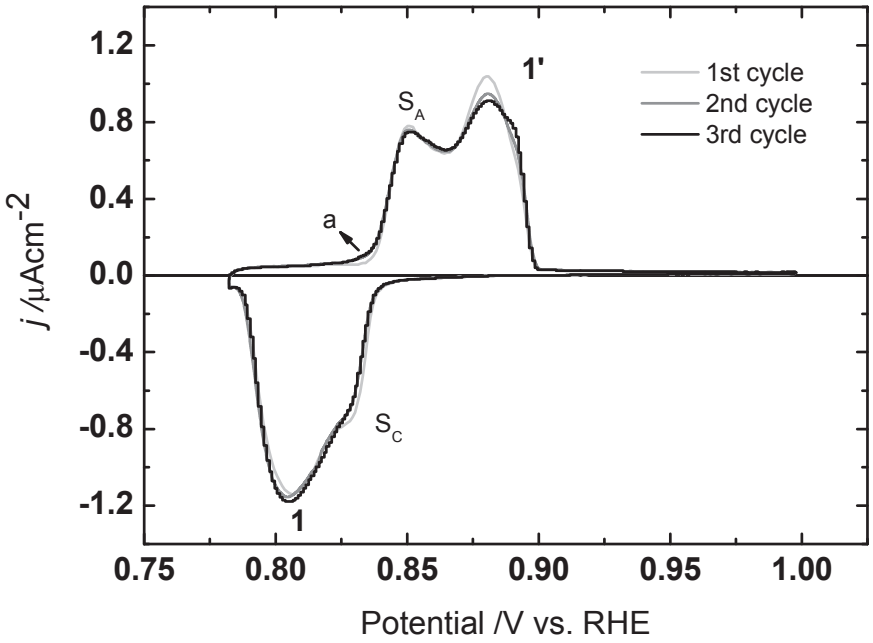

Figure II.7: Cyclic voltammograms of Au(111) in 0.1 M H_2SO_4 + 0.1 mM $PdCl_2$ + 3 mM HCl; sweep rate: 0.1 mV·s^{-1}.

Peaks 1/1' correspond to Pd deposition/dissolution on Au(111) terraces, while the shoulder S_C and the corresponding peak S_A have been ascribed to Pd deposit and dissolution on steps, respectively [8]. Cyclic voltammograms show that Pd dissolution on terraces decreases somewhat already after one cycle; deposition on steps sites is also affected. These curves are in agreement with a description of a slightly incomplete Pd dissolution process.

As shown in the last section, Nernst potential divides Pd bulk deposition from UPD, where UPD corresponds to one monolayer deposition. Thus one monolayer can be easily obtained by setting the potential at the Nernst potential.

Let's look more closely at this first step of the deposition. Figure II.8 shows the curve of deposition obtained by a potential step from 0.998 V *vs.* RHE, where no deposition occurs, down to 0.798 V *vs.* RHE, a potential value where the UPD voltammetric deposition is not yet completed (cf. figure II.7).

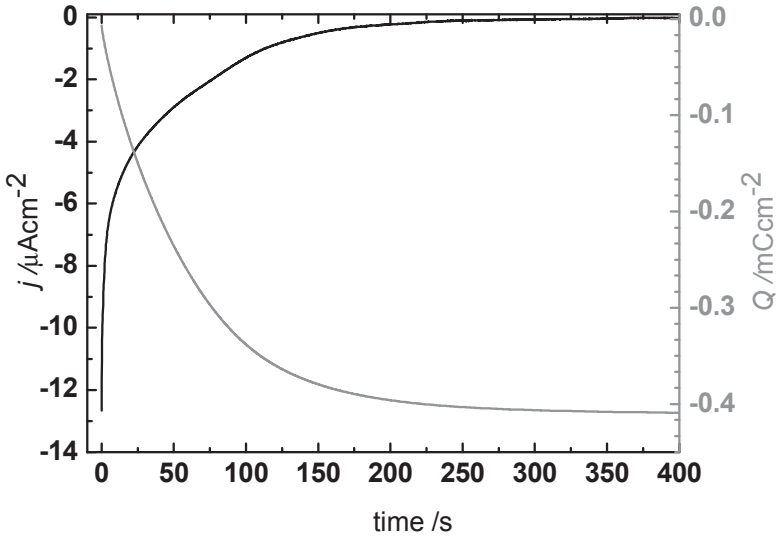

Figure II.8: Au(111) in 0.1 M H_2SO_4 + 0.1 mM $PdCl_2$ + 3 mM HCl. chronoamperometry at 0.798 V *vs.* RHE. Black: I-t curve; Grey: Q-t curve.

The current quickly decays from a relatively high value (~13 $\mu A \cdot cm^{-2}$)[d] down to 0 in around 300 s. As the integrated charge shows, the deposition completed in this time interval corresponds very closely to the theoretical value of one monolayer, with a total deposited charge of 413 $\mu C \cdot cm^{-2}$. The UPD character of the deposition is revealed by the fact that no further OPD deposition occurs at this potential once the 1st monolayer is completed. In conclusion, one complete Pd layer can be prepared with both voltammetry and chronoamperometry, once Nernst potential is not overcome.

[d] Due to time resolution limitation of the potentiostat, the initial current value is actually not exactly known. See chapter III.2.4.

As the second layer contribution is revealed by a pronounced peak (peak 3 in figure II.3), we wandered if it had an UPD character as well, shifted in the OPD region due to a kinetic effect. Our measurements showed that Pd deposition never stops once Nernst potential is overcome, even in correspondence of the well-defined peak for the 2nd layer. Finally, only the first monolayer can be precisely separated from following deposited layers.

In the following, only voltammetry will be applied for deposition of low thickness films (<3ML), while both voltammetry and chronoamperometry at 0.718 V *vs.* RHE (diffusion limited current) will be used for thicker films, as shown in Figure II.9.

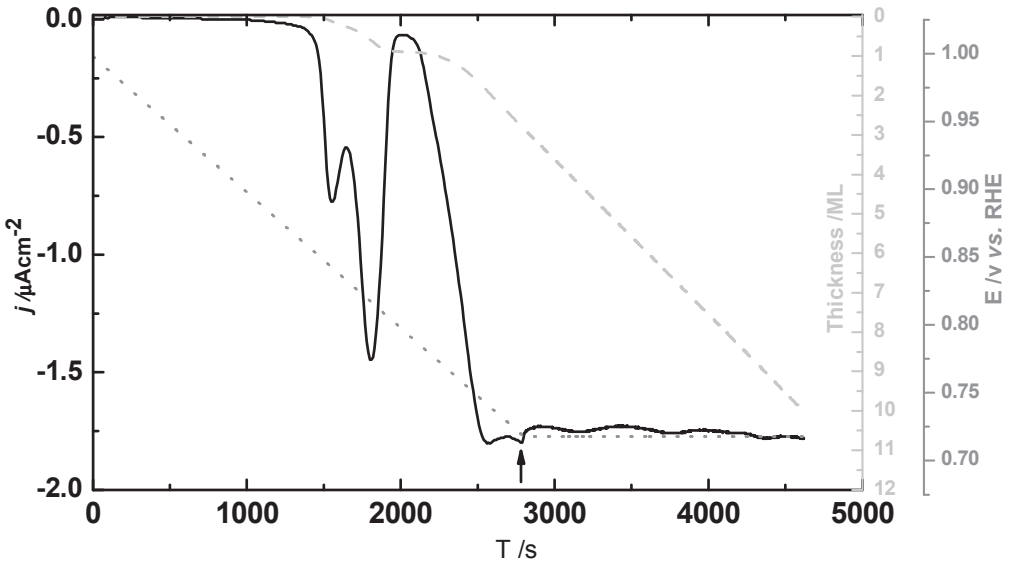

Figure II.9: Typical deposition curve in 0.1 M H_2SO_4 + 0.1 mM $PdCl_2$ + 3 mM HCl solution. Au(111) electrode is dipped into the solution at 0.998 V *vs.* RHE. The potential is swept down to 0.718 V *vs.* RHE with a scan rate of 0.1 mV·s^{-1} and hold at 0.718 V *vs.* RHE until the desired amount of Pd is deposited. Solid line: current; dashed line: integrated charge; dotted line: applied potential; Arrow indicates the onset of CA deposition.

To summarize, we have shown that Pd deposition proceeds through UPD for the first adlayer, followed by OPD. First under potentially deposited monolayer can be obtained

both by voltamperometry or chronoamperometry. Films thicker than about 3ML are obtained by CV down to diffusion limited current, followed by CA until the obtainment of the wished thickness. Our results curves are in agreement with the description of a slightly incomplete Pd dissolution process.

II.3 Electrochemical characterization of Pd films

The voltammogram for $Pd_{1\ ML}$/Au(111) in 0.1 M H_2SO_4, deposited from chloride containing solution, is displayed in Figure II.10.

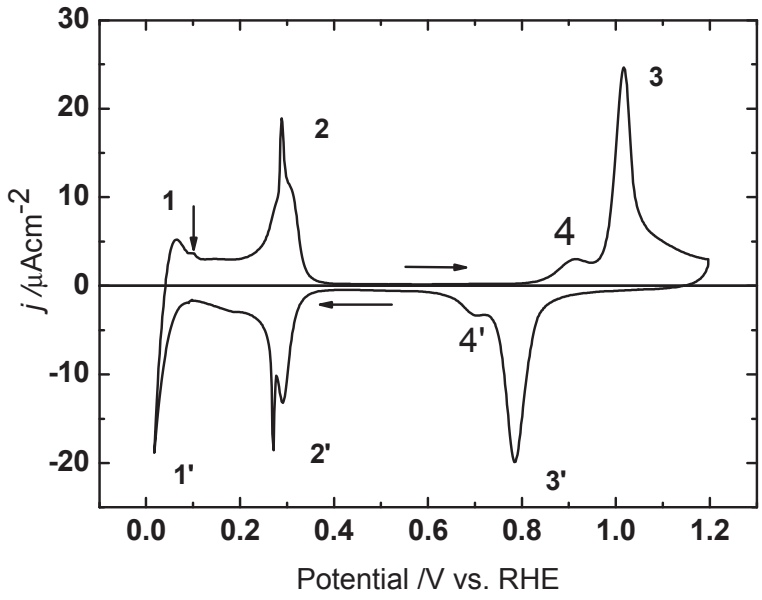

Figure II.10: Voltammogram of $Pd_{1\ ML}$/Au(111) in 0.1 M H_2SO_4. The scan onset is indicated by the vertical arrow. Sweep rate: 5 mV·s^{-1}.

When the first Pd monolayer is completed, no Au(111) surface characteristic peaks are distinguishable (cf. Figure II.2). So, the current–potential curve reflects the complete covering of the substrate as seen by STM [8,11]. The features in the region at potentials below 0.5 V *vs.* RHE have been already described by several authors [8,9,11]. They have been ascribed to hydrogen and sulfate adsorption/desorption reactions (peaks 2'/2) and hydrogen insertion/desorption (peaks 1'/1). Surface oxidation (or OH adsorption) of the

first Pd monolayer occurs at around 1.0 V *vs.* RHE, the pre-peak at 0.9 V *vs.* RHE being associated to the oxidation occurring at mono-atomic high steps, according to STM data [8]. The same was observed for the surface oxidation of bulk Pd(111), where defects are preferentially oxidized [12]. Finally, surface oxidation and reduction (peak 3/3' and peak 4/4') seem to be less reversible than hydrogen adsorption and desorption (peak 2/2').

II.3.1 Potential range for stable electrochemical characterization

We wanted to determine the largest potential window in which the electrochemical signature of the sample can be recorded without damaging it.

Pd dissolution at high potential

It is interesting to investigate the effects of oxidation at high potentials on the stability of Pd films. Several cycles were performed on $Pd_{1\ ML}$/Au(111) in 0.1 M H_2SO_4, as displayed in Figure II.11.

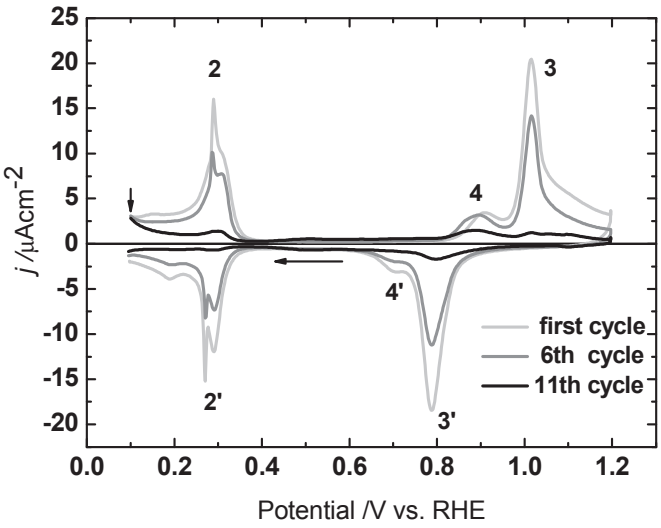

Figure II.11: Cyclic voltammogram of $Pd_{1\ ML}$/Au(111) in 0.1 M H_2SO_4, scan rate 5 mV·s^{-1}. Arrows indicate the onset and sweep direction.

Excursion of potential up to 1.2 V *vs.* RHE and subsequent oxide reduction leads to a significant decrease of the voltammetric peaks, both in the hydrogen desorption/adsorption region near 0.25 V *vs.* RHE and in the oxide zone. The initial signature of the Pd film as described in the previous paragraph almost totally disappears after about 11 cycles. This behavior indicates that repeated oxidation–reduction cycles in 0.1 M H_2SO_4 lead to a gradual dissolution of palladium. Since Pd forms a rather stable oxide already at around 1.0 V, our findings show that the dissolution kinetics of Pd in 0.1 M H_2SO_4 is extremely slow. The corresponding decrease of the peaks intensity in the hydrogen desorption/adsorption region seems to indicate that adsorbed hydrogen is proportional to the amount of Pd atoms on the surface. The peak at 0.9 V *vs.* RHE (peak 4/4'), which is related to oxide formation at defects, decreases as well, but proportionally less than the main peak, which would correspond to the formation of many defects during dissolution.

In order to avoid the destructive action of Pd dissolution, we have restricted the potential range during electrochemical characterization to the ion adsorption zone ($E < 0.5$ V *vs.* RHE).

Hydrogen evolution/insertion at low potential

As Figure II.12 shows, the cathodic current increases in the lowest potential region between 0.1 V and 0.02 V *vs.* RHE. This behavior is due to hydrogen evolution reaction, which starts at around 0.08 V *vs.* RHE for Pt(111). After cycling down to more negative potential values, the surface is "cleaner", as shown by the enhanced intensity of the peaks, probably corresponding to the desorption of contaminating anions (i.e. Cl^-). Nevertheless, hydrogen evolution and hydrogen insertion, observed at lower potential values than about 0.1 V *vs.* RHE for Pd films with higher thickness than 2 ML (see Figure IV.6), may degrade the Pd film.

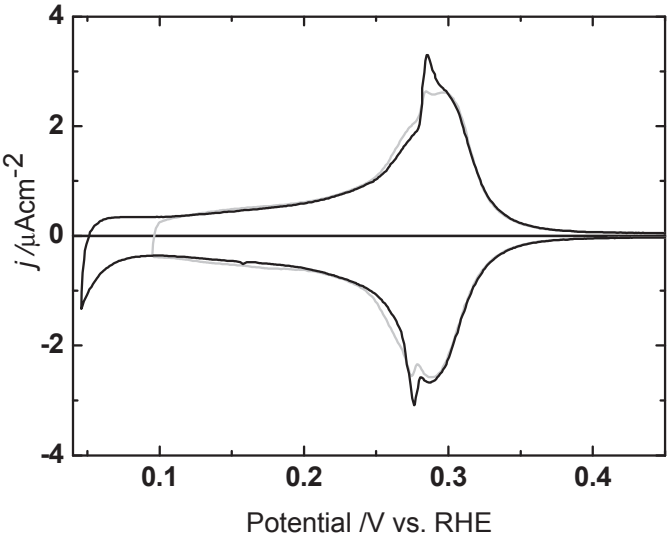

Figure II.12: Voltammograms of $Pd_{1\ ML}$/Au(111) in 0.1 H_2SO_4 with different potential ranges. First stable cycle (light grey line) is followed by the cycle in the lowest potential region (black line) Sweep rate: 20 mV·s^{-1}.

In particular, if the deformation of Pd film caused by hydrogen absorption/desorption exceeds the elastic range, it may introduce permanent deformation, as will be discussed in detail in chapter IV. For this reason, during the recording of Pd film electrochemical signature, we will consider 0.1 V *vs.* RHE as the lowest potential limit.

II.3.2 **Pd film stability**

Figure II.13 shows the cyclic voltammogram of $Pd_{1\ ML}$/Au(111) in 0.1 M H_2SO_4 in the hydrogen adsorption/desorption region. The curve shows evident evolution before reaching a stable state. Peaks intensity increases in the range [0.24, 0.35] V *vs.* RHE and decreases around 0.2 V *vs.* RHE. Cleaning of the surface with cycling should contribute to the observed behaviour, even if some reorganisation of the adsorbed Pd atoms on the gold surface cannot be excluded. Indeed, such behaviour has already been observed by Duncan *et al.* for $Pd_{0.8\ ML}$/Au(111) [13]. They assign peaks 2/2' to hydrogen adsorption/desorption on steps and their disappearance would be related to the coalescence of Pd islands with cycling, which would reduce the number of steps.

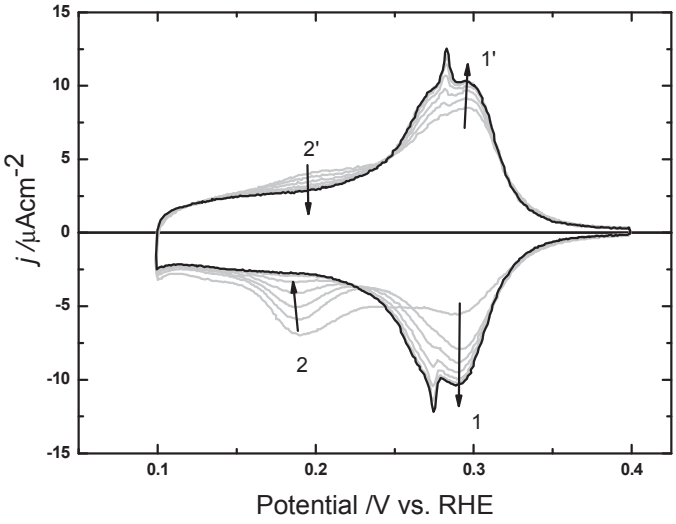

Figure II.13: Voltammogram of $Pd_{1\ ML}$/Au (111) in 0.1 M H_2SO_4 solution. Scan rate: 5 mV·s^{-1}.

In the following discussion, we will always show the stable curve, except when specially indicated.

We note that the amplitude of the curve's change is smaller for thicknesses higher than 1 ML: the steady-state is obtained in less than 5 cycles.

Our experiments also show that the quality of substrate is decisive for the stability of Pd films. For Pd adlayer formed on high quality Au(111) surface, the stable state is quickly reached (Figure II.14). Hence flame annealing is a key step in the gold surface preparation in order to remove the surface defects before Pd deposition.

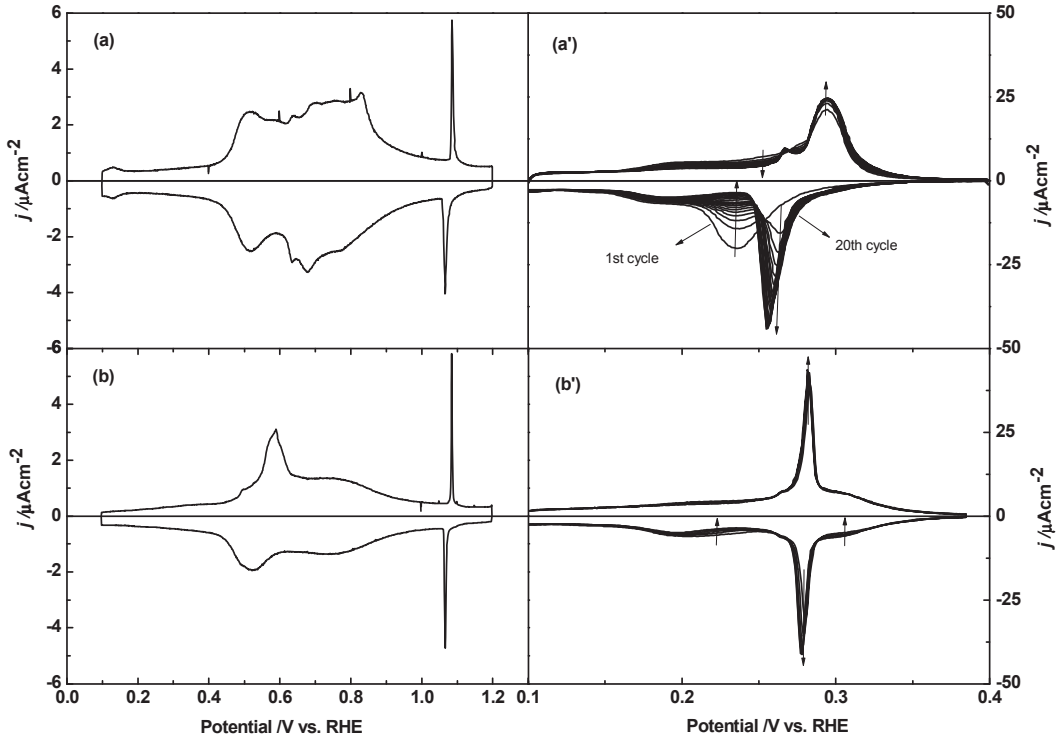

Figure II.14: Flame annealing influence on the quality of the gold substrate and on the deposited film. Electrochemical characterizations of flame annealed Au(111) in 0.1 M H_2SO_4 before (a) and (b) (10 mV·s^{-1}) and after (a') and (b') Pd deposition ($Pd_{1.5\ ML}$/Au(111), 5 mV·s^{-1}).

II.3.3 Scan rate influence

As the comparison of scan rate normalized voltammetric curves shows (Figure II.15), the peaks are definitively better defined in correspondence of the lowest scan rate. Contrarily to region 3, which doesn't seem to change with scan rate, peaks 1/1' and 2/2' are no more convoluted and become reversible with the scan rate decreasing. Region 4, dominated by hydrogen insertion/desorption convoluted with hydrogen evolution reaction (HER) faradic reaction, changes a lot, as expected, with scan rate[e].

[e] Purely faradic current depends only on the over-potential and does not change with scan rate. HER current, dominating contribution in region 4, is supposed to be independent from the scan rate and, once normalized with the scan rate, it should decrease as the scan rate increases.

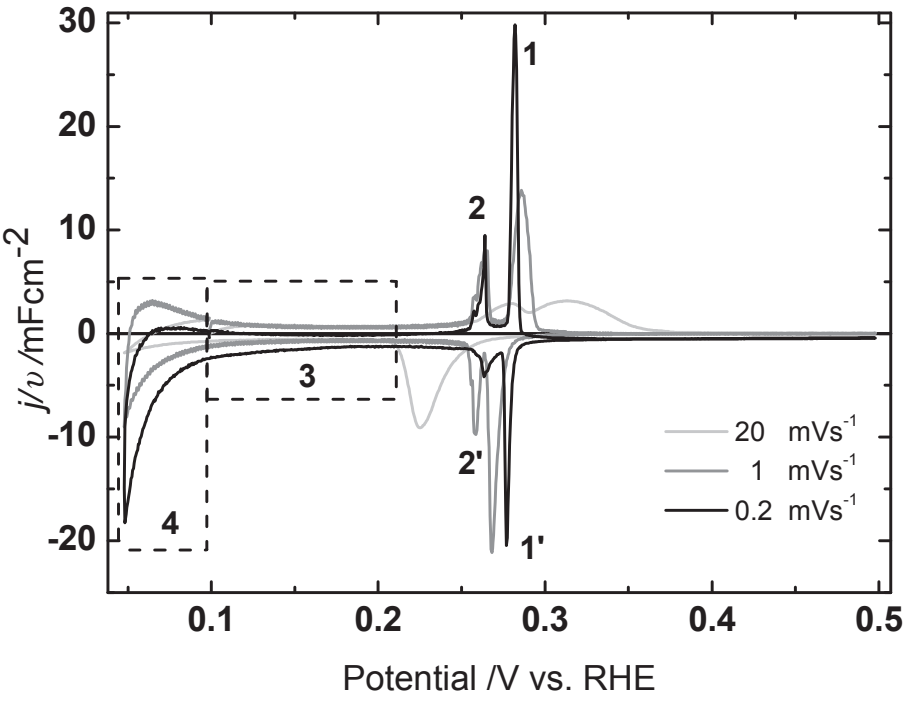

Figure II.15: Cyclic voltammograms of $Pd_{4\ ML}$/Au(111) in 0.1 H_2SO_4 at different scan rates.

Nevertheless big differences between the non normalized current with different scan rate are still present, indication that HER current is not the only contribution to the total current in this potential region.

Finally, a quite low speed rate for Pd/Au(111) film electrochemical characterization must be used, much lower than 10 $mV \cdot s^{-1}$ used for Pd/Pt(111) [1]. As figure II.15 shows, the peaks are already well defined at 1 $mV \cdot s^{-1}$, hence we decided not to work at lower scan rate, because the small improvements on the peaks resolution would be rapidly counteracted by the contamination during such long experiments. So we set the scan rate equal to 1 $mV \cdot s^{-1}$ in all the electrochemical characterization experiments.

In conclusion, we could determine the parameters best choice for Pd/Au(111) film characterization in 0.1 M H_2SO_4, the voltamperometry informing about the Pd film surface morphology. A reasonable potential range is found to be 0.1 V - 0.5 V *vs.* RHE, where ions adsorption occurs. Pd film is oxidized and dissolution begins at potential higher than 0.8 V *vs.* RHE. Even if cathodic sweeping down to 0.1 V *vs.* RHE may be

helpful to remove contaminating anions, potential must be kept in the range 0.5 V - 0.8 V *vs.* RHE in order to avoid film's degradation caused by hydrogen absorption/desorption cycles.

The stability of CV curve seems to be directly related to the quality of Au(111) surface. The voltammogram more rapidly stabilizes for Pd film deposited on defects poor Au(111) surface.

A sweep rate as low as at least 1 $mV \cdot s^{-1}$ is necessary to separate the different reaction steps.

II.3.4 **Peaks description and evolution**

In this section, we will try to assign the various peaks present in the electrochemical characterization of Pd/Au(111) films, in order to get information about the surface morphology of the samples. The results will be discussed qualitatively first, then quantitatively.

Figure II.16 shows the typical voltammogram obtained for $Pd_{4\ ML}$/Au(111) in 0.1 M H_2SO_4 For convenient discussion, this figure has been divided into different zones following their noticeable features. Accordingly to Baldauf *et al.* [11], region III corresponds to hydrogen absorption into Pd and the beginning of hydrogen evolution reaction. The authors show that HER proceeds at higher over-potentials as compared to massive palladium and becomes more pronounced with increasing film thickness.

Region II is relatively flat and featureless. Nevertheless, the current is much larger than the one associated with double layer charging and it has been ascribed to hydrogen adsorption [11,13,14].

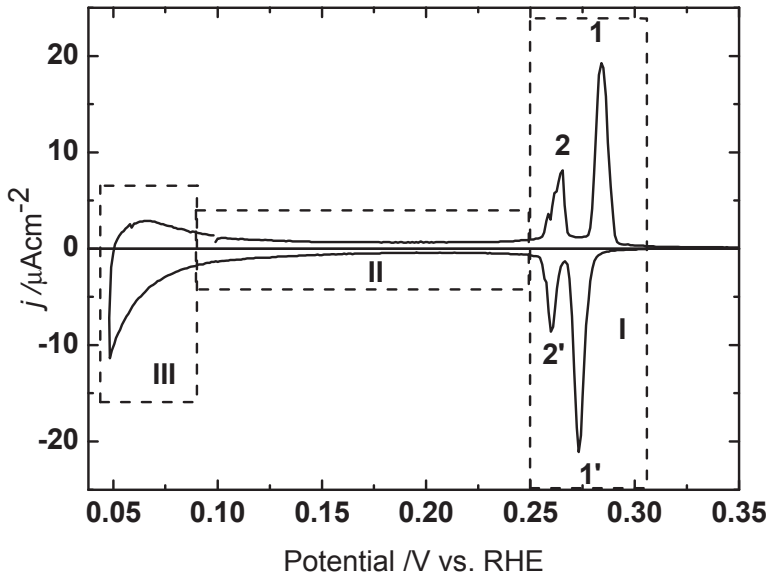

Figure II.16: Voltammogram of $Pd_{4\ ML}$/Au(111) in 0.1 M H_2SO_4. Sweep rate: 1 mV·s^{-1}.

The two cathodic peaks 1' and 2' have tentatively been attributed by Baldauf *et al.* [11] to hydrogen adsorption on the perimeter of Pd islands formed on the first Pd layer (1') and to hydrogen adsorption on terraces (2'). Peaks 1 and 2 are supposed to be the corresponding anodic peaks during reverse scan, thought they are not well separated in their experiments.

Duncan *et al.* [13] associated peaks 2/2' to the 3D growth of Pd, supporting this hypothesis on the work of Kibler *et al.* [8], who observed with *situ* STM images the formation of the third layer of Pd before the completion of the second one. They also refer to the fact that peaks 2/2' seems to appear at the same time with hydrogen absorption, as shown by the increase of the current at low potentials (no hydrogen absorption is found in electrochemical experiments for one Pd layer [11,15,16,17,18]).

Indeed, precise attribution of H adsorption peaks remains controversial.

In order to check the correspondence between cathodic and anodic peaks, we used the so called potential window technique, as shown in Figure II.17 for $Pd_{2\ ML}$/Au(111).

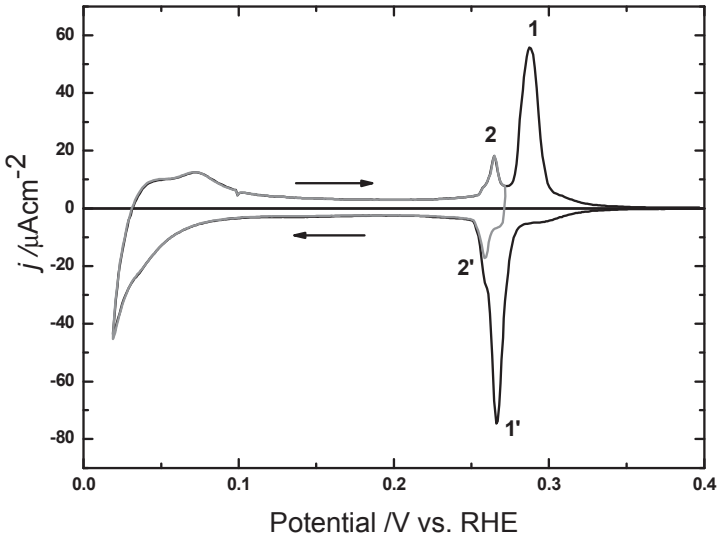

Figure II.17: Voltammograms of $Pd_{2\ ML}$/Au(111) in 0.1 H_2SO_4 with different potential ranges. Sweep rate: 5 $mV \cdot s^{-1}$.

By setting the switch potential between peaks 2 and 1, we not only show that peak 2' corresponds to peak 2, but also that the single reduction peak observed at high scan rate is actually the superposition of two peaks, 1' and 2'. Hence two different processes are present in hydrogen adsorption reaction.

Effects of thickness

Figure II.18 shows the characterization curves measured for Pd films with several thicknesses.

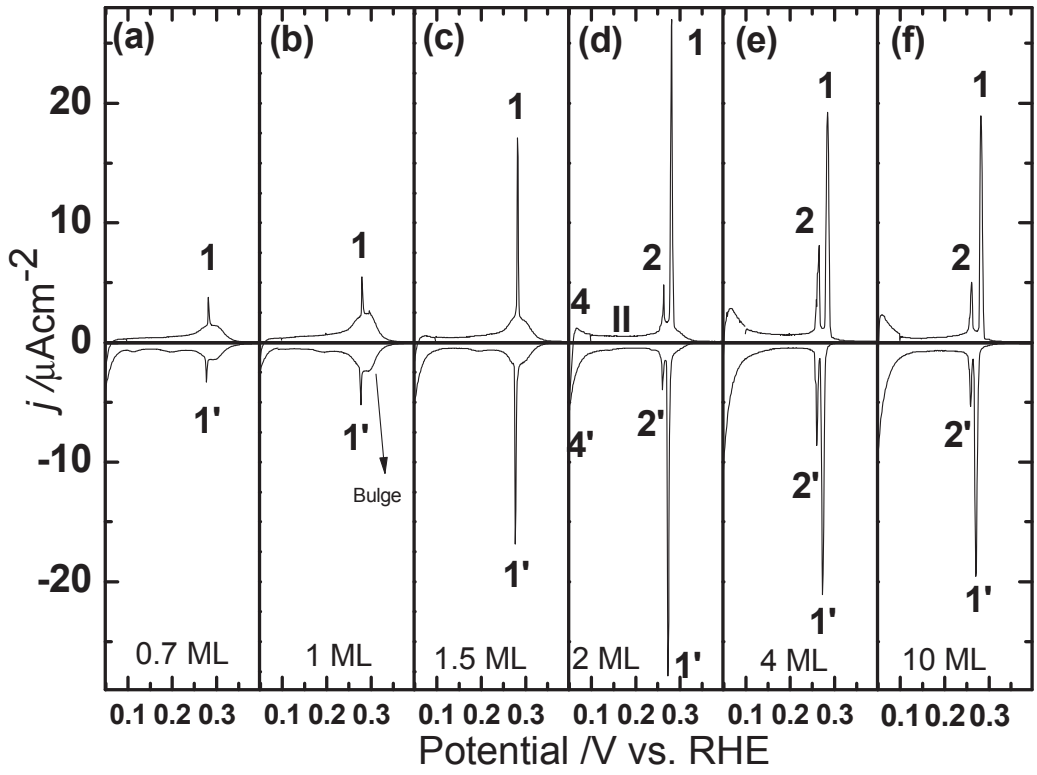

Figure II.18: Voltammogram of $Pd_{x\ ML}$/Au(111) in 0.1 M H_2SO_4, sweep rate: 1 mV·s^{-1}.

We can see well defined signatures which evolve as a function of the thickness. The main changes are the appearance of peaks 2/2' at 2 ML, the amplitude evolution of peaks 1/1' and the disappearance of the broad bump (called bulge in the following) under peaks 1/1' at the highest thicknesses. More in details:

Region II: the effects of thickness are very small (Figure II.19). Peaks 1/1' (Figure II.20). They are very small and narrow up to 1 Pd ML. Then they grow significantly from 1 ML to 1.5 ML and their height almost doubles at 2 ML. They reach the maximum intensity for 2 ML and slightly decrease for 4 ML and 10 ML. They also become broader beyond 2 ML.

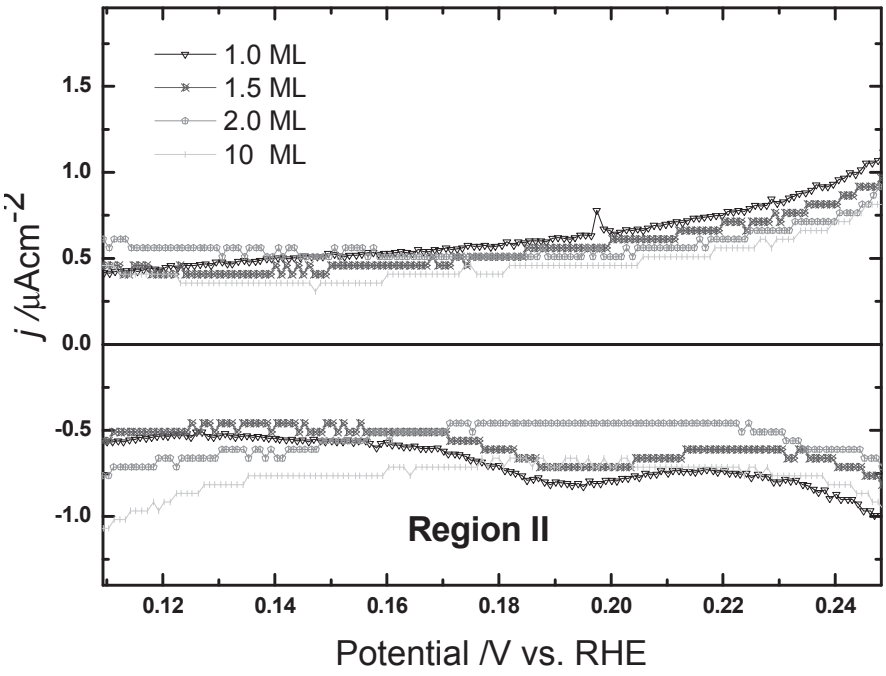

Figure II.19: Voltammograms of $Pd_{x\ ML}$/Au(111) in 0.1 M H_2SO_4. Same data as Figure II.18, enlarged scale. Sweep rate: 1 mV·s^{-1}.

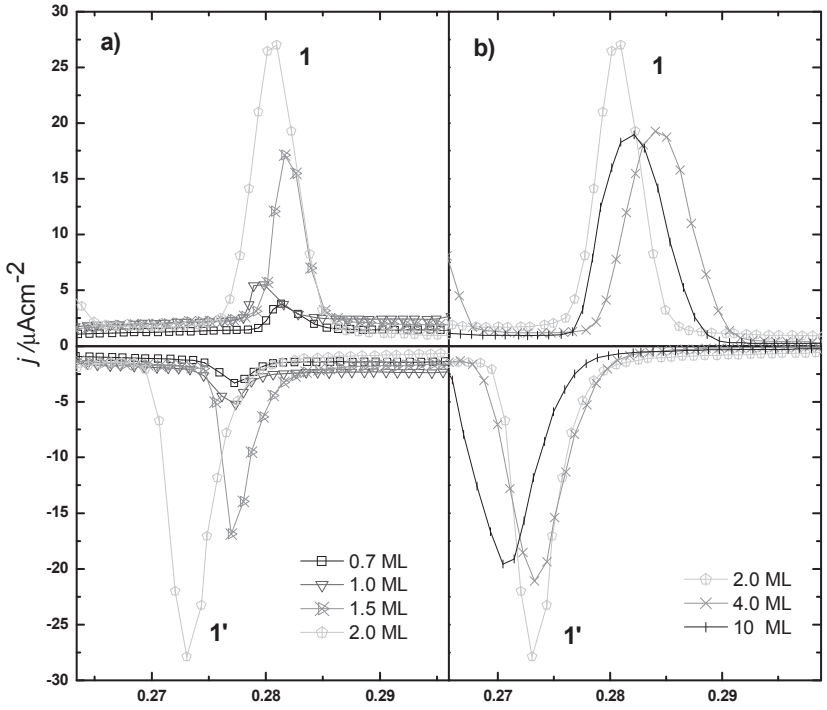

Figure II.20: Voltammograms of $Pd_{x\ ML}$/Au(111) in 0.1 M H_2SO_4. Same data as Figure II.18, enlarged scale. Sweep rate: 1 mV·s^{-1}.

Peaks 2/2' (Figure II.21): they are present only for thicknesses of at least 2 monolayers. They become broader with thickness and the maximum intensity is for about 4 ML, even if their amplitude does not change as dramatically as it is the case for peaks 1/1'.

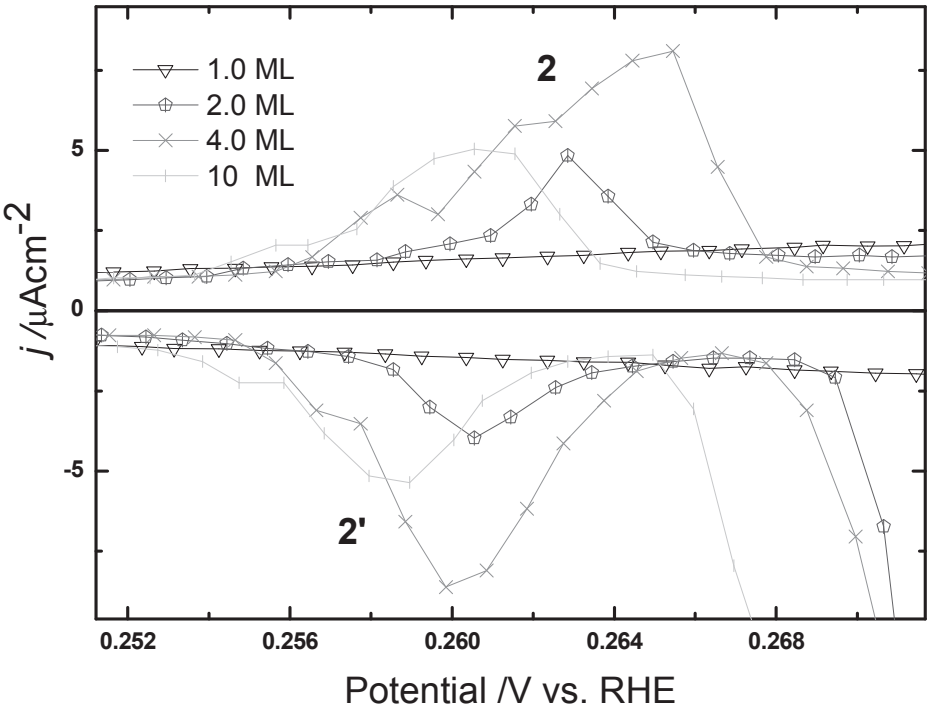

Figure II.21: Voltammograms of $Pd_{x\ ML}$/Au(111) in 0.1 M H_2SO_4. Same data as Figure II.18, enlarged scale. Sweep rate: 1 $mV \cdot s^{-1}$.

We point out for the first time the presence of a bulge under peaks 1/1' for the lower coverage (Figure II.22). It is already present at 0.7 ML and reaches its maximum amplitude at 1 ML. Then it rapidly decreases with thickness and is no more present at 4 ML.

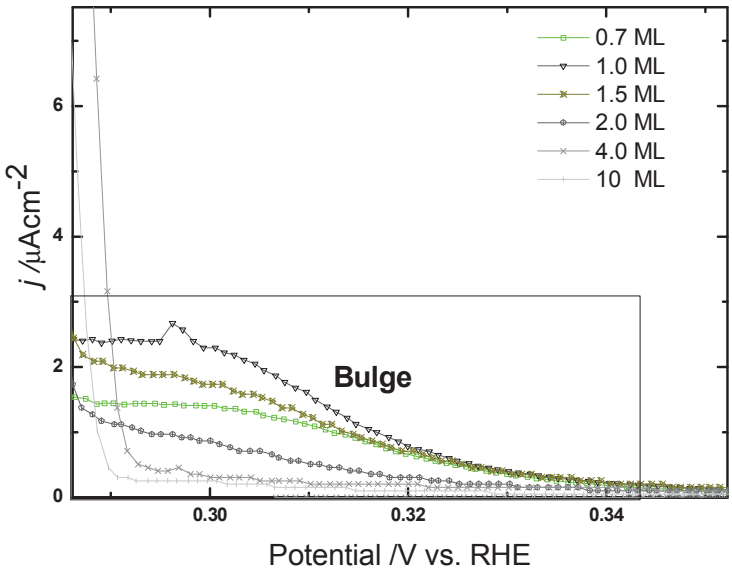

Figure II.22: Voltammogram of $Pd_{x\ ML}$/Au(111) in 0.1 M H_2SO_4. Same data as Figure II.18, enlarged scale. Sweep rate: 1 $mV \cdot s^{-1}$.

Peaks 4/4' (Figure II.23): intensity increases with thickness, even if not in a regular way.

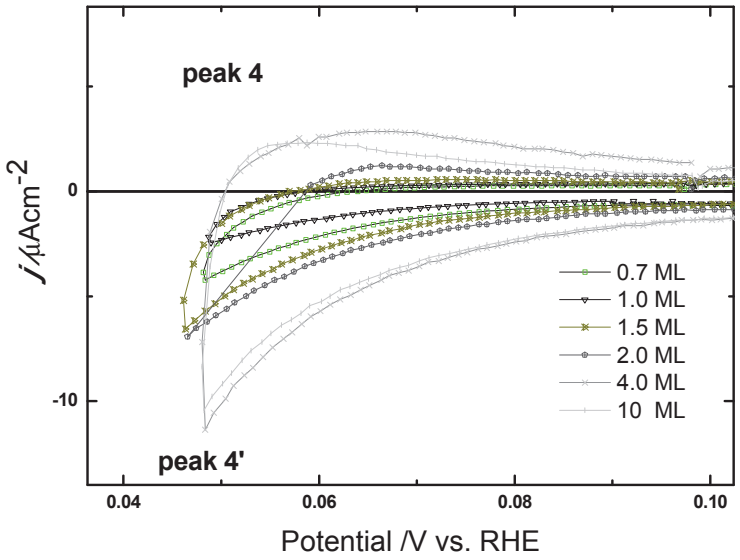

Figure II.23: Voltammograms of $Pd_{x\ ML}$/Au(111) in 0.1 M H_2SO_4. Same data as Figure II.18, enlarged scale. Sweep rate: 1 $mV \cdot s^{-1}$.

II.3.5 Relationship between peaks and electrochemical reactions

As shown in the previous paragraphs, the assignment of electrochemical reactions to each peak is still controversial. By qualitative comparison and quantitative analysis, we have tried to get a deeper understanding of the different processes occurring at the surface as a function of the applied potential.

As a first step, we made a comparison with Pt(111) [19]. As gold, platinum is a noble metal with hexagonal (111) surface.

Figure II.24 shows a comparison of voltammograms recorded for Pt(111) and $Pd_{1\ ML}$/Au(111) in sulfate solution.

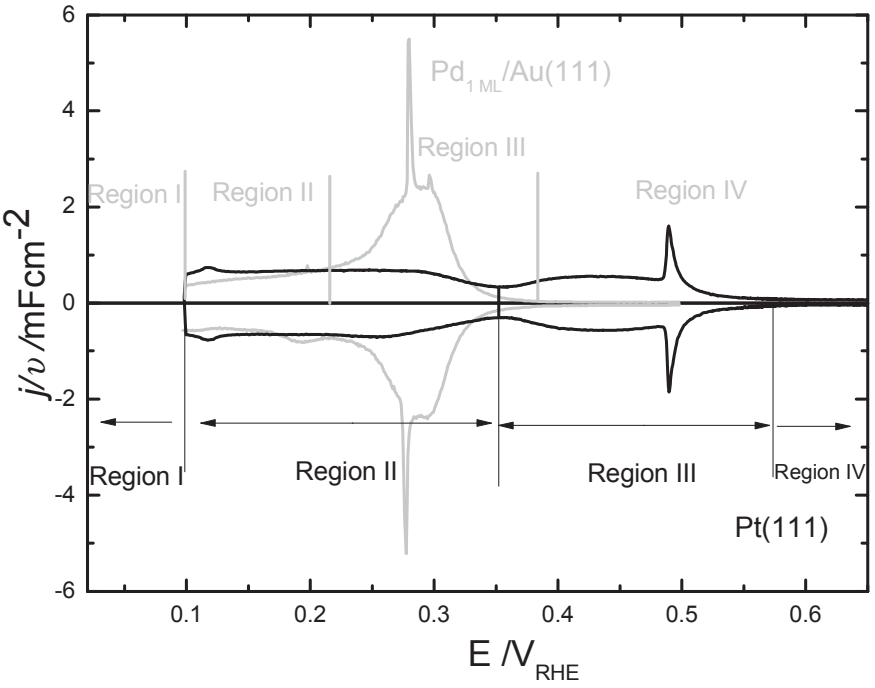

Figure II.24: $Pd_{1\ ML}$/Au(111) (light grey line) and Pt (111) [19] voltammograms, 0.1 M H_2SO_4.

The Pt(111) curve, whose shape reminds a “butterfly”, can be divided in four regions:

Region I: Hydrogen evolution region. No absorption is expected on Pt(111).

Region II: The hydrogen adsorption/desorption region. It is relatively flat and featureless. Some authors [20,21,22] modeled the hydrogen UPD isotherm with a simple Frumkin adsorption [23], which considers the interaction between hydrogen adsorbed atoms. The associated charge corresponds to about 2 adsorbed hydrogen atoms per 3 Pt surface atoms.

Region III: It is characterized by two distinct features, a broad peak and a spike. The total charge corresponds to one electron per 3 Pt surface atoms. Compared to the bulge, the charge under the spike is negligible. Combining classical electrochemistry with *in situ* STM/XRD, the ordered/disordered phase transition of the sulfate adlayer has been proved to be the origin of the spike in the Pt(111) voltammogram [24]. The same authors applied Mont Carlo computational algorithms and succeeded in reproducing the various features in the whole butterfly region assuming a hard interaction between hydrogen and adsorbed sulfate. They ascribe the cathodic pre-wave near the spike to long-range ordered adsorption of sulfate.

Region IV: Double layer region. Current is associated to the double layer charging/discharging.

For completeness, we also cite the refined model proposed by Blum *et al.* [25], where proton, water and bisulfate form honeycomb structure.

Accordingly to the shape similarities between the voltammograms of the two systems, as shown in figure II.24, we will try to consider for Pd/Au(111) the same mechanisms as those described in previous paragraphs for Pd/Pt(111).

Region II

Region II is as flat and featureless as for Pt(111). Its shape is not sensitive to the different scan rates, indicating a high kinetic of the associated reaction, and doesn't vary significantly with thickness. We assign this zone to hydrogen adsorption/desorption, following a Frumkin isotherm where the interaction between adsorbed ions is repulsive.

From Figure II.25, we can see that region II is present for the three electrodes, Pt(111), $Pd_{1\ ML}$/Au(111) and $Pd_{1\ ML}$/Pt(111). Nevertheless, the width is smaller for the Pd films, especially in the case of Pt(111) as a substrate. These differences may be just caused by the displacement of region III down to lower potentials, but we can't exclude that a fraction of hydrogen adsorption/desorption extends in region III, as a background signal under the peaks.

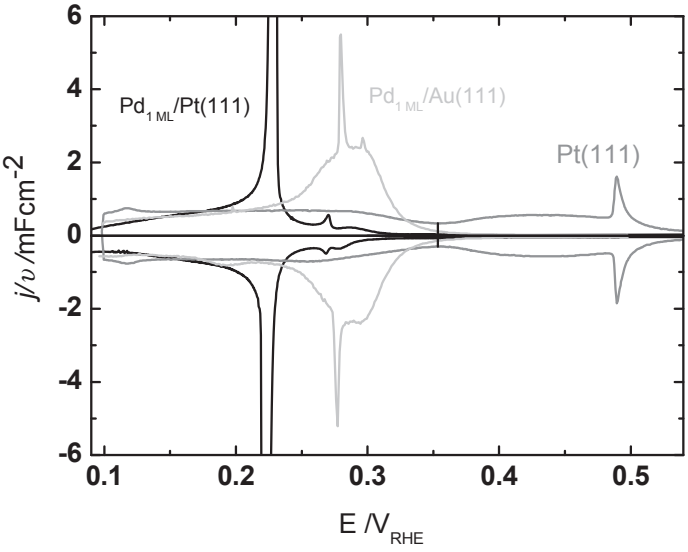

Figure II.25: $Pd_{1\ ML}$/Au(111) (light grey line), $Pd_{1\ ML}$/Pt (111) [1] (black line) and Pt(111) [19] (dark grey line) voltammograms in 0.1 M H_2SO_4.

Region III is described by a bulge and by a thin peak in both Pt(111) and Pd/Au(111) systems. As a first approximation, we are tempted to attribute region III to the adsorption/desorption and reorganization of (bi)sulfate. Nevertheless, a more detailed

analysis allows going deeper into the comprehension of the reactions present in this potential range.

Region III: the bulge

As shown in Figure II.24, the charge under the bulge is larger than for Pt(111). It reaches his maximum value for 1 ML (see Figure II.22), and decreases both for thicker but also for thinner deposits. It behaves like it were associated to ions (hydrogen and/or (bi)sulfate) adsorption/desorption on the free surface of the first Pd atomic layer deposited on Au(111). We also remark that the bulge decreases, but doesn't disappear, for a deposit of 2 ML as equivalent thickness. According to our model, this would correspond to the presence of a fraction of the 1st layer surface free on the surface. This description is in fully agreement with previous STM observations [8], indicating that indeed the 3rd layer growth begins before the completion of the 2nd layer.

Region III: peaks 1/1'

Peaks 1/1' are small and very sharp at low coverage, up to $Pd_{1\ ML}$/Au(111). Then, they increase mostly in height but also slightly in width up to $Pd_{2\ ML}$/Au(111) (Figure II.20a). For thicker deposit, their height is gradually decreasing (Figure II.20b). As it is the case for the spike in Pt(111), a first attempt would be to associate them to the (bi)sulfate adlayer reorganization. Nevertheless, the anodic peak is not at higher potential than the bulge as it is the case for Pt(111) and hence it cannot be assigned to an adsorbed sulfate phase transition at a specific potential, as (bi)sulfate layer must be adsorbed on the surface before being reorganized. Moreover, the charge under the 1/1' peaks is much larger (~48 $\mu C \cdot cm^{-2}$) for $Pd_{1.5\ ML}$/Au(111) than for Pt(111) (~14 $\mu C \cdot cm^{-2}$), confirming that the underlying reactions are not same in the two systems (Figure II.26). Indeed, the various observations just commented induce to ascribe these peaks to both adsorption/desorption and reorganization, or more simply to the direct adsorption/desorption of an organized structure, explaining the sharpness of the peaks.

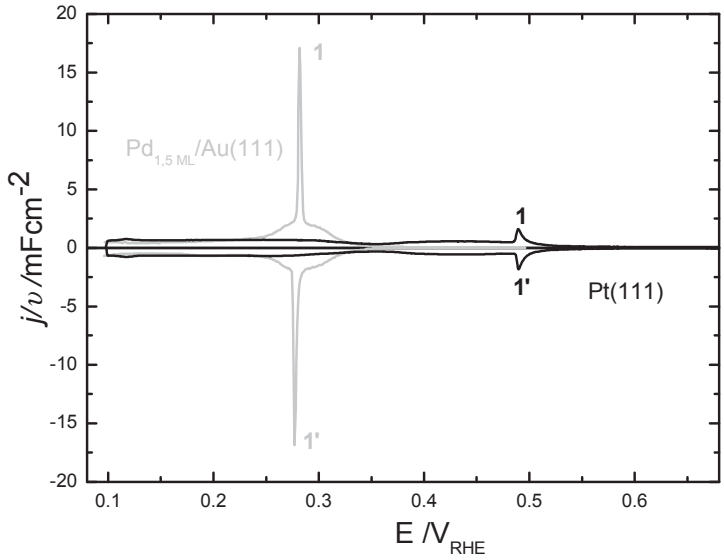

Figure II.26: $Pd_{1.5\ ML}$/Au(111) (light grey line) and Pt(111) (black line) voltammograms in 0.1 M H_2SO_4.

As peaks 1/1' reach their maximum for $Pd_{2\ ML}$/Au(111), a first approximation is to assign them to reactions on the free surface of the 2nd Pd layer. However, this in in contradiction with the fact that peaks 1/1' are present for 0.7 and 1.0 ML, thicknesses for which there is no second Pd layer deposit. At the same time, we already noticed (Figure II.20) that the behavior of these peaks markedly changes once the second layer deposition begins. These findings can be explained with the presence of two contributions in the same potential interval, i.e. under the peaks 1/1': anions adsorption on the 2nd Pd layer for x>1 and possibly the reconstruction of the fraction of adsorbed layer on the first Pd layer or the adsorption of a well-organized structure.

Such a description for the reactions contributing to peaks 1/1' suggests that the proportion of the free 2nd Pd layer on the surface doesn't significantly change from 2 ML up to 10 ML, as the peaks intensity does not vary in this thicknesses range. Indeed, preliminary results from surface X-ray diffraction experiments [26] made at the ESRF by ESME team point out the presence of 3D growth for higher coverage than two layers, characterized by the presence of towers about 20 ML high for Pd_{4ML}/Au(111) above the

two complete Pd adlayers and covering only about 10% of the surface (see Figure II.27). Data analysis reveals that only the height of the towers increases with thickness up to 10 ML, while the fraction of free second layer surface does not significantly evolve. I*n situ* STM images on Pd deposition without chloride [8] show a strong 3D growth beyond two layers as well, with huge deposits at stepped sites. Hence, the structural description of thicker films than 2 ML consists in an extremely rough surface, with growth of high towers leaving large parts of the 2nd Pd layer free at least up to 10 ML. This model is in complete agreement with the assignment of peaks 1/1' to hydrogen adsorption/desorption on the second pseudomorphic Pd layer, its behavior exactly corresponding to a 3D "towers like" growth.

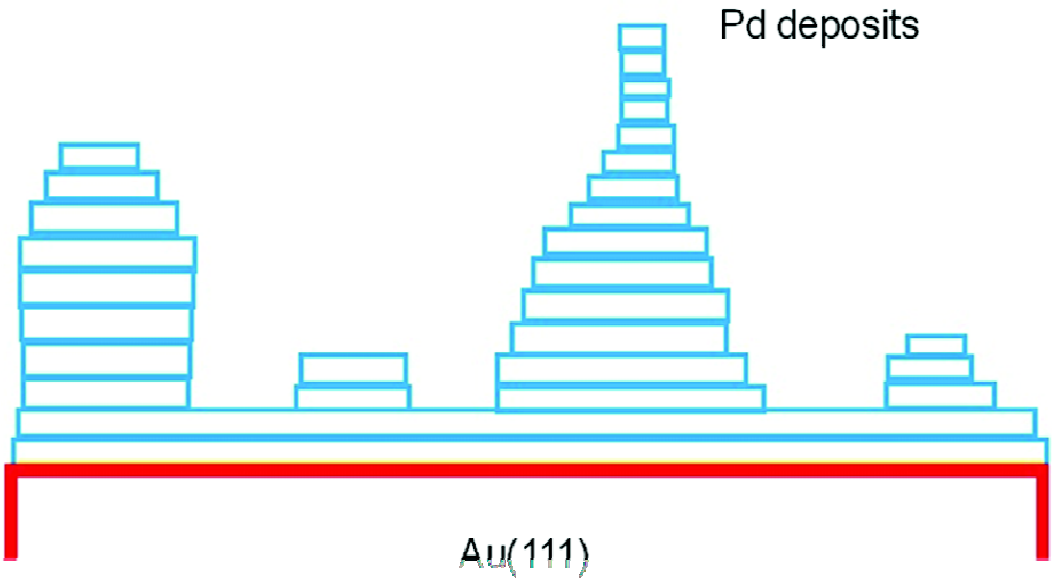

Figure II.27: Schematic of the $Pd_{4\ ML}$/Pt(111) film structure according to SXRD measurements[26].

Region III: peaks 2/2'

Peaks 2/2' are sharp and the integrated charge value is larger than for the spike characterizing Pt(111) (Figure II.28).

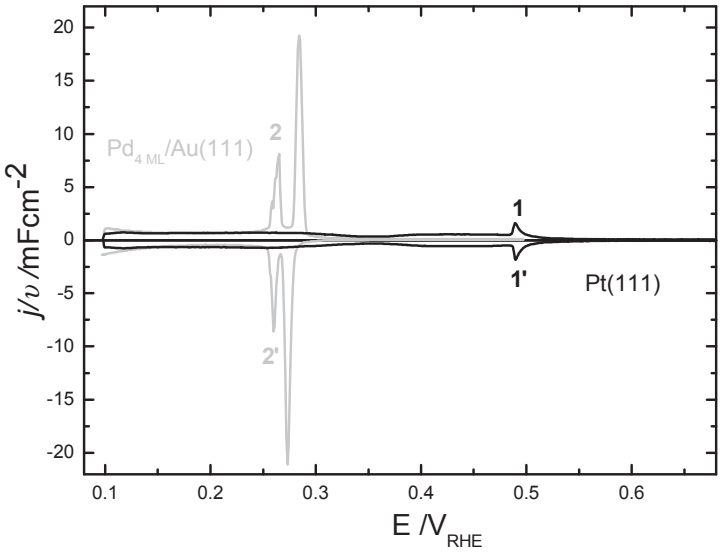

Figure II.28: $Pd_{4\ ML}$/Au(111) (light grey line) and the Pt(111) (black line) [19] voltammograms in 0.1 M H_2SO_4.

They appear only at 2 ML, reach the maximum intensity at 4 ML, and slightly decrease at 10 ML. Keeping in mind the structural model for Pd/Au(111) films described in the previous paragraph, peaks 2/2' seem to be associated to hydrogen adsorption on relaxed Pd layers. The overall small size of 2/2' peaks would be due to the rather small towers footprint and the slight intensity decrease beyond 4 ML would be linked to the shrinkage of the towers size with thickness increasing.

We note that potential position of peaks 2/2' is very close to the electrochemical signature of hydrogen adsorption on 2nd and following pseudomorphic Pd layers on Pt(111) [27] (see Figure II.29).

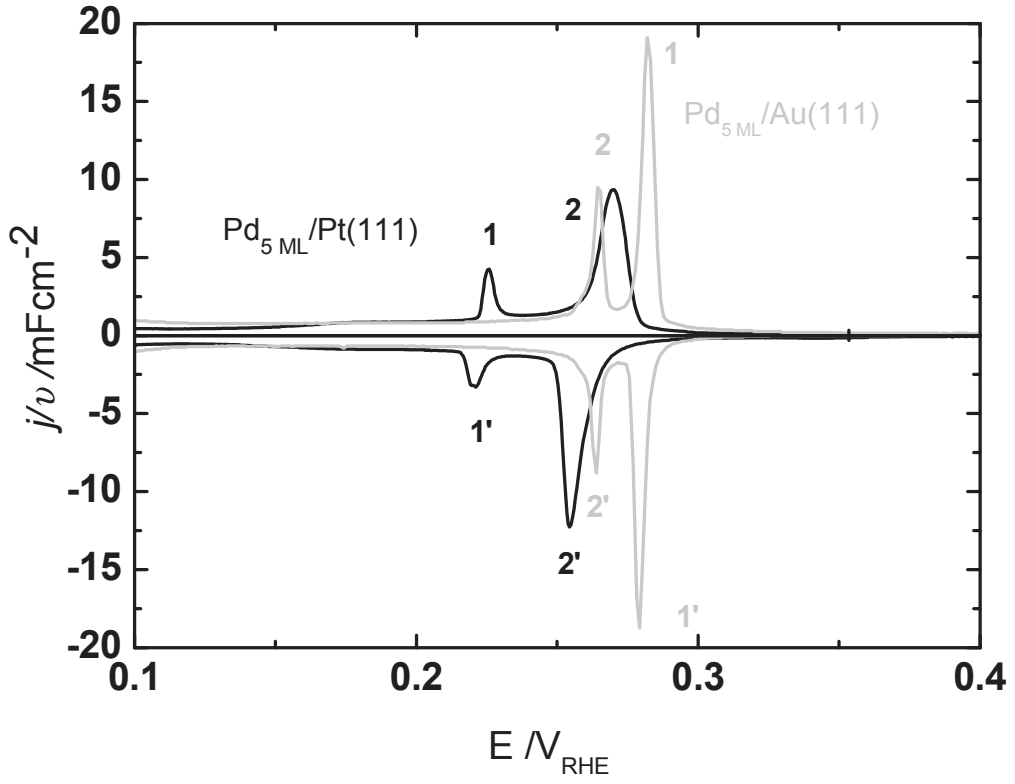

Figure II.29: CV for the $Pd_{5\ ML}$/Au(111) (light grey line), $Pd_{5\ ML}$/Pt(111) (black line) [1] in 0.1 M H_2SO_4.

Such a correspondence suggests a similarity for both the electronic and the geometric structure of the Pd surface layers deposited on the two substrates. This is not astonishing concerning the electronic structure, as in both cases the peaks concern processes on Pd atoms adsorbed on sub-lying Pd layers. For the geometrical aspect, it would correspond to non-completely relaxed surface Pd layers on Au(111) beyond 2 ML, characterized by the same lattice parameter as the pseudomorphic Pd layers on Pt(111)[f]. Indeed, Moiré patterns have been observed by STM [8], corresponding to the loss of the pseudomorphic structure starting at the 5th layer and the surface X-ray diffraction study on the Pd films growth (see chapter III) demonstrate that the relaxation starts with the 3rd layer. Even

[f] a_{Au}=4.0782 Å, a_{Pd}=3.89°7 Å, a_{Pt}=3.9242 Å

more interesting is the Pd film structure determination obtained by ESME team [26], which shows that Pd layers beyond the second layer in $Pd_{4\ ML}$/Au(111) are not completely relaxed, with an in-plane parameter corresponding to the Pt one. All these results are in very good agreement with the proposed assignment of the 2/2' peaks.

In conclusion, we could divide the characterization curves into four potential regions, each one being associated to specific reactions. Region I involves hydrogen absorption and evolution reactions. Region II is associated with hydrogen adsorption/desorption described by Frumkin isotherm. Region III corresponds to hydrogen and/or (bi)sulfate adsorption. Region VI only exhibits double layer charging. We propose an assignment for the features present in region III. Two contributions seem to be present for peaks 1/1', one possibly corresponding to the adsorption/desorption of an organized structure for deposits below 1 ML and one due to anions (hydrogen-(bi)sulfate) adsorption/desorption onto the second pseudomorphic Pd layer. The presence of a bulge under peaks 1/1' has been for the first time pointed out, thanks to low scan rate, and assigned to anions adsorption/desorption on the first pseudomorphic adsorbed Pd layer. Peaks 2/2' are the signature of anions adsorption/desorption on the following (x>2 ML) non-completely relaxed Pd layers. This determination is in full agreement with the structural characterization for Pd/Au(111) thin films.

II.3.6 **Anions effects**

In order to further investigate the role of sulfate in the features observed during the electrochemical characterization of Pd films, we performed experiments with anion substitution. Figure II.30 shows the characterization of Pd deposits in $HClO_4$ solution and in a sulfate acid solution in presence of HCl, perchlorate being less strongly adsorbed and chloride being much more strongly adsorbed than (bi)sulfate on noble metals.

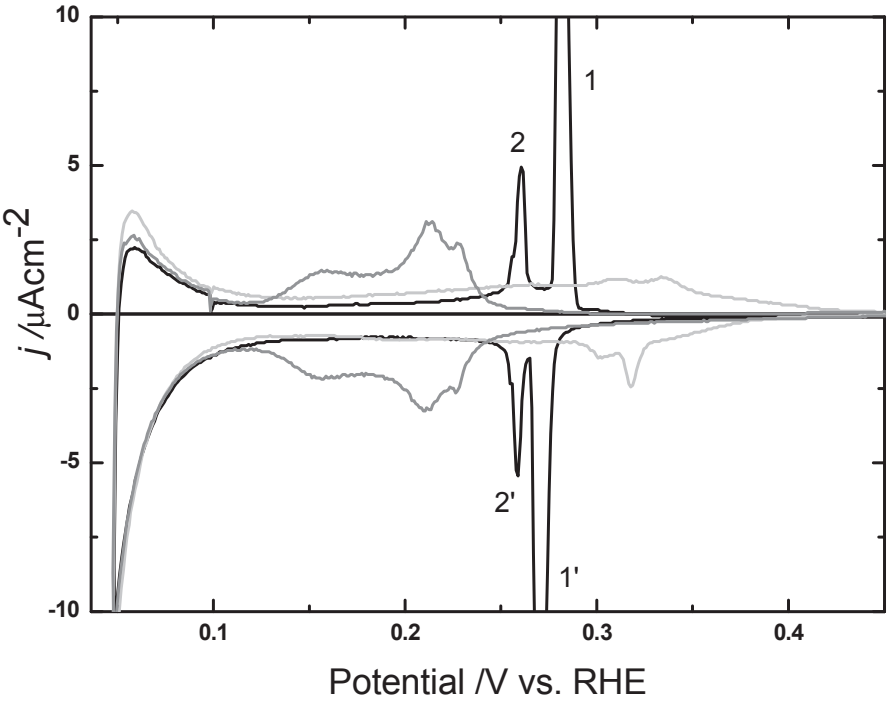

Figure II.30: $Pd_{10\ ML}$/Au(111) voltammograms in different solutions. Black line: 0.1 M H_2SO_4; grey line: 0.1 M $HClO_4$; light grey line: 0.1 M H_2SO_4+ 1 mM HCl. Sweep rate: 1 $mV \cdot s^{-1}$.

As a result, 1/1' and 2/2' peaks disappear in both substitutions and remaining features are smaller and broader. They are shifted towards higher potential in the ClO_4^- solution, while, in opposite, they are shifted down to lower potential with the addition of Cl^-. The correlation between potential shift and the strength of anions adsorption confirms that peaks in region III are specific to (bi)sulfate adsorption. From a practical point of view, this shows that the characterization of the Pd deposits in H_2SO_4 solutions gives better defined signatures.

Figure II.31 shows substitution experiments on $Pd_{1\ ML}$/Au(111), characterized by the bulge contribution under peaks 1/1' in 0.1 M H_2SO_4 attributed to hydrogen/(bi)sulfate adsorption/desorption on the first adsorbed Pd layer.

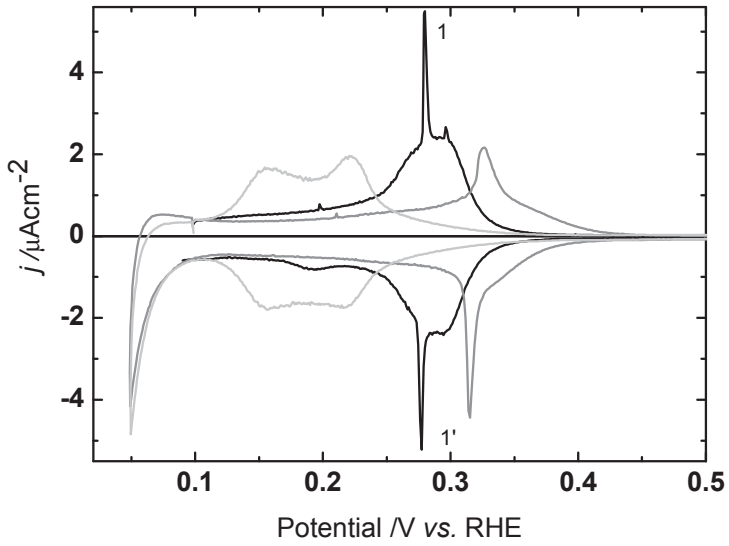

Figure II.31: $Pd_{1\ ML}$/Au(111) voltammograms in different solutions. Black line: 0.1 M H_2SO_4; grey line: 0.1 M $HClO_4$; light grey line: 0.1 M H_2SO_4+ 1 mM HCl. Sweep rate: 1 mV·s^{-1}.

As for the other peaks, the bulge shifts toward higher and lower potential with perchlorate and chloride anion substitution, respectively. This shows that all the features present in region III are related to anion adsorption. The sharp peak 1/1' is also affected by substitution, completely disappearing in presence of chloride, more surprisingly remaining with ClO_4^- substitution, especially in the cathodic part. This behavior looks similar to the one observed for Pt(111) in presence of perchlorate. Similarly, the bulge may be associated to OH adsorption in ClO_4^- [28].

It is also interesting to note that ClO_4^- substitution leads to a slightly more flat area in the region II. This would suggests that the observed slope in H_2SO_4 is partially related to a repulsive co-adsorption of H and (bi)-sulfate in the corresponding potential range (0.15-0.25 V *vs.* RHE)

II.4 Quantitative analysis

In the previous section, the evolution of each feature in the characterization voltammograms has been discussed and we have qualitatively figured out the processes which may correspond to each peak in the curve. In this section, we will determine the charges associated to the various contributions, in order to find a confirmation and better interpretation of the corresponding reactions. We will mainly focus on region III, most affected by thickness and anions substitution.

Our quantitative analysis is based on the anodic curve, as peaks tend to overlap at higher speed rates in the cathodic sweeping (Figure II.17).

II.4.1 Anodic peak 1

The charges under peaks 1 and 2 are calculated after subtraction of the bulge and anions adsorption contributions in region II.

The charge corresponding to peak 1 as a function of thickness is shown in Figure II.30. The charge is very small up to 1 ML. Then, there is a strong increase between 1 ML and 2 ML. This is coherent with peak 1 being a signature of anions adsorption on the 2^{nd} layer. From 2 ML to 10 ML, the charge is mostly unchanged, suggesting that there is no evolution of the 2^{nd} layer free surface. Within the "towers like" growth structural model beyond the 2^{nd} pseudomorphic layer, this corresponds to the fact that 3D growth starts before completion of the 2^{nd} layer, and the area covered by the rising towers is compensated by the completion of the 2^{nd} layer for x>2. The decreasing of the charge from 10 ML to 16 ML indicates that only beyond about 10 ML the second layer is going to be completed.

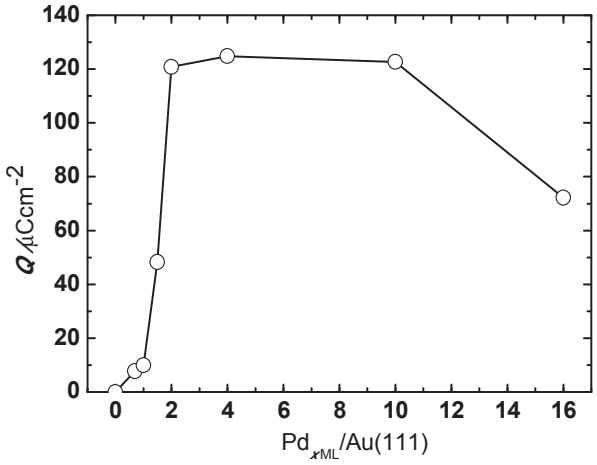

Figure II.32: The integrated charge under peak 1 as a function of thickness.

Full width at half maximum (FWHM) of peak 1 as a function of thickness (Figure II.33) shows the presence of two regions, below and above 2 ML. This observation supports our hypothesis that two superposed contributions are present in the same potential interval, under peak 1.

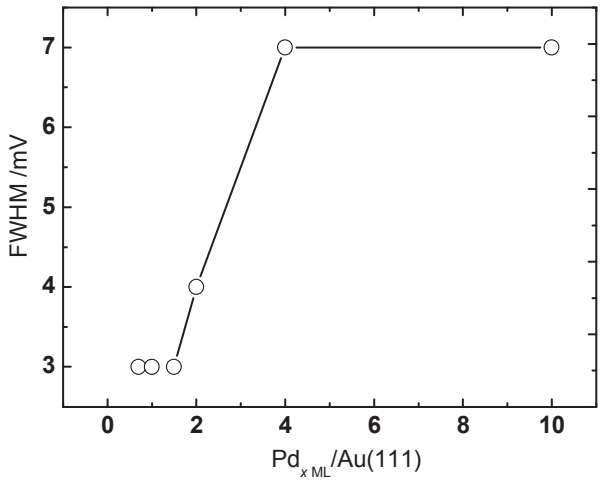

Figure II.33: FWHM of peak 1 defined in figure II.20 as a function of thickness.

The first one, with an overall marginal charge of 10 $\mu C \cdot cm^{-2}$, would correspond to a reorganization of adsorbed species on the 1st layer. The second and main one, 12 times larger, is the direct adsorption of hydrogen/(bi)sulfate on the 2nd layer.

II.4.2 **Anodic peak 2**

Figure II.34 shows the integrated charge under peak 2 as a function of the Pd film thickness.

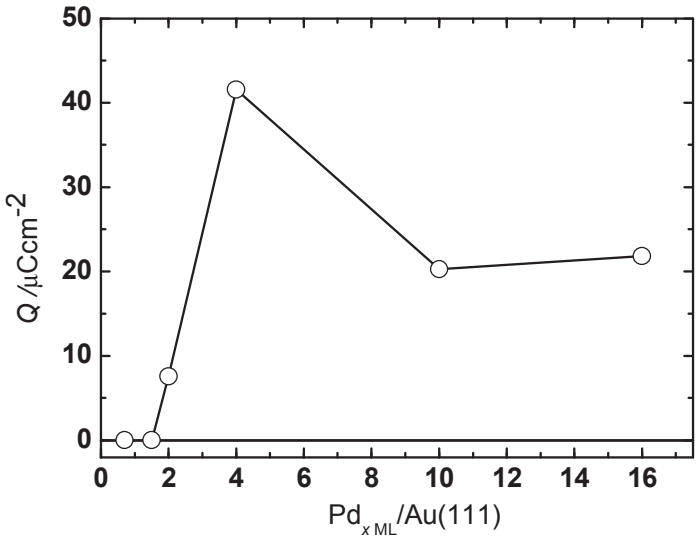

Figure II.34: The charge under peak 2 defined in Figure II.20 as a function of thickness.

It only appears for x>2 ML and is definitely smaller than the charge under peak 1. The overall behavior of the charge is in agreement with the assignment of peak 2 to the anions adsorption on relaxed Pd, in particular on top of the 3D towers. The maximum at 4 ML may be related to larger towers at the beginning of the growth. If we consider that the same type of anions are adsorbed under peaks 1 and 2, their charge ratio suggests that the top of towers occupy about 1/6 of the surface for 10 ML and 16 ML. Contrarily to previous studies on Pd deposition on Pt(111) showing that for this system charges ratio cannot be directly related to free surfaces [1,29], this result is in very good agreement with the 10% value for the occupation ratio of the 3D towers given by SXRD [26].

II.4.3 **Bulge**

(Bi)sulfate adsorption has been pointed out on Pt(111) and Au(111) surface [30], as well as on Pd/Au(111) and massive Pd(111) [31]. STM measurements of an electrodeposited Pd monolayer on Au(111) at 0.8 V *vs.* RHE show a ($\sqrt{3}\times\sqrt{7}$)R19.18° structure of adsorbed (bi)sulfate [8]. Concomitant hydrogen and (bi)sulfate adsorption has been deduced with electrochemical CO oxidation on Pd/Au(111) films [31]. At the same time, some controversy still remains if bi-sulfate or sulfate are adsorbed [32,33,34].

In this thesis the bulge feature has been pointed out for the first time and attributed to the adsorption (anodic scan) of anions on the first free Pd monolayer.

In the following discussion, we will model the bulge signal with a Langmuir isotherm which is a particular case of the Frumkin isotherm, just assuming that there is no interaction between adsorbed species [3].

For an adsorption with *n* electrons transferred, the change of Gibbs free energy is:

$$\Delta G_{ads} = nF(E - E_{eq}) \qquad \text{Equation 1}$$

where *F* is the Faraday constant, E_{eq} is the equilibrium potential.

According to Nernst equation, we have:

$$E_{eq} = E^0 + (RT/nF)\ln c_A(sol) \qquad \text{Equation 2}$$

where c_A(sol) is the bulk concentration of adsorbent in solution.

From Eq. 1 and Eq. 2 we obtain:

$$\Delta G_{ads} = nF(E - E^0) - RT\ln c_A(sol) \qquad \text{Equation 3}$$

In the case of a single adsorbate described by Langmuir isotherm, the relevant expression for the isotherm is [35]:

$$\frac{\theta_A}{1-\theta_A} = \exp(-\frac{\Delta G_{ads}}{RT}) \qquad \text{Equation 4}$$

where θ_A is the coverage of adsorbed specie A.

By substituting Eq. II.3 in eq. II.4 we have:

$$\frac{\theta_A}{1-\theta_A} = c_A(sol)\times\exp(-\frac{nF(E-E^0)}{RT}) \qquad \text{Equation 5}$$

We note that, following Eq. 5, when $E=E^0$, $\theta_A = 0.5$, ($c_A(sol)$=1).

In order to compare with voltammetric data, the potential and coverage must be expressed as a function of the measured current density i_{CV}.

From Eq. 5, E can be derived,

$$E = E^0 - \frac{RT}{nF}\ln\frac{\theta_A}{c_A(1-\theta_A)} \qquad \text{Equation 6}$$

As $i_{CV} \equiv \frac{dQ_A}{dt}$ we get:

$$i_{CV} = \frac{dQ_A}{dt} = Q\ \frac{d\theta_A}{dE}\frac{dE}{dt} = Q\,\nu\frac{d\theta_A}{dE} \qquad \text{Equation 7}$$

where Q is the charge for one full monolayer and v is the sweep rate.

From Eq. 5, we get:

$$\frac{d\theta_A}{dE} = -\frac{nF}{RT}\theta_A(1-\theta_A) \qquad \text{Equation 8}$$

And also $\theta_A = \frac{c_A(sol)}{c_A(sol) + \exp(\frac{nF}{RT}(E - E^0))}$ Equation 9

So $i_{CV} = \frac{Q\nu c_A(sol) nF \exp(-\frac{nF}{RT}(E - E^0))}{RT[1 + c_A(sol)\exp(-\frac{nF}{RT}(E - E^0))]^2}$ Equation 10

As $F = N_A e$ and $R = k_B N_A$, where N_A is Avogadro constant, e is the element charge and k_B is the Boltzmann constant, Eq. 10 can be written as following.

$$i_{CV} = \frac{Q\nu c_A(sol) ne \exp(-\frac{ne}{k_B T}(E - E^0))}{k_B T[1 + c_A(sol)\exp(-\frac{ne}{k_B T}(E - E^0))]^2} \quad \text{Equation 11}$$

Eq. 11 represents the Langmuir description for the isotherm and Figure II.35 shows the result for the fitting procedure applied on the bulge in the potential range higher than ~0.29 V *vs.* RHE. There are 3 adjustable parameters in the modeling function, the integrated charge Q, the electro-sorption valence *n* of adsorbent, and the standard potential, E^0. Fitting is adjusted taking into account for the current background value. The fit was performed only in the 0.29-0.5 V *vs.* RHE potential range, in order to avoid the contribution of peaks 1 and 2.

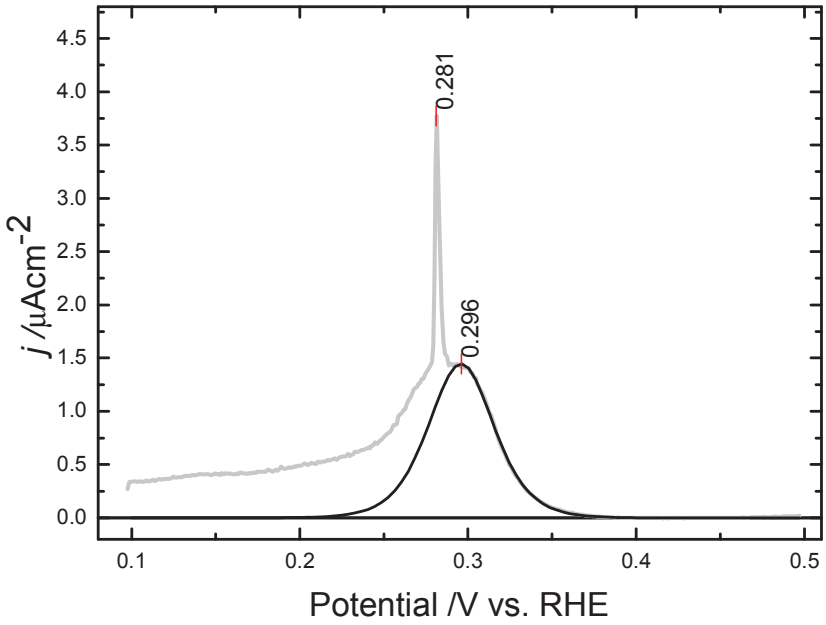

Figure II.35: $Pd_{0.7\ ML}$/Au(111) voltammogram in 0.1 H_2SO_4. Light grey line: experimental curve; black solid line: the fitting of curve using Langmuir isotherm (Eq. 11).

We can see that the Langmuir isotherm model successfully describes the experimental curve in this area. The corresponding electro-sorption valence is equal to -1.985, which is very close to -2. In the Langmuir description, it may correspond to sulfate as adsorbed species in this potential region, even if co-adsorption of one bi-sulfate and one proton can't be excluded. pH dependent experiment could be usefull to determine these adsorptions. Nevertheless, we point out that in order to determine the electro-sorption valence, other models like Frumkin isotherm should be tested, in order to verify the existence of possible lateral interaction which would certainly give different n value. E^0 is found to be equal to 0.356 V *vs.* RHE and nearly independent of the film thickness. This is in agreement with the idea that only one process is at the origin of the bulge.

Figure II.36 shows the remaining charge after subtraction of bulge and peak 1 to the Pd_{1ML}/Au(111) characterization:

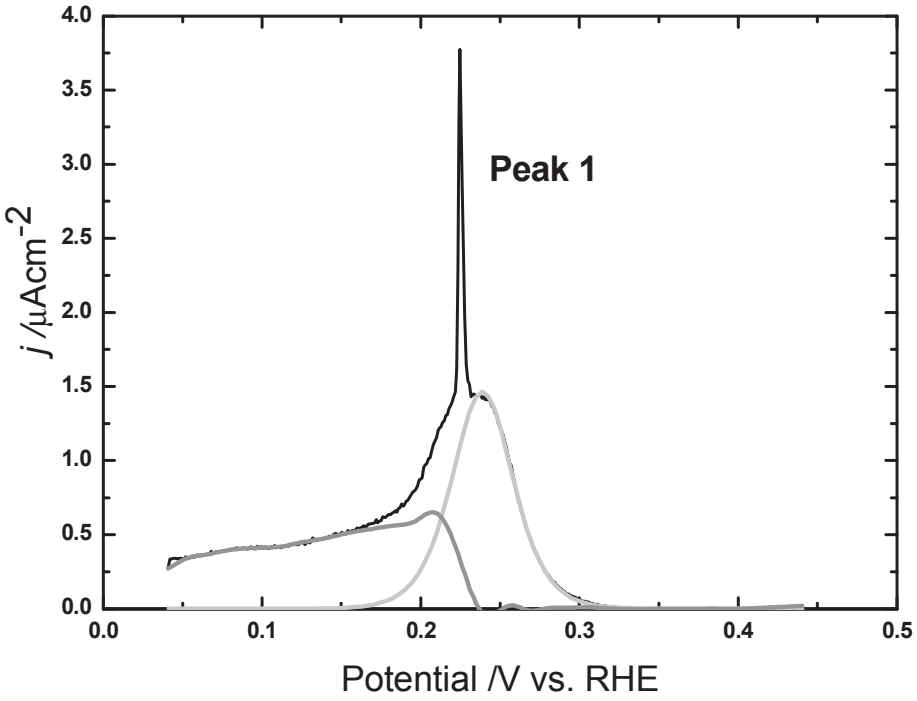

Figure II.36: $Pd_{0.7\ ML}$/Au(111) voltammogram in 0.1 H_2SO_4, 1 $mV \cdot s^{-1}$.Black line: experimental data; light grey line: fitting with Langmuir adsorption model; dark grey line: difference between the two signals.

As shown in Figure II.36 an almost flat and featureless curve is obtained by subtracting peak 1 and bulge contributions from the experimental signal. It looks like the hydrogen adsorption present in region II (described by repulsive Frumkin model) extended up to higher potential values. Indeed, looking carefully, we can see that the current at 0.2 V *vs*. RHE is about twice the current at 0.05 V *vs*. RHE. We interpret this finding as an overlap of hydrogen and sulfate adsorptions around 0.2 V *vs.* RHE. As already mentioned in the anions substitution part, a repulsive co-adsorption can modify the Frumkin isotherm, inducing the presence of a slope. It would be interesting to check this co-adsorption using CO displacement experiments for the determination of the point of zero total charge (pztc).

Concerning the charge, it is not easy to extract a trend versus the thickness. The overall charge is between 100 and 120 $\mu C \cdot cm^{-2}$.With 1 hydrogen atom adsorbed for 2 palladium

on the surface, this is significantly lower than on Pt(111) with 2 H atoms for 3 Pt atoms at the surface.

Following the Langmuir model (n=-2) we model the charge under the bulge for several film thicknesses (see Figure II.37).

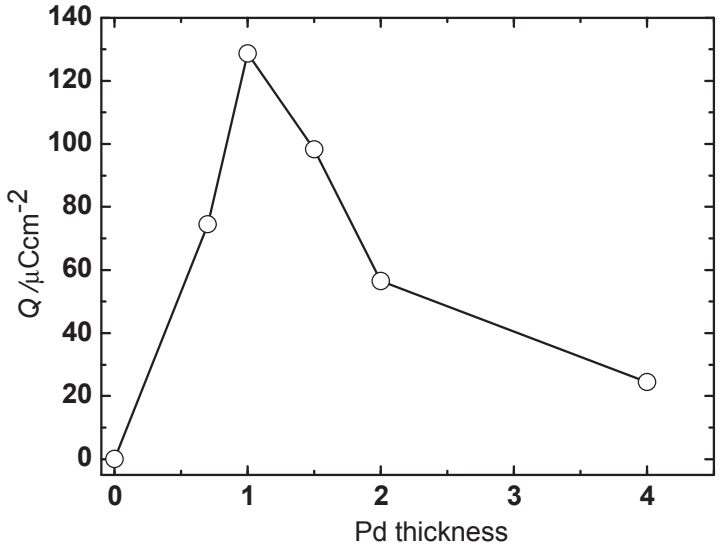

Figure II.37: The change of hydrogen/sulfate adsorption/desorption by Langmuir mode as a function of the Pd film thickness.

The charge increases from Au(111) (no Pd deposit) and reaches a maximum for 1 ML, in agreement with the assignment of this peak to the anions adsorption on the 1st monolayer free area. Our simulation shows that the charge is 57 $\mu C \cdot cm^{-2}$ for 2 ML, corresponding to about 44% of the value found for the first layer; the 1st layer doesn't seem to be fully covered (19%) even for 4 ML. These results are in agreement with a Pd growth where third layer begins before completion of the second one.

Figure II.38 shows the charges of the three features, peak 1, peak 2 and the bulge and their sum as functions of the thickness. There is a kind of exchange between the bulge and peak 1: when the first decreases, the second increases. This confirms their assignments to anion adsorption onto the free surface of the 1st and the 2nd palladium layers, respectively.

The total charge strongly increases with thickness up to 2 ML and decreases above 4 ML. As Figure II.38 shows, the main contribution to the total charge at the higher thicknesses is given by peak 1.

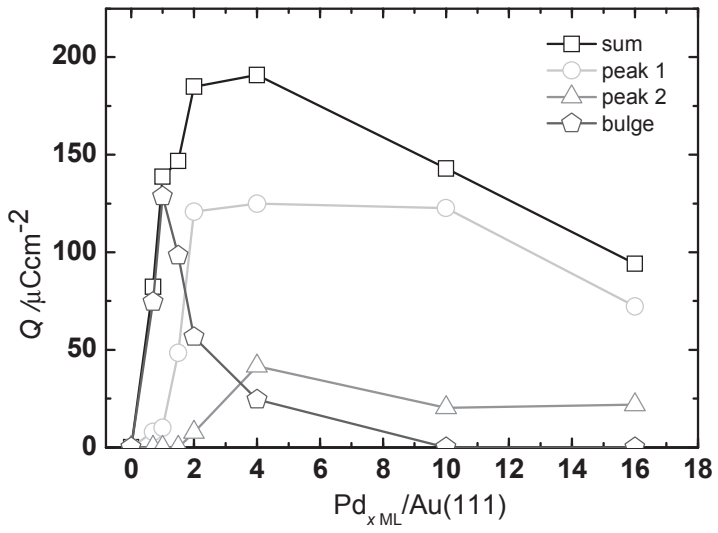

Figure II.38: The different integrated charge as functions of thickness. Open circle: charge of peak 1; open triangle: charge of peak 2; open pentagon: charge of bulge estimated with Langmuir model; open square: total charge.

In conclusion, according to the quantitative analysis, we know that: 1, towers 3D growth starts before completion of the 2nd layer, and the area covered by the rising towers is compensated by the completion of the 2nd layer. Only beyond about 10 ML the second layer begins to be completed; 2, wide peak 1 on more than 1 ML contains the contribution of both adsorbed species reorganization and adsorption; 3, bulge is corresponding to hydrogen/(bi)sulfate adsorption/desorption on free 1st Pd monolayer over Au(111) without interaction between adsorbed anion; 4, the remaining featureless part seems to be hydrogen Frumkin adsorption, where adsorbate repel each other, and can extend to 0.2 V *vs.* RHE.

II.5 Conclusions

Well-defined signatures for each deposition stage have been obtained for Pd deposition experiment. We confirmed that Pd deposition proceeds through UPD for the first monolayer and OPD for the following layers. After Pd deposition/dissolution cycle, the surface of Au(111) seems to be modified by both non-complete Pd dissolution and Au(111) surface structural evolution.

Electrochemical characterizations of the films in 0.1 H_2SO_4 show a huge effect of the scan rate, indicating that the hydrogen/sulfate adsorption/desorption reactions are kinetically controlled. Only scan rates lower than about 1 $mV \cdot s^{-1}$ allow to evidence and correctly separate the various features of the voltammetry.

Four different contributions have been observed. For the first time the hydrogen/sulfate adsorption/desorption on the 1st Pd layer is attributed to the broad bulge in the 0.2-0.3 V *vs.* RHE interval. We could successfully describe its behavior as a function of the potential and of the films thickness by a Langmuir isotherm. Peaks 1/1' has been assigned to the adsorption/desorption and reorganization reactions on the free surface of the 2nd Pd monolayer. Peak 2/2' has been attributed to the adsorption/desorption and reorganization reactions on the 3rd and following almost relaxed layers. Finally, a constant contribution (plateau) is assigned to the hydrogen adsorption/desorption described by repulsive Frumkin isotherm, whose contribution extends up to more than 0.2 V *vs.* RHE.

The evolution of the four signatures with thickness is in agreement with the fact that the growth is pseudomorphic up to the second layer, with the 3rd layer growth beginning before the completion of the 2nd layer. The attribution of the various peaks is in complete agreement with the structural model proposed by SXRD characterization of the films, where the strong 3D growth beyond the second layer is characterized by huge "towers" leaving unchanged the ratio of free second layer surface at least up to 10 ML.

Reference:

1 C. Lebouin, Y. Soldo-Olivier, E. Sibert, P. Millet, M. Maret, R. Faure, J. Electroanal. Chem., 626 (2009), 59.

2 C. C. Herrmann, G. G. Perrault, A. A. Pilla, Anal. Chem. 40 (1968), 1173.

3 O. M. Magnussen, K. Krug, A. H. Ayyad, J. S. Tettner, Electrochim. Acta, 53 (2008), 3449.

4 M. S. Zei, G. Lehmpfuhl, D. M. Kolb, Surf. Sci., 221 (1989), 23.

5 J. Wang, B. M. Bocko, A. J. Davenport, H. S. Isaacs, Phys. Rev. B, 46 (1992), 10321.

6 K. P. Bohnen, D. M. Kolb, Surf. Sci., 407 (1998), L629.

7 D. M. Kolb, Prog. Surf. Sci., 51 (1996), 109.

8 L. A. Kibler, M. Kleinert, R. Randler, D. M. Kolb, Surf. Sci., 443 (1999), 19.

9 J. Tang, M. Petri, L.A. Kibler, D. M. Kolb, Electrochim. Acta, 51 (2005), 125.

10 A. W. Stephenson, C. J. Baddeley, M. S. Tikhov, R. M. Lambert, Surf. Sci., 398 (1998), 172.

11 M. Baldauf, D. M. Kolb, Electrochim. Acta, 38 (1993), 2145.

12 A. M. El-Aziz, L. A. Kibler, J. Electroanal. Chem., 534 (2002), 107.

13 H. Duncan, A. Laisia, Electrochim. Acta, 52 (2007), 6195.

14 H. Naohara, S. Ye, K. Uosaki, J. Perrot. J. Electroanal. Chem.. 500 (2001), 435.

15 R. Hoyer, L.A. Kibler, D. M. Kolb, Electrochim. Acta, 49 (2003), 63.

16 L. A. Kibler, A. M. El-Aziz, D. M. Kolb, J. Mol. Catal. A-Chem., 199 (2003), 57.

17 B. Alvarez, V. Climent, A. Rodes, J. M. Feliu, J. Electroanal. Chem., 497 (2001), 125.

18 B. Alvarez, A. Berna, A. Rodes, J. M. Feliu, Surf. Sci., 573 (2004), 32.

19 E. Sibert, thesis, INPG, Grenoble (2000).

20 A. Lasia, J. Electroanal. Chem., 562 (2004), 23.

21 N. M. Markovic, T. J. Schmidt, B. N. Grgur, H. A. Gasteiger, R. J. Behm and P. N. Ross, J. Phys. Chem. B, 103 (1999), 8568.

22 A. Zolfaghari, G. Jerkiewicz, J. Electroanal. Chem. 467 (1999), 177.

23 A. J. Bard & L. R. Faulkner, Eds. D. Harris, E. Swain, E. Aiello, Electrochemical Methods: Fundamentals and Applications (2nd), New York: John Wiley & Sons, 2001, 552.

24 M. T. M. Koper, J. J. Lukkien, J. Electroanal. Chem., 485 (2000), 161.

25 L. Blum, D. A. Huckaby, N. Marzari, R. Car, J. Electroanal. Chem., 537 (2002), 7.

26 Ultra-thin Pd films electrodeposited onto Au(111): *in situ* SXRD study, in preparation

27 Y. Soldo-Olivier, M. C. Lafouresse, M. De Santis, C. Lebouin, M. de Boissieu, E. Sibert, J. Phys. Chem. C, 115 (2011), 12041.

28 J. Clavilier, J. Electroanal. Chem., 107 (1980), 211.

29 C. Lebouin, Y. Soldo-Olivier, E. Sibert, M. De Santis, F. Maillard, R. Faure, Langmuir, 25 (2009), 4251.

30 G. Jerkiewicz, Electrocatal., 1 (2010), 179.

31 A. M. El-Aziz, L. A. Kibler, J. Electroanal. Chem., 534 (2002), 107.

32 Y. Shingaya, M. Ito, J. Electroanal. Chem., 467 (1999), 299.

33 P. W. Faguy, N. S. Marinkovic, R. R. Adzic, J. Electroanal. Chem., 407 (1996), 209.

34 P. W. Faguy, N. S. Marinkovic, R. R. Adzic, Langmuir, 12 (1996), 243.

35 M. I. Volkova-Gugeshashvili, A. G. Volkov,and V. S. Markin, Russ. J. Electrochem., 42 (206), 1194.

Chapter III. Pd deposition: growth mechanisms

III.1 Introduction

Crystalline growth represents an example of phase transition, where a stable phase (the crystal) grows at the expense of a non-stable phase (gas or liquid). The driving force is the difference Δμ between the chemical potentials of the species (molecules, ions,) to be deposited (μ^d) and of the atoms in the crystal (μ^C)

$$\Delta\mu = \mu^d - \mu^C \qquad \text{Equation 1}$$

Crystallization is spontaneous when Δμ>0 (supersaturation), there is crystal evaporation for Δμ<0 and the system tends to equilibrium (no evaporation and no crystal growth) for Δμ=0.

Growth kinetic is hence a complex phenomenon as crystallisation may involve several distinct steps. Atoms coming from the gaseous (liquid) phase and arriving on the surface can be adsorbed and afterwards they can migrate on the surface (surface diffusion). After some time they can incorporate the crystal or they can be desorbed and go back to their initial phase.

Three different growth modes are experimentally observed, schematically represented in Figure III.1. They are the bi-dimensional layer-by layer growth, also known as Frank van der Merwe mode [1], the 3-dimensional growth, or Volmer-Weber mode [2] and the mixed Stranski-Krastanov mode [3], where the initial 2D growth becomes 3D beyond a certain critical thickness.

Heteroepitaxial growth is frequently pseudomorphic, which means that the deposit not only grows with a specific orientation depending on the substrate, but also with a lattice constant matched to the substrate. Since the natural lattice constants of the deposited film a_d and the substrate a_s may differ, the deposited film is in a state of strain in case of pseudomorphic growth. The misfit strain ε is

$$\varepsilon = \frac{a_d - a_s}{a_s} \qquad \text{Equation 2}$$

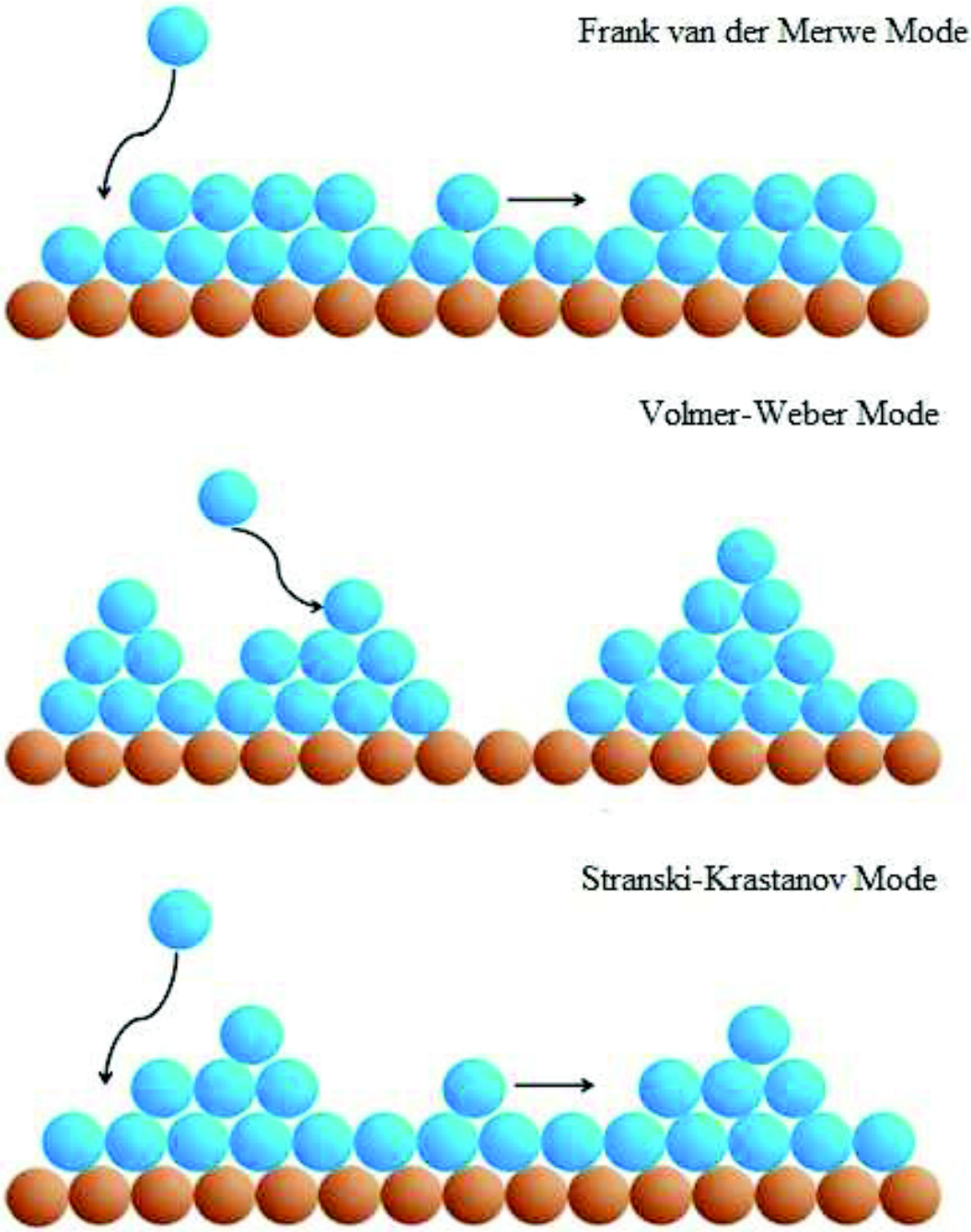

Figure III.1: Schematic representation of the Frank van der merwe, Volmer-Weber and Stranski-Kranstanov growth

Because of the misfit, the deposited film carries an elastic energy, whose behaviour as a function of the thickness determines the growth modes. For low thickness, the elastic energy stored is low enough to keep a homogeneously constraint deposited film. For higher thicknesses, the structure of the film may evolve in order to minimize the elastic

constraints and 3D islands form. After a critical thickness, t_c, the elastic energy may relax and form dislocations.

Compared to physical crystallisation, electro-crystallisation is characterized by the fact that metallic deposition is obtained at the cathode of an electrochemical cell. The concepts of chemical potential and electrostatics are now combined in order to describe the charged particles in presence of an electrical potential. The electrochemical potential μ_i^e is defined as the mechanical work done in bringing 1 mole of an ion of the *i* specie from a standard state to a specified concentration and electrical potential.

$$\mu_i^e = \mu_i^c - z_i F\Phi \qquad \text{Equation 3}$$

μ_i is the chemical potential of the *i* specie

z_i is the valence of the ion *i*

F is the Faraday constant

ϕ is the local electrostatic potential

The growth driving force is here the electrochemical over-potential. Bulk deposition occurs for lower potential than the Nernst (equilibrium) value, while at higher potential values no electrocrystallisation takes place. The exception is given by Under Potential Deposition (UPD), where one or few metallic monolayers of heteroatoms can be deposited on a metallic surface at higher potential than Nernst, as it is the case for Pd deposition on Au(111) (see chapter II).

Experimental conditions can deeply influence the growth mechanisms of deposits like the current density, the concentration in the solution of the metallic ion to be deposited, the stirring of the solution, the temperature, the pH value, presence of other cations or anions, the substrate, etc. For this reasons there is only limited theory of electro-crystallisation capable to predict the structure of the electrochemical deposit. The theory is largely based on the experimentation and it uses all the concepts developed for the physical crystallisation. Nevertheless, the problem is still more complicated in electro-crystallisation, as the diffusion of ions in solution to the electrode surface, the

electron transfer at the interface and the effect of the electric field must be here taken into account.

For the specific case of UPD of the first Pd layer, two possible mechanisms may be present. The first is an adsorption process following a Gibbs isotherm (i.e. a succession of equilibrium states). The second considers UPD as a nucleation and growth process, where deposition cannot be stopped at an intermediate coverage by selecting an appropriate potential.

Both experimental and theoretical ways have been used in order to unveil the mechanism of Pd growth on Au (111) [4,5,6,7,8]. Nevertheless the limited time resolution prevents to observe the initial nucleation and growth of Pd by classical *in situ* STM.

In this chapter we will try to have a deeper look inside the mechanisms and the kinetic of the Pd films growth, especially during the UPD step. Classical electrochemical methods and *in situ* SXRD experiments will be discussed.

III.2 Electrochemical study

As discussed in chapter II, Pd deposition on Au(111) starts with an UPD process corresponding to the deposit of one full monolayer. It is followed by an OPD process corresponding to bulk deposition. In this electrochemical study, we will focus on the very first layers deposition, trying to get more details on the elementary process and to obtain some data on the reaction kinetics.

III.2.1 CV and CA alternately applied

Figure III.2 shows the measured current as a function of the time where voltammetry (0.1 $mV \cdot sec^{-1}$) and chronoamperometry deposition are alternately applied.

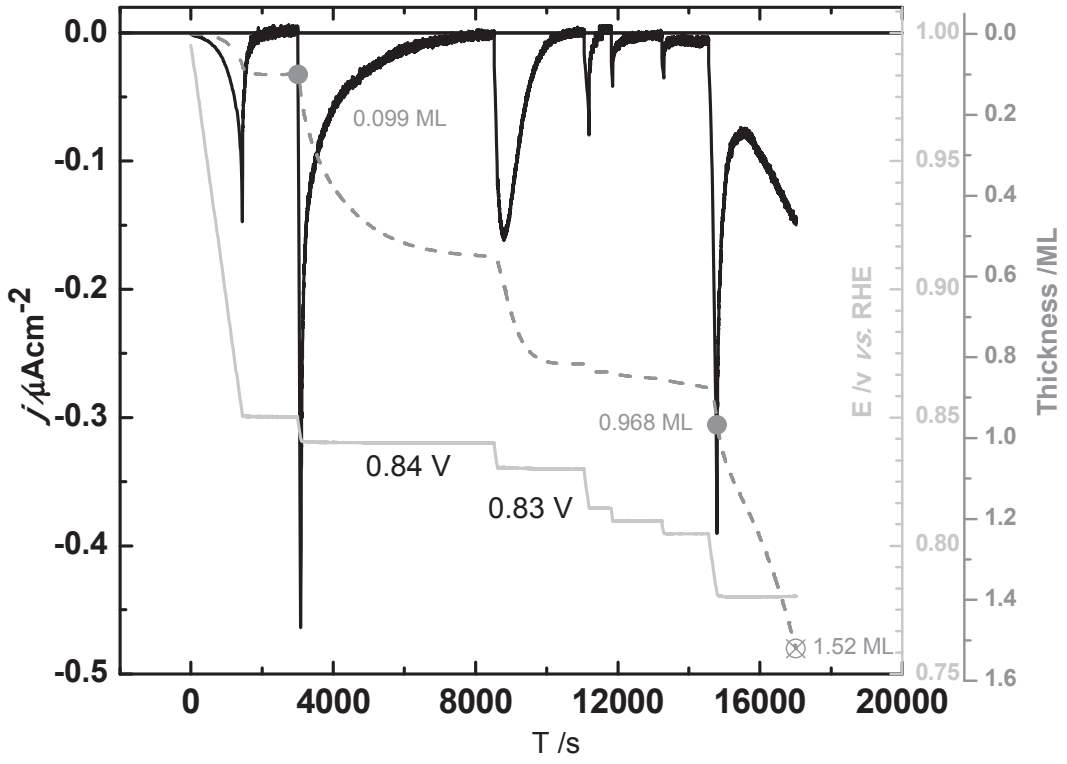

Figure III.2: Pd deposition on Au (111) in 0.1 M H_2SO_4 + 0.1 mM. $PdCl_2$ + 3 mM HCl. Current (solid line), equivalent thickness (dash line) and applied potential (grey line; scan parts at 0.1 mV·s^{-1}).

Electrode is inserted at 1.0 V *vs.* RHE, were no Pd deposition occurs. Potential is initially swept down at 0.1 mV·s^{-1}. A significant deposition current is observed during the CV, exponentially decaying during CA at 0.852 V *vs.* RHE to reach a negligible value corresponding to the stop of Pd deposition. Such finding strongly suggests that we face an adsorption process. A similar behaviour is observed during following CV down to 0.842 V *vs.* RHE and CA at this last potential value, even if current decrease during CA is slower compared to previous case. The time scale of the decay is here almost 1 hour, corresponding to a very slow kinetic, and the associated charge corresponds to about half a layer. Current behaviour is completely different during following CV and CA down to 0.832 V *vs.* RHE (Figure III.3).

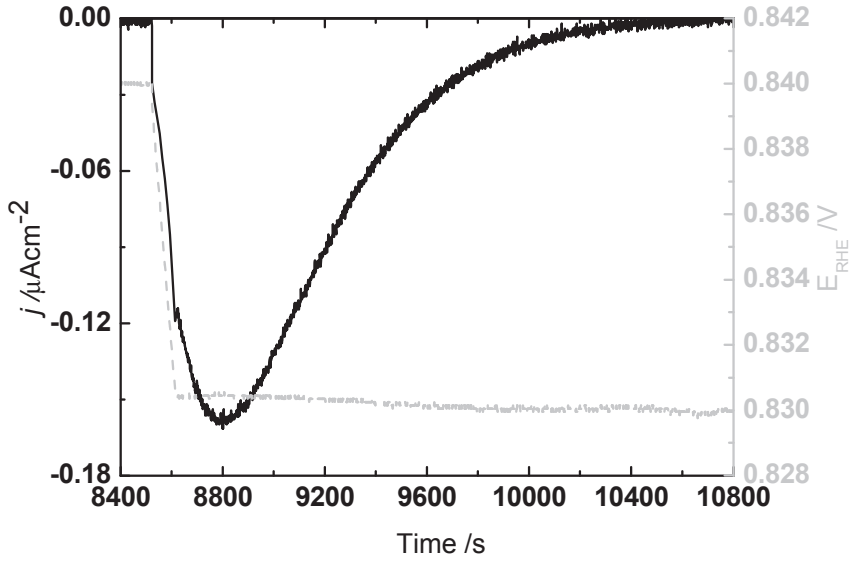

Figure III.3: Time dependence of Pd deposition current on Au(111): enlarged scale of Figure III.2 (CV from 0.84 down to 0.83 V *vs.* RHE at 0.1 mV·s $^{-1}$ and CA at 0.83 V *vs.* RHE).

The cathodic current not only increases during the potential scan, but it continues to increase during CA at 0.83 V *vs.* RHE, reaching a maximum about three minutes after CA start. Then, current decreases again and is equal to zero with a time scale of about 15 minutes. Such rising transient at constant potential is the signature of a nucleation and growth mechanism. Even if the cumulated charge since the beginning of the experiment is only equal to 370 µC·cm^{-2}, lower than the one measured with classical potential scan experiment (433 µC·cm^{-2}), it seems to be completely associated with the UPD process. Indeed, further decrease of the potential does not significantly increase deposition, until the bulk deposition starts at 0.78 V *vs.* RHE (cf. Figure II.7). The discrepancy between the two charges could arise from experimental uncertainty amplified by the long duration (3 hours) of the experiment. More interestingly, in the present experiment the UPD process is completed at a potential (0.83 V *vs.* RHE) where the deposit only starts in the classical potential scan experiment (cf. Figure II.7). Moreover, this potential seems to correspond to the pre-peak attributed by Kibler *et al.* with *in situ* STM images to Pd deposition along the steps [9]. This leads to the conclusion that the deposit only grown from the steps in the present condition. This is in opposite with the nucleation and growth mechanism. An intermediate hypothesis would be that the growth starts from punctual

defect from the Au(111) other than steps as can be seen on STM pictures by Kibler *et al.*. [9]

This initial study suggests that two different mechanisms contribute to UPD process: Pd adsorption at higher potential is followed by nucleation and growth mechanism, probably starting from substrate surface defects.

III.2.2 Current transition measurements

Instantaneous nucleation and 2D growth with nuclei overlap for UPD Pd deposition on Au (111) in 0.1 M H_2SO_4 + 0.1 mM $[PdCl_4]^{2-}$ solution was suggested by Quayum *et al.* [10] with current transient measurements. However, their model badly fits Pd growth in solution with high concentration (0.4 mM/1 mM) of $[PdCl_4]^{2-}$. Moreover, their typical time scales are surprisingly small, about 10 ms. They are not in agreement either with our measurements (Figure III.3), characterized by a time scale of several minutes, or with time scale of about 10 s measured by Kibler *et al.* [9] during Pd UPD dissolution. Even more annoying is the charge evaluation of their rising transient. Even a potential step directly in the bulk deposition potential region shows only an equivalent deposit of 0.3 ML. For purely UPD steps, a rough evaluation gives a charge of about 40 $\mu C \cdot cm^{-2}$, corresponding to only 0.1 ML of Pd on Au(111). We strongly believe that Quayum *et al.* did not actually measure the kinetic of the full Pd UPD deposition, or at least only a small fraction of process.

Also Kibler *et al.* [9] studied the kinetics of Pd deposition in 0.1 M H_2SO_4+1 mM H_2PdCl_4 solution by current transient measurement. For deposition, they only obtained an exponential decaying current which can't be fitted with nucleation and growth models. However, they observe rising transients in the dissolution of 1st Pd monolayer.

In order to further investigate initial steps of Pd deposition, we have made potential transition measurements, a well suited method to study the kinetics of electrocrystallization. Indeed, the kinetic of elementary steps is only potential dependent, as it is contrarily the case of sweep potential methods.

The theoretical aspects of the nucleation and growth mechanism will be shown before the discussion of the experimental results.

III.2.3 Theoretical description of nucleation and growth mechanism

Nucleation

The well-established Bewick-Fleischmann-Thirsk (BFT) model, initially developed for anodic film formation on mercury [11], is frequently used for nucleation and growth description. For a nucleus to evolve into a stable entity, the fluctuations in the system must be able to overcome an energy barrier, ΔG_c, corresponding to the free energy of activation for homogeneous nucleation, also called critical free energy.

In the case of a metallic monolayer deposition on a surface of the same material we have:

$$\Delta G_c = -\pi h \gamma^2 M / nF\rho\eta \qquad \text{Equation 4}$$

where *h, γ, M, n, F, ρ, η* are thickness of nuclei, molar surface energy, molar mass, valence, Faraday constant, mass density and over-potential, respectively. In the case of hetero-metallic deposition, a correction term due to the difference between molar surface energy for the two materials must be considered.

The rate of nucleation A is relied to the critical free energy through the following equation:

$$A = A' \exp(-\Delta G_c / k_B T) \qquad \text{Equation 5}$$

where *A'* is a constant, k_B is Boltzmann constant, *T* is the temperature.

The density of the nuclei *N(t)* as a function of the time is given by:

$$N(t) = N_0\left(1 - e^{-At}\right) \qquad \text{Equation 6}$$

where N_0 is the number of active sites .

For $At \ll 1$, corresponding to a slow kinetic, we have the so called progressive nucleation:

$$N(t) = N_0 At \qquad \text{Equation 7}$$

In this case only a small fraction of the possible nuclei are formed during the experiment, depending from the time.

In correspondence of a rapid kinetic, $At >> 1$, instantaneous nucleation is present, where all the possible nuclei are formed at the beginning of the potential step.

$$N(t) = N_0 \qquad \text{Equation 8}$$

Growth

Theoretical treatment of nucleation growth is dominated by geometrical considerations concerning the shape and the size of growing centers. If the rate determining step in the eletrocrystallisation process is the incorporation of atoms, the current for 2D growth is [11]:

$$I = \frac{2\pi N_0 nFMhk_g^2 t}{\rho} \exp\left(-\frac{\pi N_0 M^2 k_g^2 t^2}{\rho^2}\right) \qquad \text{(Instantaneous) Equation 9}$$

$$I = \frac{2A\pi N_0 nFMhk_g^2 t^2}{\rho} \exp\left(-\frac{A\pi N_0 M^2 k_g^2 t^3}{3\rho^2}\right) \qquad \text{(Progressive) Equation 10}$$

where k_g is the growth rate constant.

The two models exhibit a peak as a function of time, with the current maximum I_m at $t=t_m$. By using the these two coordinates obtained from Eq. 9 and Eq. 10 imposing $dI/dt(t_m)=0$, the two previous equation can be reduced to a more convenient form:

$$\frac{I}{I_m} = \frac{t}{t_m} \exp\left\{-\frac{\left[\left(\frac{t}{t_m}\right)^2 - 1\right]}{2}\right\} \qquad \text{Equation11}$$

$$\frac{I}{I_m} = \left(\frac{t}{t_m}\right)^2 \exp\left\{-\frac{2\left[\left(\frac{t}{t_m}\right)^3 - 1\right]}{3}\right\} \qquad \text{Equation 12}$$

The behaviour of the current described by the two nucleation and 2D growth models is shown in Figure III.4. The presence of a peak, typically called rising transient, is clearly seen for both descriptions, but the shapes of the two models are quite different and should be easily distinguished in experiments.

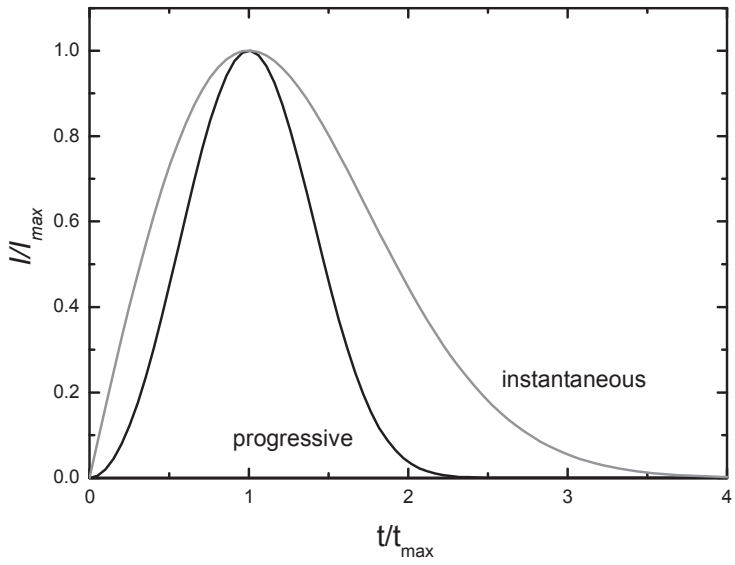

Figure III.4: The growth of monolayer by the instantaneous (grey line) and progressive (black line) nucleation mechanisms, according to Equation 11 and 12.

3D growth models also exist, but they are out of the scoop of this chapter as we are focusing on the two-dimensional UPD Pd deposition.

III.2.4 Experimental measurements

Current transition measurements are commonly used to study the kinetics under constant over-potential conditions. Typically, potential is switched from a higher value where no Pd deposition occurs down to a chosen value, which is hold during deposition. Hence in these experiments the over-potential is constant during UPD, simplifying the data analysis.

Figure III.5 shows several current transient experiments made during Pd deposition on Au (111) in 0.1 M H_2SO_4 + 0.1 mM $PdCl_2$ + 3 mM HCl; different final potential values are considered for CA measurements.

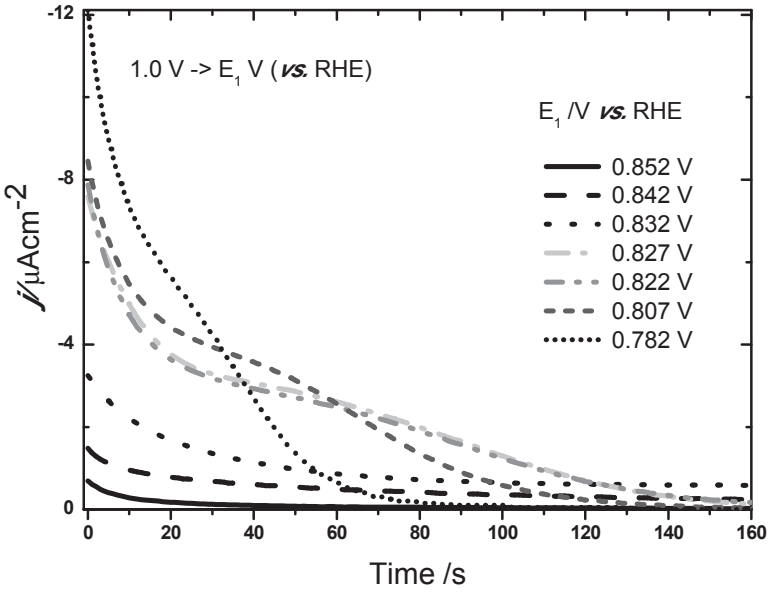

Figure III.5: Cathodic transition currents obtained during Pd deposition on Au(111) in 0.1 M H_2SO_4 + 0.1 mM $PdCl_2$ + 3 mM HCl. Each measurement corresponds to the CA obtained after the potential step from 1.0 V vs. RHE to the E_1 value.

If only a nucleation and growth mechanism were present, a current profile as described in Figure III.4 would be expected. Actually, the current decays featurelessly down to 0.832 V *vs.* RHE, while a shoulder appears at around 60 s for lower potentials. The current decay followed by a rising transient suggests the superposition of two processes. Indeed, as discussed in paragraph III.2.1, our results already suggest that UPD goes through two mechanisms, adsorption and "nucleation and growth". By the way, a model combining these two processes acting independently has already been used on Cu UPD on Au(111) [12,13].

We note that, accordingly to the studies of Holzle *et al.* [14] on Cu deposition on Au(111), the step density is a factor that can prevent to observe the rising transient peak. The presence of steps and/or defects should be considered in the Pd/Au(111) system in order to describe the weak amplitude for the observed transient current.

For instantaneous and progressive nucleation in 2D growth mode, the corresponding current densities given by equation 11 and 12 can be simplified as following:

$$j_{ins} = k_1 t \exp\left(-k_2 t^2\right) \qquad \text{Equation 13}$$

$$j_{prog} = k_1 t^2 \exp\left(-k_2 t^3\right) \qquad \text{Equation 14}$$

where k_1, k_2 are constants corresponding to reaction rate.

Following the Langmuir model, the adsorption current can be expressed as [15]:

$$j_{ads} = k_3 \exp(-k_4 t) \qquad \text{Equation 15}$$

where k_3, k_4 are constants corresponding to reaction rate.

Hence the total current densities in the case of instantaneous nucleation and progressive nucleation are respectively given by:

$$j(t) = k_1 t \exp(-k_2 t^2) + k_3 \exp(-k_4 t) \qquad \text{Equation 16}$$
$$j(t) = k_1 t^2 \exp(-k_2 t^3) + k_3 \exp(-k_4 t) \qquad \text{Equation 17}$$

Only the modelling considering adsorption and instantaneous nucleation, as described by Eq. 16, correctly reproduces the experimental data for $E_1 \leq 0.827$ V *vs.* RHE, as shown in Figure III.6.

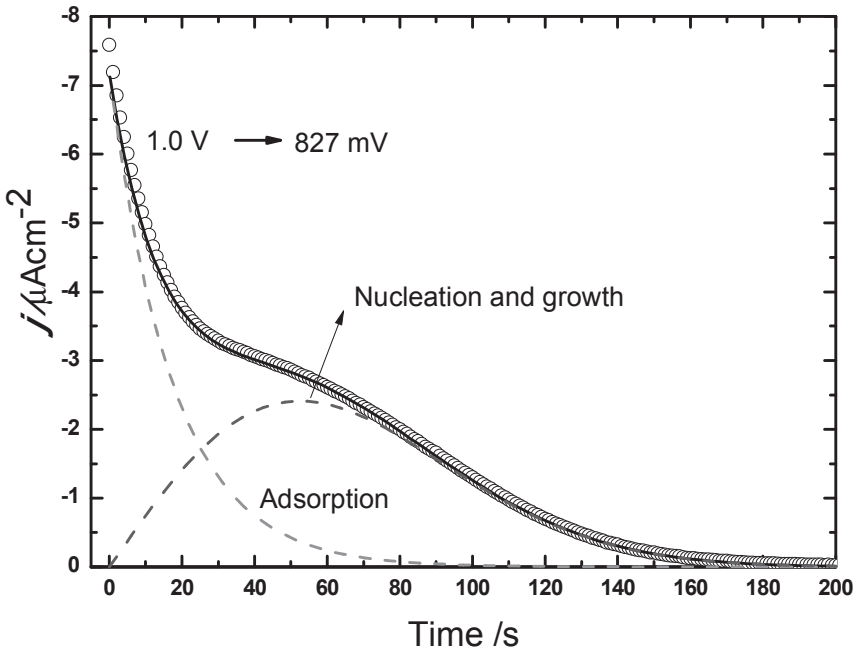

Figure III.6: Fitting procedure of the experimental transient current considering adsorption and instantaneous nucleation and growth contributions, as given by Eq. 16.

This result corresponds to the fact that a significant part of Pd deposition follows a mechanism with instantaneous nucleation and 2D growth mode in correspondence of high over-potential. For small over-potential, characterized by a small overall integral charge,

our curves confirm that nucleation and growth mechanism doesn't seem to be active, confirming the results discussed in paragraph III.2.1. In the following, we will focus on measurements with high over-potential.

Figure III.7 shows the potential dependence of constants: k_1, k_2, k_3, k_4.

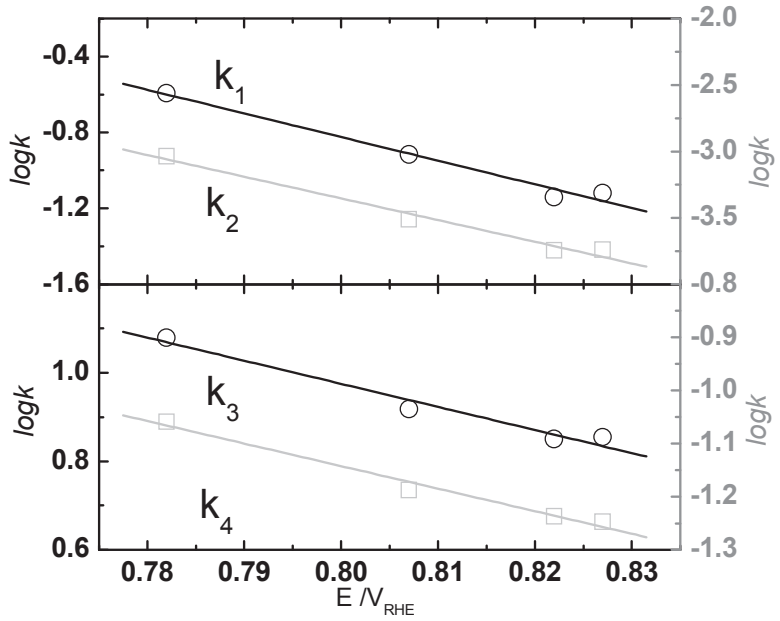

Figure III.7: Potential dependence of constants k_1-k_4.

Integrating Eq. 13 and recalling Eq. 9, we can find a relation between the constants k_1 and k_2 in the case of instantaneous nucleation and growth [12]:

$$k_1 = 2\pi nFMhN_0k_g^2 / \rho = 2k_2q_{nucl} \qquad \text{Equation 18}$$

k_g is the rate constant; q_{nucl} is the total charge in nucleation process.

From Eq. 9 we also know that [12]:

$$k_2 = \pi M^2N_0k_g^2 / \rho^2 \qquad \text{Equation 19}$$

We note that k_1, k_2 are both proportional to the square of the growth rate k_g. So Figure III.7 shows that the growth rate increases with over-potential ($k_g^2 = \rho^2k_2 / \pi M^2N_0$).

The linear relation between log(k) and E indicates the rate constant k_g can be modelled by the Butler-Volmer relation, expressing the relation between reaction constant rates and activation energy of intermediate states in absence of diffusion limitations [16]:

$$k_g = k_g^0 \exp\left[-(1-\beta)nFE/RT\right] \qquad \text{Equation 20}$$

where β is a coefficient relied to the symmetry of the energy barrier.

By substituting Eq. 19 into Eq. 20, we can get:

$$\log k_2 = a - 2(1-\beta)nFE/(RT\ln 10) \qquad \text{Equation 21}$$

Where $a = \log(\frac{\pi M^2 N_0 k_g^{0\,2}}{\rho^2})$.

By extracting the slope of logk_2 *vs.* E from Figure III.7, we can get $(1-\beta)n$ value, found to be equal to 0.484. Assuming that the energy barrier is symmetrical, i.e. β=0.5, we can get n=~0.968. This value is nearly equal to 1 and strongly suggests that the electrochemical reaction involved in the nucleation and growth only use one electron i.e. something like Pd(I) + e^- →Pd(0). Pd(I) should be an adsorbed specie in the Gibbs meaning, like a chloro-complex of Pd^+.

The slope of logk_1 and logk_2 are expected to be the same if the nucleation charge q_{nucl} doesn't depend on potential. They are actually -12.5 and -16.3, respectively. This finding is an indication that the charge q_{nucl} varies with potential.

In the same way, integrating Eq. 15, we have for k_3 and k_4:

$$k_3 = k_4 q_{ads} \qquad \text{Equation 22}$$

where q_{ads} is total charge in the adsorption process.

Again, the linear relation between log(k_4) and E (Figure III.7) suggests that the potential dependence of k_4 should follow the Butler-Volmer relation [12]:

$$k_4 = k_a^0 \exp\left[-(1-\beta)nFE/RT\right] \qquad \text{Equation 23}$$

$$\text{Or} \quad \log k_4 = b - (1-\beta)nFE/(RT\ln 10) \qquad \text{Equation 24}$$

where $b = \log(k_a^0)$.

The fitting procedure of logk_4 *vs.* E results in $(1-\beta)n = 0.251$ for Pd adsorption process on Au(111). Assuming that β=0.5, we get n=~0.502 which shows a smaller partial electron transferred during adsorption process. Nevertheless this last value is probably underestimated, as we do not actually measure all the charge relied to Pd deposition in the potential step experiments. The time resolution in our experiment is not enough to record all the charge, in particular at the potential jump where adsorption is the main process. This is shown in Figure III.8 by the comparison between the full charges recorded for deposition (potential step) and for dissolution (CV at 0.1 mV·s^{-1}).

The different slopes of logk_3 and logk_4, -5.22 and -4.24 respectively, suggests that q_{ads} depends from the potential. Moreover, these values being quite different than for "nucleation and growth" process, the kinetic evolution seems to have a different behaviour as a function of the over-potential in the two mechanisms.

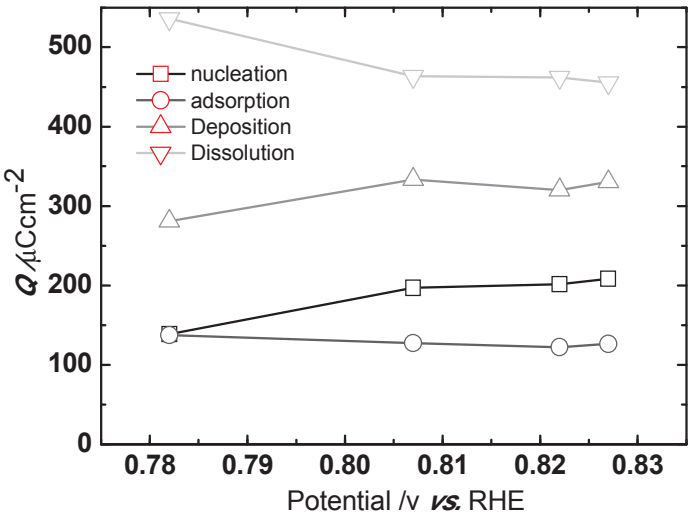

Figure III.8: Total charge measured for Pd deposition in potential step experiments (triangles up) and in dissolution obtained with CV at 0.1 mV·s^{-1} (triangles down). Calculated charge contribution in the adsorption and in the "nucleation and growth" processes derived from Eq. 18 and Eq. 22.

Figure III.8 also shows the comparison between the calculated charges associated to adsorption and to "nucleation and growth" mechanisms. At potential higher than 0.8 V *vs.* RHE, the charge associated with nucleation roughly corresponds to a full layer with a charge transfer of one electron (220 $\mu C \cdot cm^{-2}$). At 0.782 V *vs.* RHE the charge is lower by about 25%. Recalling that the "nucleation and growth" kinetic seems to faster increase with over-potential than adsorption, this finding could be relied to a kinetically limited 2D growth due to a lower concentration of adsorbed species. The real surface concentration of adsorbed species should be considered in the kinetic equation formulation.

Finally, we have shown that Pd UPD on Au(111) consists in two steps: adsorption is followed by a nucleation and growth mechanism with a constant number of nuclei. The rate constants for both adsorption and "nucleation and growth" mechanisms obey the Butler-Volmer relation and the total charge value depends from the applied potential value. The valence charge is close to one for nucleation and growth process, while its value for adsorption could not be correctly evaluated.

III.3 *In situ* SXRD

Deeper comprehension of the mechanisms underlying Pd deposition on Au(111) can be obtained with Surface X-Ray diffraction (SXRD) experiments. Indeed, close bounds exist between the structure of the deposit and the electrochemical response, as shown for Pd/Pt(111) [17,18].

III.3.1 Brief introduction on Surface X-ray diffraction

Thanks to their wavelength close to interatomic distances, X-rays represent an extremely well suited probe for indirect observation of the atomic structure of a crystal through the phenomenon of diffraction.

The amplitude of the scattered X-rays ordered by an atomic lattice is enhanced in certain directions and canceled in others, giving rise to diffraction peaks, as described by the Bragg's law:

$$n\lambda = 2d \sin\theta \qquad \text{Equation 25}$$

where *d* is the lattice spacing, θ is the incident angle, λ is the wavelength and n is an integer.

Each peak is identified by its Miller indices (*H*, *K*, *L*) and all the diffraction spots represent the reciprocal lattice associated with the direct space. Lattice parameters, cell size and type and arrangement of the atoms in the unit cell can be obtained from the positions and intensities of the diffracted peaks.

The surface of the crystal represents a symmetry break. Its contribution to the diffraction signal is represented by a non-zero intensity distribution between the volume Bragg peaks, called rods truncation (CTR, Crystal Truncation Rod), and oriented perpendicularly to the surface (Figure III.9). The crystal structure of the surface may be different from the volume: indeed relaxations in the atomic planes of extreme surface can occur. CTRs are sensitive to the surface structure and ordering in the lateral direction.

For each CTR, the diffraction index "*L*" describes the out of plane direction. The intensity on a rod varies continuously as a function of *L*, it reaches maximum for integer values of *L* at the bulk Bragg peaks, while the midway between these spots are the most sensitive to the surface structure.

The diffracted intensity from a surface is around one million times less than that from the bulk region. For this reason SXRD experiments could develop only with synchrotron radiation sources, providing the necessary brilliance for X-ray to measure the intensity diffracted from surface [19].

X-Ray diffraction using the intense and well-collimated beam from third generation synchrotron source can be used for studies of films growth [19, 20]. For homoepitaxial films, characterised by the same interplanar spacing of adlayers and substrate, the interference of the CTR scattering from the substrate with that from the overlayers gets important, since the layer spacing and the phase shift are the same. Hence, each additional layer deposited onto the surface will give rise to the same CTR, but with an additional phase shift. The resulting oscillatory behaviour of the diffraction signal is most pronounced in the anti-phase condition, corresponding to the *L* value between two Bragg peaks (anti-phase condition). Indeed, the maximum sensibility to the atomic-scale surface morphology of the crystal is between two Bragg peaks of the substrate. Changing the

scattering vector (*L* value) will affect only the amplitude of the oscillations, but not their period.

Thickness can be accurately determined from the number of observed oscillations.

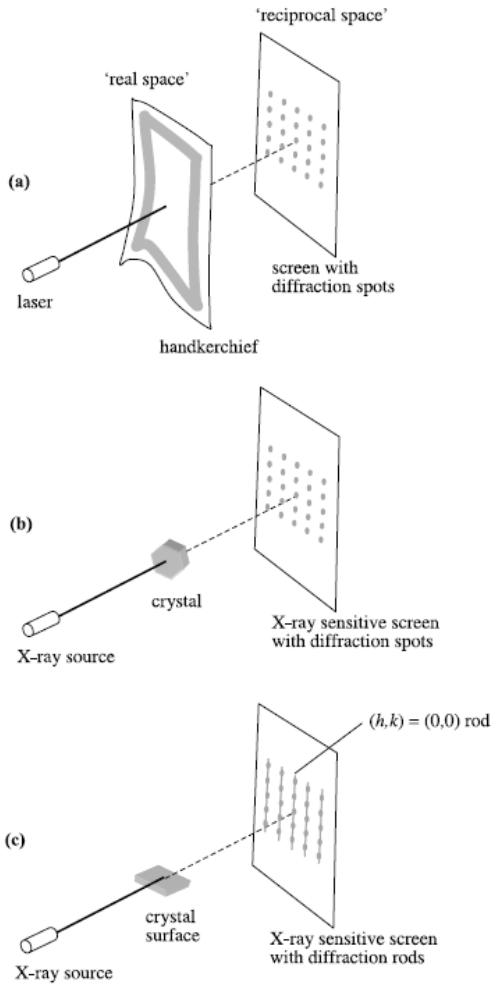

Figure III.9 [19]: Diffraction occurs when a periodic structure is illuminated by a light with a wavelength smaller than the periodic distances of the sample. Diffraction of laser light by a handkerchief (a) is analogous to the diffraction of X-rays by a crystal (b). When X-rays are diffracted by a crystal with an atomically flat surface, diffraction rods originating from the surface are visible between the Bragg peaks from the bulk (c). The central rod corresponds to specular reflectivity and is labelled (0,0).

III.3.2 Experimental procedure

Au(111) single crystal (10 mm diameter, MaTecK Jülich, Germany) with a mosaic spread of about 0.1° was flame annealed (butane/air) and cooled down in air. The quality and cleanliness of the surface were checked by cyclic voltammetry in 0.1 M H_2SO_4 like in

previous chapter. A Saturated Calomel Electrode (SCE) was used as reference electrode, even if all potentials are referred to RHE ($V_{RHE}=V_{SCE}$-0.298V in 0.1M H_2SO_4).

Pd electrochemical deposition was made in a 0.1 M H_2SO_4 + 0.1 mM $PdCl_2$ + 3 mM HCl solution in the column cell dedicated to *in situ* SXRD experiments. This cell was expressly designed and manufactured to avoid the exhaustion of reactive during the diffraction experiment. About 5 centimeters of electrolytic solution are in front of the crystal, allowing the study of Pd film initial growth (see Annex B). The experiment begins at 0.998 V *vs.* RHE, potential value corresponding to the Au(111) unreconstructed phase with a (1x1) structure. Potential is then negatively scanned down to 0.723 V *vs.* RHE at 0.1 $mV \cdot s^{-1}$ and is then maintained at this potential value, corresponding to the Pd bulk deposition region during the whole deposition process. For dissolution, potential is scanned back up to 0.998 V *vs.* RHE at 0.1 $mV \cdot s^{-1}$.

(0,1,0.5) anti-phase reflexion was recorded as a function of the time/potential during the deposition process under potential control (Biologic VSP potentiostat). As explained in the previous paragraph, the growth mode can be inferred from the anti-Bragg signal, which presents characteristic oscillations in correspondence of pseudomorphic layer-by-layer growth [21]. Experiments were performed under room temperature conditions.

III.3.3 **Results**

Figure III.10 shows the expected behaviour of the diffraction signal intensity calculated at (0,1,0.5) in anti-phase position for a layer-by-layer pseudomorphic growth from 0 to 2 ML. The simulation has been made with ROD package [22].

The signal is at its maximum value in correspondence of the bare Au(111) surface. The structure factor intensity |F| decreases with the growing of the first layer. It reaches its minimum value for 0.9 ML and increases again definitively after 1.1 ML. It reaches again its initial maximum value for 2 ML. To summarize, layer-by-layer pseudomorphic growth is described by an oscillatory behaviour of the anti-Bragg signal, with maxima or minima in correspondence of the completion of one layer.

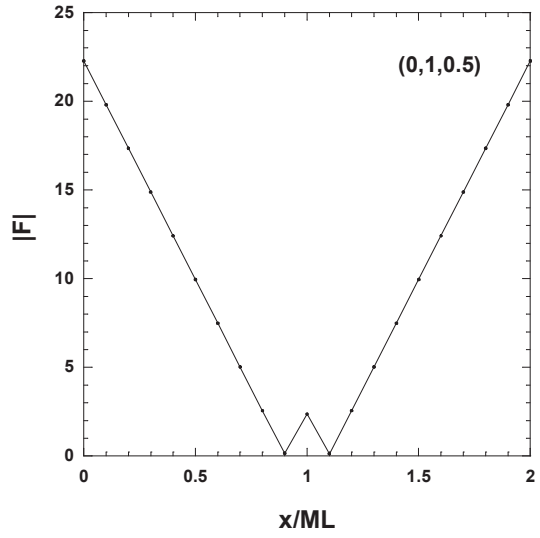

Figure III.10: $Pd_{x\ ML}$/Au(111): simulated structure factor for the (0,1,0.5) reflexion in the case of layer-by-layer pseudomorphic growth.

Figure III.11 shows the intensity evolution of the diffraction signal recorded in anti-phase position at (0,1,0.5) during Pd deposition and dissolution, as well as the applied potential.

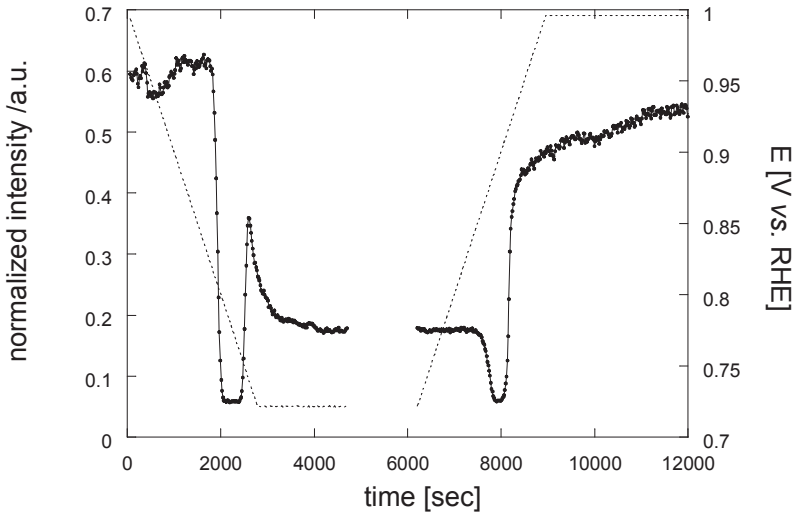

Figure III.11: *In situ* SXRD diffraction signal recorded at (1,0,0.5) during Pd deposition and dissolution in $PdCl_2$ 10^{-4} M + HCl $3 \cdot 10^{-3}$ M + H_2SO_4 0.1 M. Each point corresponds to 17 s recording. Deposition is made with potential scan from 0.998 down to 0.723 V *vs.* RHE at 0.1 $mV \cdot s^{-1}$, followed by chronoamperometry at this last value potential. Potential is maintained at 0.72n3 V *vs.* RHE till 6210 s (data have not been recorded between 4700 and 6200 s). Dissolution is made with a scan up to the initial potential value at the same rate. Continuous line with circles: normalized diffracted signal; dashed line: potential value.

At first, we remark that a layer-by-layer growth is observed for the two first deposited Pd layers, as the minimum between 2050 and 2400 seconds and the maximum at about 2600 s indicate.

The first minimum corresponds to the completion of the first Pd layer and extends over a quite large potential interval, about 77 mV. Indeed, theoretical simulation for Pd pseudomorphic growth on Au(111) indicates that this minimum is expected to extend from 0.9 ML to 1.1 ML. Hence, the large width of the minimum is due to the very low deposition speed rate. Simulation foresees that the anti-Bragg signal increases again up to its initial value in correspondence of the deposition of 2 complete monolayers. We observe such behaviour, but the signal intensity does not reach the value it had before Pd deposition, possibly due to a non-ideal layer-by-layer pseudomorphic growth up to about 2 layers.

The third layer deposition rapidly becomes three-dimensional, and the signal remains constant during all the following deposition process, corresponding to the absence of major induced relaxation for the two first layers is observed.

This description for Pd growth is confirmed by the measurements made in a point of the reciprocal space nearer to the Bragg peak, where three-dimensionally grown film contributes to the reflected beam. Figure III.12 shows the comparison of the signal at (0,1,0.5) with the measurements made at (0,1,2.09), both recorded during Pd deposition in the same experimental conditions. L is chosen at a higher value than the Bragg peak (L=2), as bulk Pd has a smaller lattice parameter (3.8907 Å) than Au (4.0782 Å). Its contribution is hence expected at higher L values than the Bragg peak.

No significant three-dimensional growth contribution is observed in correspondence of the first two layers. After the completion of the second Pd layer, the structure of Pd film rapidly evolves towards the Pd bulk one, as the increase of the (0,1,2.09) diffracted intensity indicates. These results are in complete agreement with the layer-by-layer character for the two first layers revealed by the measurements of the anti-phase signal.

Our results are in agreement with previous STM observations of Köntje *et al.* [23], who pointed out the bi-dimensional growth of Pd films (voltammetric deposition) up to 2 ML regardless of the anion in the solution. On the contrary, our findings are in contrast with

the *in situ* surface X-Rays diffraction experiments of Takahasi *et al.* [24], where Pd is deposited at fixed potential. The authors find that only the first Pd layer is pseudomorphic and the following ones are relaxed. This discrepancy underlines the strong dependence of the growth mode from the deposition conditions and in particular from the growth rate. The authors suggest that higher growth rates hinder a layer-by-layer mechanism for the Pd film deposition.

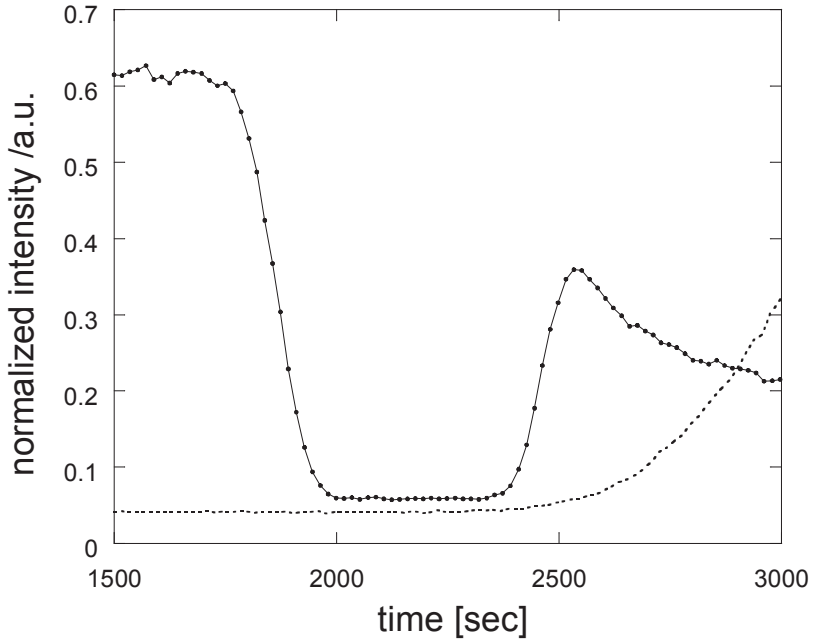

Figure III.12: Au(111) in $PdCl_2$ 10^{-4} M + HCl $3\cdot10^{-3}$ M + H_2SO_4 0.1, scan rate 0.1 mV·s^{-1}. Diffraction signal recorded at (0,1,2.09) (dotted line, Pd bulk contribution) and at (0,1,0.5) (continuous line with circles, pseudomorphic Pd layers).

Contrarily to Pd/Pt(111), where a pseudomorphic character over about 10 Pd layers was observed [25], the pseudomorphism is rapidly lost in the case of gold single crystal substrate. This finding has a main origin in the larger misfit for the Pd/Au(111) system ($\left(a_{Au}-a_{Pd}\right)/a_{Au}=0.046$) compared to Pd/Pt(111) ($\left(a_{Pt}-a_{Pd}\right)/a_{Pt}=0.0086$). Indeed, the difference in the lattice parameter of deposited pseudomorphic layers and substrate induces strain energy in the adlayers, whose value increases with the thickness of the film. Typically, the transition from coherency to incoherency for a supported epitaxial film requires the appearance of misfit dislocations at the interface above a critical thickness. Its value depends on the misfit and on several parameters of the substrate and of the overlayers (Burger vector, Poisson ratio and shear modulus) [26]: the

larger the misfit, the more important the elastic strain and the smaller the critical thickness.

Dissolution begins at 6210 s and diffracted intensity behaviour is quite different from deposition (Figure III.11). The oscillation corresponding to the dissolution of the second layer is no more present. Dissolution does not evolve layer-by-layer, but in a rough way. Only the first deposited layer is dissolved separately at a higher potential value, as shown by the oscillation at about 8000 s. Even if this peak is narrower, the signal reaches the same minimum value as during the deposition, signature of the fact that the first layer did not relax.

Diffraction intensity does not reach its initial value at the end of the dissolution process. This could be due to the presence of an alloy on the Au surface or to the a degradation of the Au(111) surface order. The present measurements cannot discriminate between these two hypotheses, as the detection of several Crystal Truncation Rods (CTRs) would be necessary for that.

III.3.4 Comparison with electrochemistry

Contrarily to the experiments made in a glass cell, the "hanging meniscus" configuration for the single crystal is not possible in the column cell used for *in situ* diffraction measurements. For this reason, the gold crystal's lateral faces give a non-negligible contribution to the current recorded during the SXRD experiment. This implies that the direct comparison between SXRD measurements and electrochemical current may not be straightforward. The comparison between the current recorded in the *in situ* SXRD cell and in a classical glass cell during the Pd deposition is shown in Figure III.13.

The contribution of the lateral poly-oriented crystal faces is present even at high potential values, before Pd deposition onto Pt(111). This observation is in agreement with theoretical DFT calculations [27] showing that the more open faces present a larger Under Potential shift. Nevertheless, the UPD peak remains clearly visible. Its position, at 0.810 V *vs.* RHE, as well as its width are the same in the two cells. The signature of the second layer deposition is also visible: the dashed line indicates the correspondence between the two measurements in correspondence of the completion of the 2nd layer.

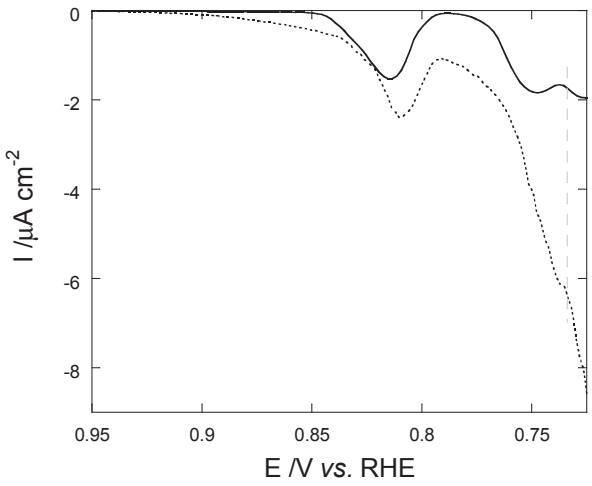

Figure III.13: Voltammetric Pd deposition in $PdCl_2$ 10^{-4} M + HCl $3 \cdot 10^{-3}$ M + H_2SO_4 0.1 M at 0.1 V·s^{-1}: comparison between currents measured in a classical glass cell in hanging meniscus configuration and in the *in situ* SXRD electrochemical cell.

Strength of this result, we compare in Figure III.14 the diffracted reflection and the electrochemical current measured in a glass cell during the Pd deposition following the same procedure used for SXRD experiment.

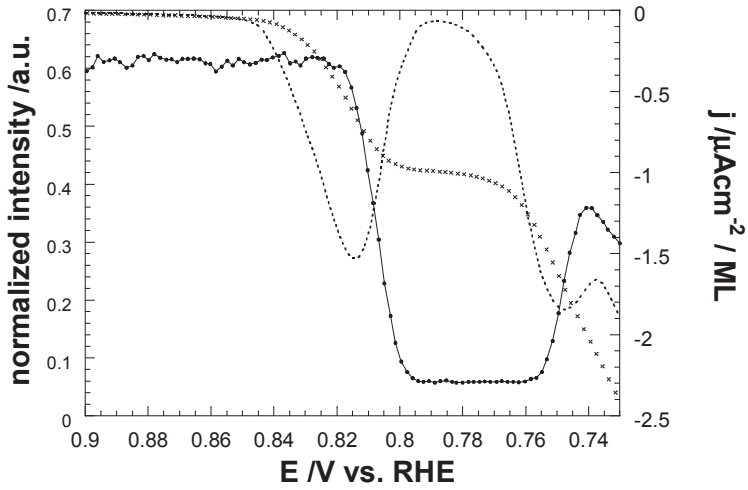

Figure III.14: Au(111) in $PdCl_2$ 10^{-4} M + HCl $3 \cdot 10^{-3}$ M + H_2SO_4 0.1 M; voltammetry scan rate: 0.1 mV·s^{-1}. Normalized diffracted signal recorded at (0,1,0.5) (continuous line with circles, 18 s measurement for each recorded point), current recorded in a glass cell (dotted line). The equivalent thickness of deposited layers is also reported (crosses): -1 for the 1st Pd ML.

The calculated number of deposited layers as a function of the applied potential is shown as well.

As expected, the completion of the first Pd layer as indicated by the UPD signal corresponds to the first minimum in the diffraction signal. As predicted by simulation, the large width of this minimum corresponds within our error bars to about 0.9-1.1 ML. This width is directly relied to the very slow deposition rate when depositing at 0.1 $mV \cdot s^{1}$. We recall that the counting time for each recorded point in SXRD experiment is 18 s, corresponding to an error on the applied potential value of 1.8 mV at the scan rate of 0.1 $mV \cdot s^{-1}$.

As there is correspondence between the two types of measurements for the completion of the first layer, as there is no agreement on the initial steps of deposition, which are recorded with a shift of about 25 mV. Even if considering the error of about 2 mV on the estimation of the applied potential, such shift is maintained. The SXRD signal begins to decrease, signature of the presence of pseudomorphic deposited palladium, only when the electrochemical charge already corresponds to about 0.3 ML.

A similar behaviour has been described during Ge deposition in UHV onto Ge(111) by Vlieg *et al.* [28],who noticed a delay between Ge effective deposition and decrease of the SXRD signal. The authors suggest that the first arriving atoms are not located at lattice positions and a partly crystalline overlayer is formed only after continued deposition.

Following this reasoning, a first explanation of the observed time-shift could be the fact that, at low coverage rates, the Pd atoms diffuse on the Au(111) surface before reaching the final equilibrium site, such as defects, steps, …. Indeed, we already pointed out that Pd UPD undergoes a first adsorption step, preceding at least for the first fraction of layer “nucleation and growth” mechanism. Such adsorbed Pd(+I) specie likely diffuses on the surface, in agreement with the observed shift between SXRD and electrochemical recordings.

Such behaviour is not observed for the second layer deposition, which could be hence ascribed to a different diffusion coefficient of Pd on Au and on Pd. The influence of the substrate and of the anions on the Pd mobility has been evoked by Tang *et al.* [29]. In their *in situ* STM measurements the mobility of Pd atoms seems higher for Pd on Pd compared

to Pd on Au in presence of adsorbed [$PdCl_4^-$], which is in agreement with our observations.

III.3.5 UPD deposition with "step" procedure

In order to better investigate the UPD mechanisms, we followed the Pd film growth recording the diffraction reflexion at different potential values, going from one value down to the next one by sweeping at 0.1 mV·s^{-1}. Rocking scan measurements at (0,1,0.5) were made at least 3 minutes after reaching the selected potential value, in order to allow the system to reach equilibrium. Following this procedure, we recorded the diffracted signal at 0.998, 0.833, 0.818, 0.813, 0.808 and 0.783 V *vs*. RHE.

The rocking scan obtained at 0.833 V *vs*. RHE (Figure III.15) presents a decrease of the peak signal by about 35%, confirming that Pd deposition has begun.

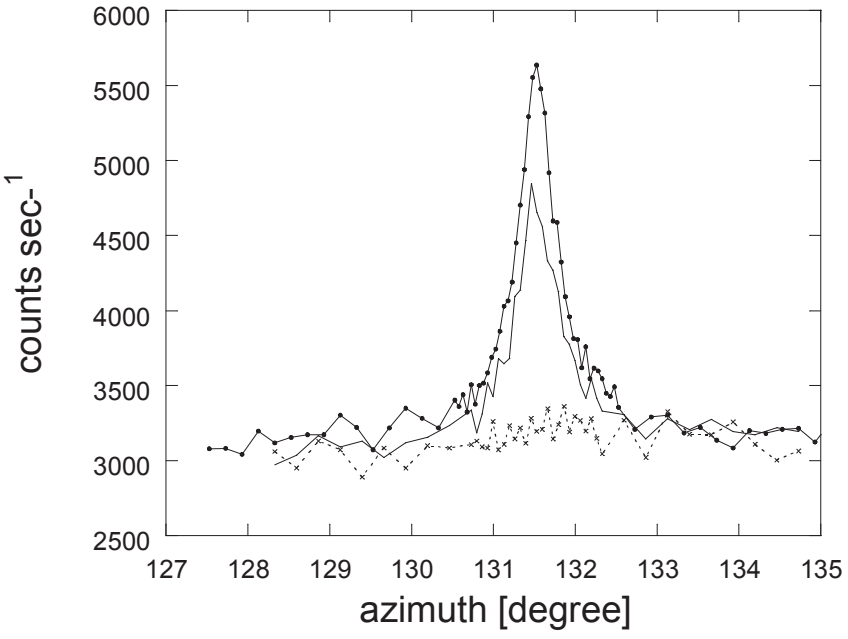

Figure III.15: Au(111) in $PdCl_2$ 10^{-4} M + HCl $3\cdot10^{-3}$ M + H_2SO_4 0.1 M. Rocking scans at (0,1,0.5) recorded at 0.998 V *vs.* RHE (circles), 0.833 V (continuous line) and 0.818 V *vs.* RHE (dashed line with crosses).

The peak completely disappears at 0.818 V *vs.* RHE. This means that at this potential a full monolayer has already been deposited, contrarily to cyclic Pd deposition with voltammetry at 0.1 mV·s^{-1} (Figure II.2) for which UPD is not completed. Such results

allow to exclude the adsorption model for Pd deposition, corresponding to a deposition rate depending from applied potential, as it is the case for hydrogen adsorption onto Pt(111) [30]. In agreement with the results previously discussed, description of Pd/Au(111) deposition must include the nucleation and growth model [10]. The irreversibility even at very low speed rates (Figure II.2) of Pd deposition/dissolution peaks is in agreement with this description.

The absence of diffraction signal is maintained lowering the potential down till 0.783 V *vs.* RHE, confirming the UPD character of the first monolayer.

The completion of the first monolayer at 0.818 V *vs.* RHE in absence of chlorides was observed with *in situ* STM by Tang *et al.* [29].

III.4 Conclusion

The growth of Pd over Au(111) in chloride containing solution is layer by layer for the first two monolayers. The third layer grows with a 3D character. The large lattice misfit between substrate and ad-layer is likely to be the main origin for the rapid loss of pseudomorphic character compared to Pd/Pt(111). SXRD measurements are in agreement with the current transient experiments, describing the Pd UPD deposition with a two steps mechanism. Adsorption of partially discharged (one electron transfer) mobile specie is followed by a complete discharge described by an instantaneous nucleation with 2D growth process. The defects likely act as nucleation centers.

Reference:

1 F. Frank, J. van der Merwe, Proc. Roy. Soc., London A, 198 (1949), 205.

2 M. Volmer, A. Weber, Z. Phys. Chem., 119 (1926), 277.

3 I. Stranski and L. Krastanov Sitz. Ber. Akad. Wiss. Wien, 146 (1938), 797.

4 H. Naohara, S. Ye, K. Uosaki, J. Phys. Chem. B, 102 (1998), 4366.

5 H. Naohara, S. Ye, K. Uosaki, J. Electroanal. Chem., 473 (1999), 2.

6 H. Naohara, S. Ye, K. Uosaki, Colloids. Surf. A, 154 (1999), 201.

7 M. Takahashi, Y. Hayashi, J. Mizuki, K. Tamura, T. Kondo, H. Naohara, K. Uosaki., Surf. Sci., 461 (2000), 213.

8 L. A. Kibler, M. Kleinert, D. M. Kolb., Surf. Sci., 461 (2000), 155.

9 L. A. Kibler, M. Kleinert, R. Randler, D. M. Kolb, Surf. Sci., 443 (1999), 19.

10 M. E. Quayum, S. Ye, K. Uosaki, J. Electroanal. Chem., 520 (2002), 126.

11 A. Bewick, M. Fleischmann and H. R. Thirsk, Trans. Faraday. Soc., 58 (1962), 2200.

12 M. H. Holzle, U. Retter, D. M. Kolb, J. Electroanal. Chem., 371 (1994), 101.

13 A. Martinez-Ruiz, M. Palomar-Pardave, J. Valenzula-Benavides, M. H. Farias, N. Batina, J. Phys. Chem. B, 107 (2003), 11660.

14 M. H. Holzle, V. Zwing, D. M. Kolb, Electrochim. Acta, 40 (1995), 1237.

15 R. D. Armstrong, J. A. Harrison, J. Electrochem. Soc., 116 (1969), 328.

16 A. J. Bard & L. R. Faulkner, Eds. D. Harris, E. Swain, E. Aiello, Electrochemical Methods: Fundamentals and Applications (2nd), New York: John Wiley & Sons, 2001, 110.

17 C. Lebouin, Y. Soldo-Olivier, E. Sibert, M. De Santis, F. Maillard, R .Faure, Langmuir, 25 (2009), 4251.

18 Y. Soldo-Olivier, M. C. Lafouresse, M. De Santis, C. Lebouin, M. de Boissieu, E. Sibert, J. Phys. Chem. C, 115 (2011), 12041.

19 E. Vlieg, Surf. Sci., 500 (2002), 458.

20 E. Weschke, C. Schüßler-Langeheine, R. Meier, and G. Kaindl, C. Sutter, D. Abernathy, and G. Grübel, Phys. Rev. Lett., 79 (1997) 3954.

21 K. Krug, J. Styettner, O. Magnussen, Phys. Rev. Lett., 96 (2006), 246101.

22 E.Vlieg, J. Appl. Crystallogr., 33 (2000), 401.

23 C. Köntje, L.A. Kibler, D. M. Kolb, Electrochim. Acta, 54 (2009), 3830.

24 M. Takahasi, K. Tamura, J. Mizuki, T. Kondo and K. Uosaki, J. Phys.: Condens. Matter., 22 (2010), 474002.

25 C. Lebouin, Y. Soldo-Olivier, E. Siber, P. Millet, M. Maret, R. Faure, J. Electroanal. Chem., 626 (2009), 59.

26 J. W. Matthews, Epitaxial Growth, J. W. Matthews, Academic, New York (1975), Chap. 8.

27 E. P. M. Leiva, Electrochimica. Acta, 41 (1996), 2185.

28 E. Vlieg, A.W. Denier van der Gon, J. F. van der Veen, Phys. Rev. Lett., 61 (1998), 2241.

29 J. Tang, M. Petri, L. A. Kibler and D. M. Kolb, Electrochim. Acta, 51 (2005), 125.

30 G. Jerkiewicz, Electrocatal., 1 (2010), 197.

Chapter IV. Electrochemical isotherms of the H-$Pd_{x\ ML}$/Au(111) system

Our overall aim is to study the effect of several parameters in the hydrogen insertion in Pd. We are mostly focusing on Pd nanofilms deposited on several well-defined substrates and especially on Au(111) for the present work. Even in this particular case, we may observe several behaviors for different film thicknesses. Hydrogen insertion isotherm is a useful tool for such studies. In gas phase, it describes the quantity of hydrogen inserted in Pd as a function of the applied H_2 pressure. It is usually expressed as an atomic ratio between hydrogen and palladium: H/Pd. It is temperature sensitive. In electrochemical environment, H_2 pressure is replaced by electrochemical potential. Hydrogen electro-insertion presents numerous advantages, like the lower cost of the electrochemical equipment, time-saving for the faster current-voltage response and avoiding the safety problem caused by high pressure [1]. Thanks to a well-established relation between the electrochemical potential and the equivalent hydrogen partial pressure [1] it is possible to deduce from the electrochemical isotherm the corresponding gas phase one [2] (see annex A). We have measured static isotherms, where every measured point corresponds to an equilibrium state of the H-Pd system at that potential.

We will start with an overview of the behaviour of Pd nanofilms on Au(111) in acidic solution in order to identify which features can be used for isotherm determination.

Figure IV.1 shows the electrochemical cyclic voltamperometry of a $Pd_{10\ ML}$/Au(111) film in 0.1 M H_2SO_4.

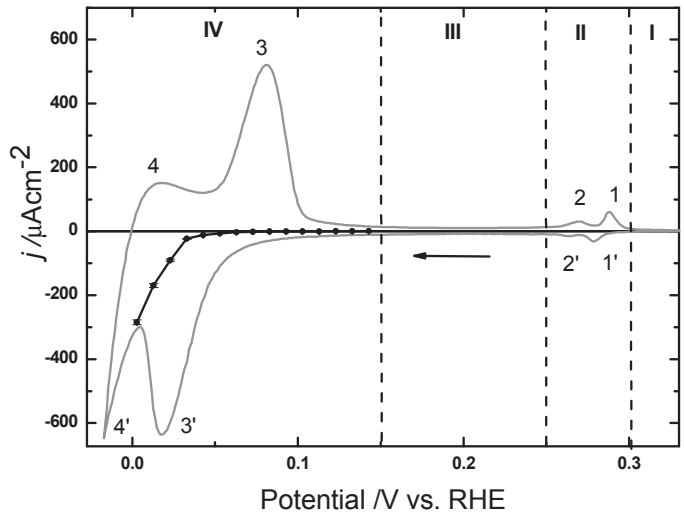

Figure IV.11: Cyclic voltammetry of $Pd_{10\ ML}$/Au(111) in 0.1 M H_2SO_4. Sweep rate: 10 mV·s^{-1}. Evaluation of hydrogen evolution is also presented (Close circles with black line), corresponding to the measured equilibrium current as a function of the applied potential.

Four regions can be identified, even if they are not separated by strict boundaries.

I. Double layer zone. Current is here totally capacitive.

II. Hydrogen/sulphate sorption/desorption region. As discussed in chapter II, this zone is dominated by hydrogen adsorption/desorption and (bi)-sulphate desorption/adsorption reactions on the second Pd adlayer (peaks 1/1') and on the following layers (peaks 2/2') .

III. As the measured current value is independent from the thickness of the Pd film, we consider that this region is dominated by hydrogen adsorption/desorption reactions.

$$Pd + H^+ + e^- \leftrightarrow Pd - H_{ads}$$

It is described by the Frumkin adsorption isotherm, based on the model of repulsive interactions between adsorbed atoms [3].

IV. Hydrogen absorption/desorption zone. Two possible paths are described in the literature for these reactions:

indirect way

$$Pd + H^+ + e^- \leftrightarrow Pd - H_{ads}$$

$$Pd - H_{ads} \leftrightarrow Pd - H_{abs}$$

direct way

$$Pd + H^+ + e^- \leftrightarrow Pd - H_{abs}$$

It is important to underline that hydrogen evolution reaction (HER) superimposes to hydrogen insertion process at the lowest potential values. Hydrogen gas is generated through Heyrovsky reaction [4,5]:

$$Pd - H_{ads} + H^+ + e^- \leftrightarrow Pd + H_2$$

or Tafel reaction [4, 5]

$$2Pd - H_{ads} \leftrightarrow Pd + H_2$$

In order to estimate the contribution of HER, current has been recorded for various potentials at equilibrium state, where the only faradic reaction is hydrogen evolution (see Figure IV.1). Current value is nearly zero above 0.02 V *vs.* RHE, indicating that in this potential region hydrogen evolution process is negligible. This is not the case for lower potentials, where HER contribution must be considered. Following this description, peaks 4/4' are mainly due to HER/HOR (hydrogen oxidation reaction) and peaks 3'/3 can be mainly attributed to hydrogen insertion/desorption. While peak 3' is clearly convoluted with peak 4', hydrogen desorption peak 3 is shifted to a higher potential range, where hydrogen evolution can be neglected. For this reason the positive scan curve can be better used for evaluation of the quantity of absorbed hydrogen.

Finally, the potential range considered for isotherm measurements is from 0.153 V *vs.* RHE to 0 V *vs.* RHE. We still cannot exclude some hydrogen adsorption in the same potential range. It may marginally affect H/Pd ratio calculation, especially for thin Pd deposits.

Absorption and desorption branches have been measured for various Pd film thicknesses and compared to bulk Pd, Pd/Pt(111) and Pt nanoparticles.

IV.1 Experimental procedure

IV.1.1 Insertion electrochemical isotherm

Figure IV.2 schematically shows the procedure followed to determine the quantity of hydrogen atoms absorbed as a function of the applied potential.

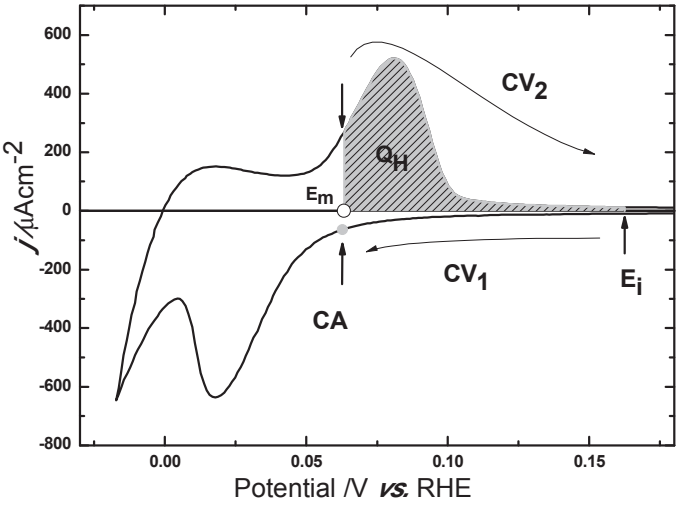

Figure IV.12: Schematic representation of the procedure followed to measure the hydrogen isotherm's absorption branch, 0.1 M H_2SO_4. Scan rate is 10 mV·s^{-1} for voltammetry.

After electrochemical characterization in 0.1 M H_2SO_4 in the region [0.1, 0.4] V *vs.* RHE, the potential is initially fixed in the hydrogen adsorption region, E_i=0.15 V *vs.* RHE. It is then negatively scanned down (CV_1) to the considered insertion potential for isotherm measurements, E_m, and it is maintained (CA) until steady state is reached.

The charge corresponding to the desorbed hydrogen is evaluated by the integral charge Q_H under the anodic curve CV_2 where each transferred electron corresponds to one inserted hydrogen atom:

$$Q_H = \int_{E_m}^{E_i} \frac{i}{\nu} dE \qquad \text{Equation 1}$$

Figure IV.3 shows typical anodic scans curves obtained for absorption isotherm calculation.

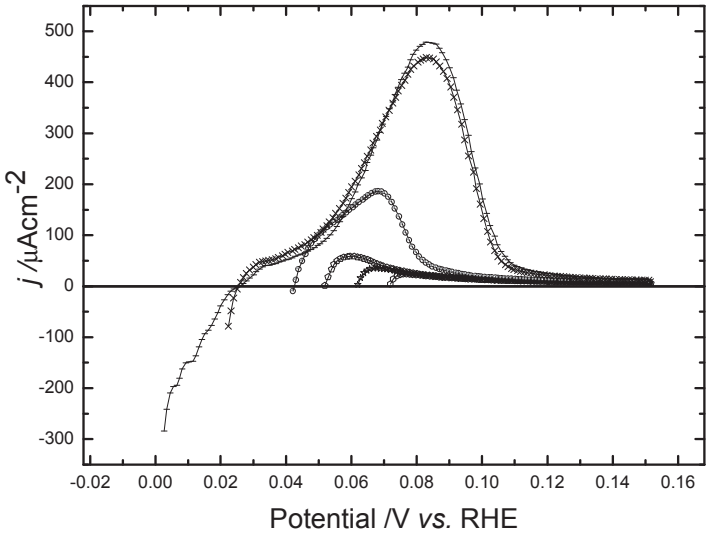

Figure IV.13: Absorption isotherm calculation: anodic scans measured for Pd$_{15\ ML}$/Au(111), 10 mV·s^{-1}.

As already discussed, hydrogen evolution current plays a more and more important role as potential decreases lower than about 0.02 V *vs.* RHE. Its contribution is shown in Figure IV.1 by negative current values. In order to consider only the charge due to hydrogen insertion process, only the positive current domain has been considered in the calculation of Q_H following Eq. 1.

The number of Pd atoms is evaluated by the deposition charge Q_{Pd}, where two electrons are exchanged for each deposited Pd atom, and hydrogen insertion rate at the potential value E_m is obtained applying the following equation:

$$(H/Pd)_{Em} = \frac{2 * Q_H}{Q_{Pd}} \qquad \text{Equation 2}$$

We recall here that 444.4 $\mu C \cdot cm^{-2}$ is the equivalent charge for 1 full Pd monolayer on Au(111).

Experimental points for isotherm determination are measured each 10 mV. In order to minimize interference of hydrogen gas, electrolyte was stirred during the measurements [6]. Experiments were performed under room temperature conditions.

IV.1.2 Desorption electrochemical isotherm

We recall that there are two branches in a hydrogen isotherm, absorption and desorption branch, respectively (Chapter I.4). For the measurement of desorption branch, the potential, initially fixed in the hydrogen adsorption zone, is negatively scanned down to E_F=-0.02 V *vs.* RHE (CV_1), value below which any further insertion can be considered as negligible. After equilibrium is reached (CA_1), potential is positively scanned up (CV_2) to the considered insertion potential E_m, where it is maintained until steady-state (CA_2). Q_H is evaluated as shown Figure IV.4 and calculation of hydrogen insertion rate is made by applying Eq. 2.

The points of the desorption branch are measured each 10 mV from the lowest potential E_F up to 0.15 V *vs.* RHE. As for hydrogen insertion isotherm, electrolyte was stirred during all the measurements. Experiments were performed under room temperature conditions.

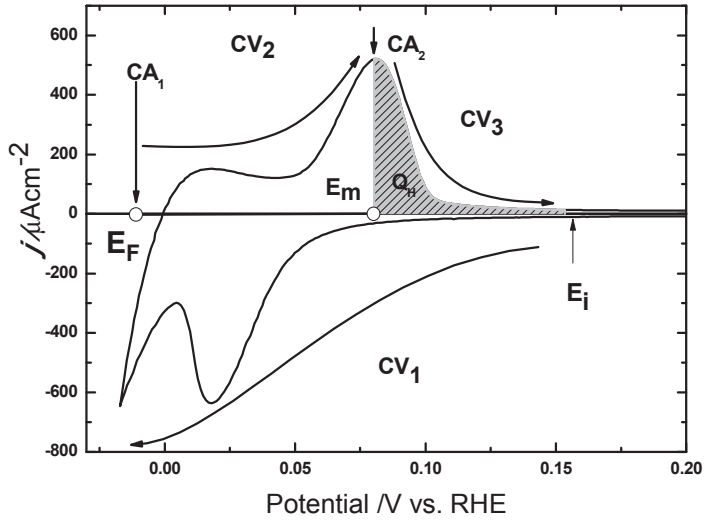

Figure IV.14: Schematic representation of the procedure followed to measure the hydrogen isotherm's desorption branch. Scan rate is 10 mV·s^{-1} for voltammetry.

IV.2 Results and discussion

IV.2.1 Pd$_{15ML}$/Au(111): hydrogen isotherm

Figure IV.5 shows the complete hydrogen isotherm of one Pd$_{15\ ML}$/Au(111) sample.

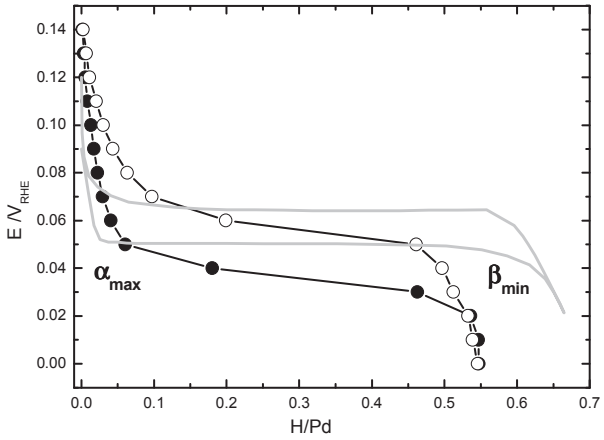

Figure IV.15: Hydrogen electrochemical isotherm of one sample Pd$_{15\ ML}$/Au(111), 0.1 M H_2SO_4. Full circles: absorption branch; open circles: desorption branch; light grey line: bulk Pd isotherm [7].

Compared to bulk Pd, Pd film isotherm still presents the two-phase plateau, but it is narrower and is characterized by a slope. Hydrogen storage capacity is smaller, $(H/Pd)_{max} \approx 0.55$. These same characteristics have been found in the H-Pd/Pt(111) isotherms and have been attributed to the constraints induced by the substrate [7,8], which induce the presence of non-equivalent insertion sites. Within this description, α_{max} and β_{min} values are not as clearly defined as for bulk Pd. Indeed, boundaries between the different regions (α zone, two-phase domain, β zone) are probably not well marked in Pd supported films, as the analogy with the Pd/Pt(111) behavior suggests, and α_{max} and β_{min} parameters do not probably have the same meaning as for bulk Pd. For this reason we will only describe their trend as a function of the various parameters (support, thickness,…), but we will not give any quantitative value. As Figure IV.5 shows, α_{max} seems to be larger for $Pd_{15\ ML}$/Au(111), corresponding to an enlargement of the α phase in Pd/Au(111) nano-films.

Isotherm clearly shows the presence of hysteresis between insertion and desorption branches. Measurements on thinner films show that hysteresis is present down to 5 ML equivalent thickness films. This finding supports the idea that hysteresis does not depend on thickness. Our results are in agreement with Pundt *et al.* [9], who showed the presence of hysteresis in the isotherm measured in gas phase on 3 nm sized Pd nanoparticles.

IV.2.2 **Influence of the thickness on hydrogen solubility**

Figure IV.6 shows the comparison among insertion isotherms obtained for various samples thicknesses. Hydrogen insertion rates in isotherms correspond to the mean value among several samples with the same equivalent thickness. Error bars are given by the standard deviation. As it has be shown in chapter III, only the two first adlayers grow bi-dimensionally, while following layers are characterized by 3D growth. This induces a worst reproducibility of the film's local morphology with thickness increasing, giving significantly bigger error bars for the thickest samples (10 ML and 15 ML).

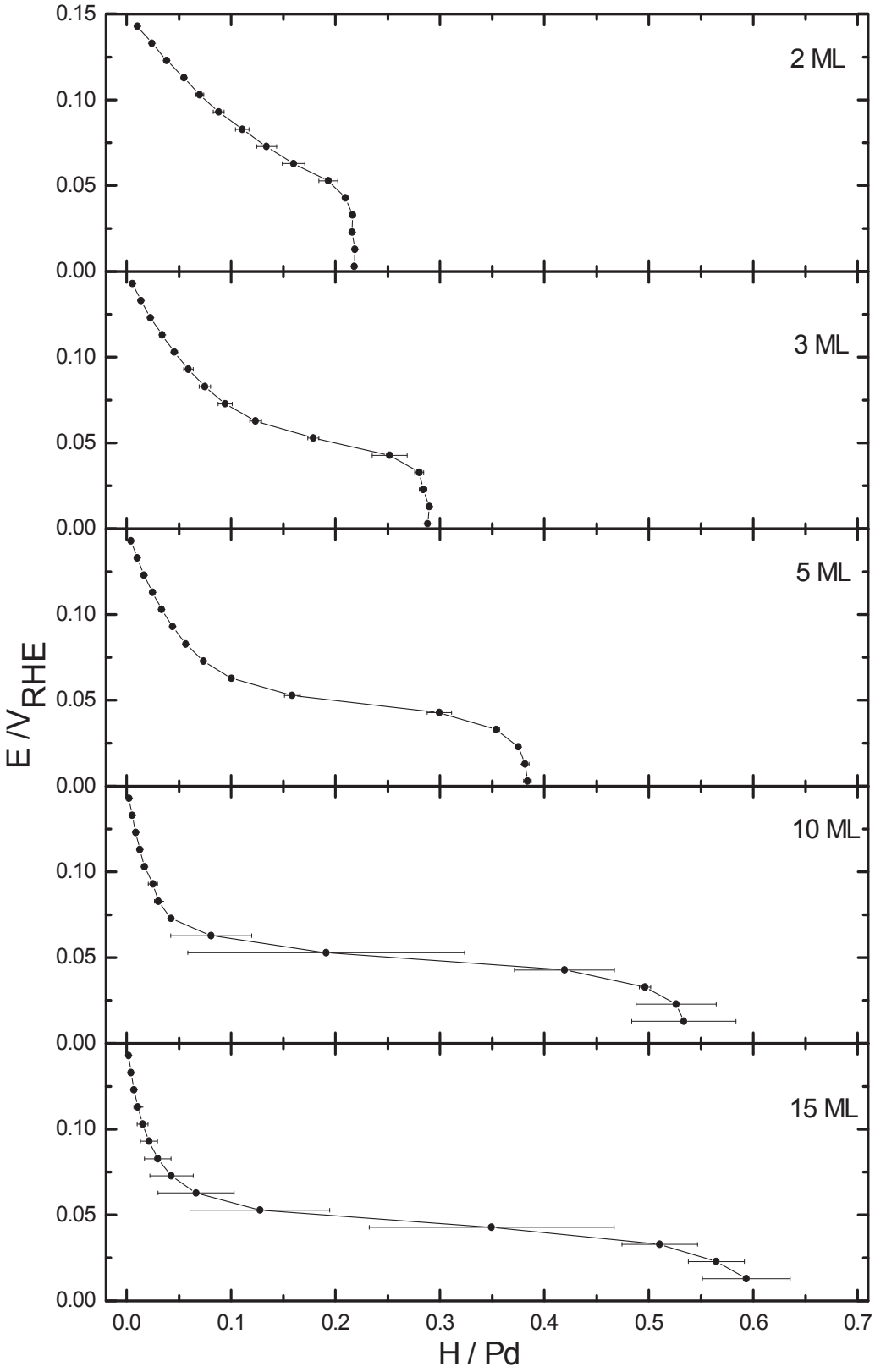

Figure IV.16: Electrochemical insertion isotherms for Pd$_{x\ ML}$/Au(111) films, 0.1 M H_2SO_4.

Maximum solubility $(H/Pd)_{max}$ is deeply modified by the thickness of the film, decreasing by about a factor three from 15 ML down to 2 ML (cf. Figure IV.7). It's value is closer to Pd bulk [10] for the thickest film, while it is about 0.2 for P_{2ML}/Au(111). These results show that the substrate plays a main role, its influence being stronger the smaller the thickness of the film.

In opposite to Pd/Pt(111), hydrogen insertion is observed even for 2 ML.

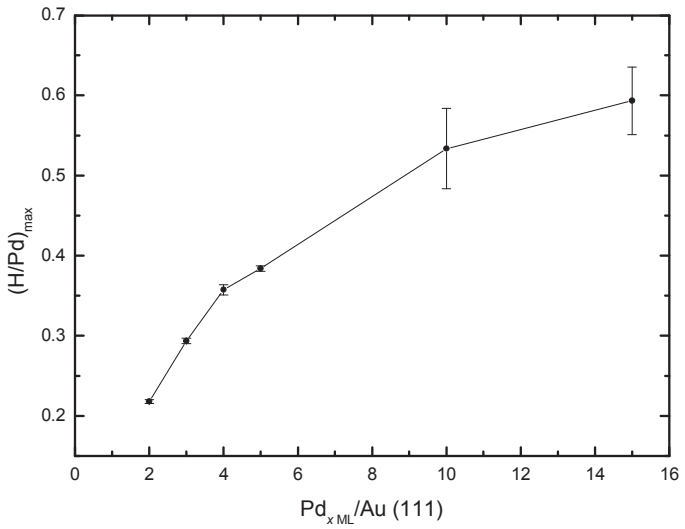

Figure IV.17: Maximum hydrogen insertion rate $(H/Pd)_{max}$ as a function of Pd/Au(111) film thickness.

The two-phase plateau width decreases with thickness and completely disappears for $Pd_{2\ ML}$/Au(111). Its slope behaves the opposite, being the most pronounced for the thinnest Pd film. This observation confirms the fact that the slope is mainly due to the effect of the substrate: the thinner the film, the bigger the crystalline support influence.

As discussed in previous paragraph, α_{max} and β_{min} values are not as well defined as for Pd bulk and the difficulty in determining a unique value for these parameters increases with decreasing of thickness. For 2 ML they are not defined at all, as well as the plateau disappears. Nevertheless, isotherms seem to show that α_{max} and β_{min} values tend to increase and decrease, respectively, with thickness decreasing.

We also remark that the isotherm for Pd$_{2\ ML}$/Au(111) does not exhibit any plateau, recalling the behaviour of AuPd alloy [11,12]. This finding suggests the formation of an alloy at the surface, even if we cannot definitely conclude about that.

In the next paragraphs we will show that the comparisons with the results obtained for Pd/Pt(111) nano-films and for non-supported Pd nanoparticles allow a deeper understanding of Pd/Au(111) isotherms behavior.

IV.2.3 Comparison with Pd/Pt(111) nano-films

Figure IV.8 shows the comparison of hydrogen insertion in Pd film with equivalent thicknesses on Au(111) and Pt(111):

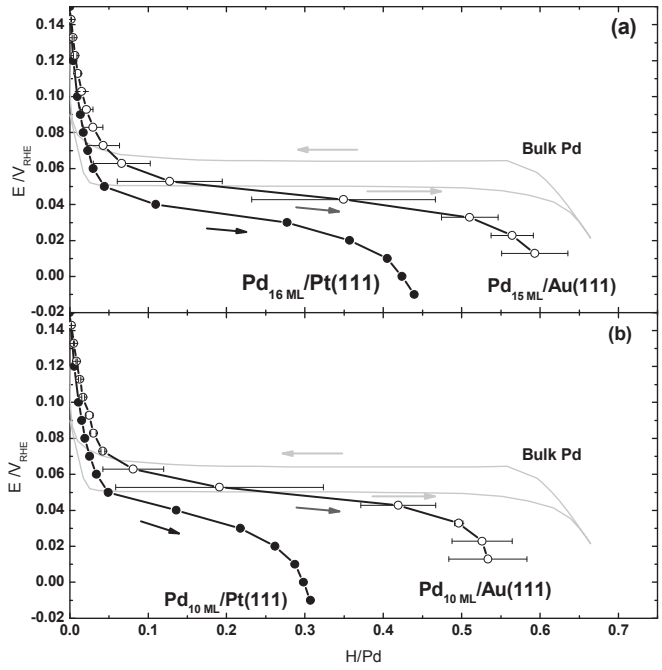

Figure IV.18: H insertion isotherms of Pd bulk [1] (continuous light grey line), Pd$_{x\ ML}$/Au(111) (open circles) and Pd$_{x\ ML}$/Pt(111) [7] (close circles) for about 15 ML (a) and 10 ML (b) as equivalent thickness.

We observe three important changes. First, the total hydrogen solubility is higher in Pd/Au(111) compared to Pd/Pt(111). Second, the slope of the plateau is much smaller. Lastly, the hydrogen insertion occurs at higher potential. Due to this higher potential, we were able to measure hydrogen insertion in Pd/Au(111) down to 2 ML without strong perturbation by HER, in opposite to Pd/Pt(111) where HER completely hide hydrogen insertion for thicknesses lower than 10 ML.

The substrate certainly plays a key role in the observed isotherms behavior. Geometric and ligand effects modifying adsorption processes have already been theoretically predicted [13]. In particular, Roudgar *et al.* made a theoretical study on H adsorption onto Pd flat layers on Au(111) and Au(100) [14]. As far as we know, no theoretical work has been done on substrate effect on hydrogen insertion in Pd films.

Indeed, a quite different structure for Pd/Pt(111) [8] and Pd/Au(111) films (see chapter III) has been revealed by SXRD. The influence of the Pt(111) substrate on the structure of the deposited Pd film extends over a quite high number of layers; Pd deposits are quite flat independently of the thickness of the film and begin to relax only beyond the about 10 first pseudomorphic layers. The influence of the substrate undergoing a gradient over a large number of layers, and inducing an important fraction of non-equivalent hydrogen insertion sites, may largely contribute to the accentuated slope of the plateau for Pd/Pt(111). On the contrary, Au(111) substrate effect is rapidly quenched down with thickness. Pd films on Au(111) grow layer-by-layer only for the two first adlayers. The third layer growth becomes 3-dimensional with relaxation of the inter-atomic distances.

Morphology, and particularly the thickness of the constraint region, seems to have an important effect also on the hydrogen insertion rate, especially with the decrease of the thickness. Moreover, the lattice parameters of the two metals, support and Pd adlayers, are very close in the case of platinum, with a misfit $(a_{Pt} - a_{Pd}) / a_{Pt} = 0.0086$, while this is not the case for Au, $(a_{Au} - a_{Pd}) / a_{Au} = 0.046$. This results in the fact that Pd

pseudomorphic first adlayers are more expanded in the in-plane direction on Au(111) than on Pt(111), probably contributing to the different isotherm behavior in the two systems.

The maximum hydrogen insertion rate for thicker deposits is the combination of bulk like and constraints layers contributions. Pd/Au(111) deposits tending more rapidly to bulk Pd behavior with thickness increase, this may contribute to explain the higher $(H/Pd)_{max}$, as well as the higher insertion potential and the smaller plateau slope.

IV.2.4 Nano-size effects

As previous paragraphs have shown, supported Pd films are characterized by properties that may significantly differ from bulk materials. In order to try to separate substrate and nano-size effects on the films' thermodynamic properties, it is interesting to make a comparison with non-supported nanoparticles.

Figure IV.9 shows the isotherms of different Pd systems: Pd bulk, non-supported commercial Pd nano-particles [1] and Pd thin films deposited on single crystals.

It must be remarked that hydrogen diffusion lengths in palladium supported films (15 ML equivalent thickness) and in nano-particles (mean size 3.6 nm) are in close ranges of order, allowing a direct comparison of their isotherms. Adsorption contribution to the isotherm is not negligible in the case of palladium nanoparticles (surface effect), but hydrogen chemisorptions can't be separated from absorption in gas-phase experiments. Thus to compare the isotherms of the two nanosystems (film and nanoparticles), we had to re-calibrate the insertion branch for the nanofilms including hydrogen adsorption charge.

Compared to bulk Pd, both Pd nano-systems (films and nanoparticles) are characterized by a smaller $(H/Pd)_{max}$ value and a narrower two-phase region. Beyond the different values for $(H/Pd)_{max}$, which have been discussed in the previous paragraph, the

slope in the plateau is presented for both supported films, while it is absent for non-supported nano-particles. This finding confirms that this isotherm's behavior is due to the constraints induced by the substrate and not by the nanometric size of the system, as it has been discussed by Soldo *et al.* [8] for hydrogen insertion into Pd/Pt(111).

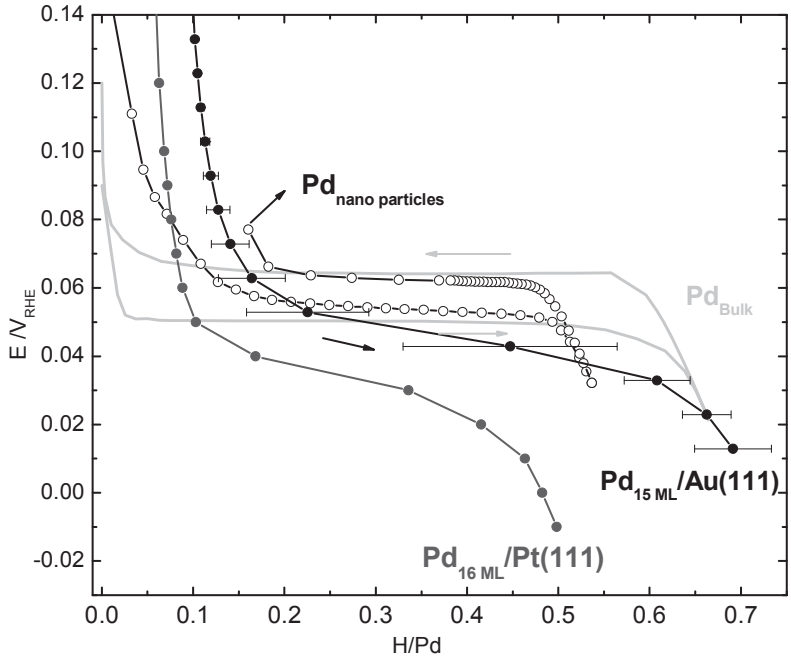

Figure IV.19: H isotherms for bulk Pd, non-supported Pd nanoparticles (mean size 3.6 nm) [7, 15] and Pd nanofilms, $Pd_{15\ ML}$/Au(111) and $Pd_{16\ ML}$/Pt (111)[a].

IV.2.5 Ageing of the samples

Bulk Pd undergoes irreversible structural modifications after hydrogen insertion/desorption cycles. This is attributed to the large misfit between Pd lattice parameter and the β phase, characterized by an expansion of about 3.5%. It is interesting to verify if such behavior is still observed in thin supported Pd films, where the nano-size may modify the effect of hydrogen insertion/desorption cycling (ageing) on the samples morphology. Figure IV.10 shows the result of aging experiment, where the insertion

[a] Nano-particles and films isotherms include the contribution of hydrogen adsorption.

isotherms measurements are repeated several times on two different films: Pd$_{7\ ML}$/Au(111) and Pd$_{10\ ML}$/Au(111).

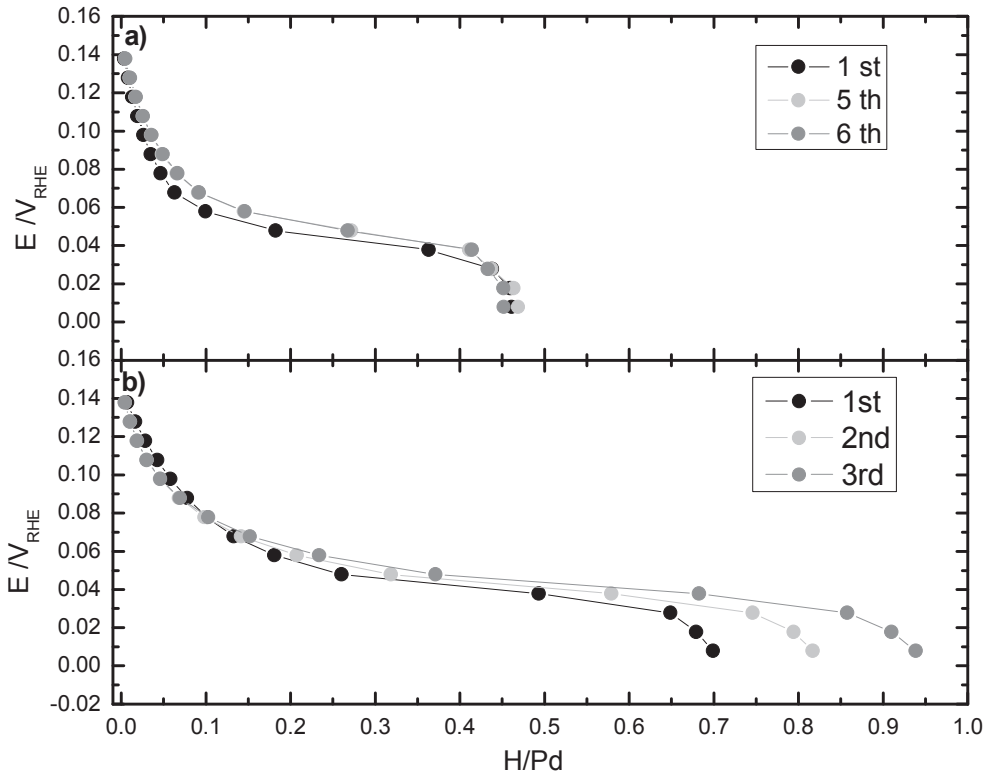

Figure IV.20: Absorption branches of H electrochemical isotherms in 0.1 M H_2SO_4 during ageing experiment on a) Pd$_{7\ ML}$/Au(111); b) Pd$_{10\ ML}$/Au(111).

Hydrogen insertion isotherms reveal that the Pd film undergoes a structural modification upon hydrogen insertion/desorption cycling. With ageing, α_{max} slightly increases and the potential corresponding to the two-phase zone is higher. Physical characterization of the film should be made, in order to establish a direct link with the film's structural evolution. In particular, the eventual formation of a surface alloy Pd-Au should be checked, as similar behavior has been observed in alloyed electrodes. In particular, potentiostatic techniques applied on Ag-Pd[b] alloyed electrodes during the

[b] Silver and gold lattice parameters are very close (a_{Ag}=4.0853Å, a_{Au}=4.09Å)

absorption of hydrogen from aqueous solution show that α_{max} increases and hydrogen maximum solubility decreases with silver content [16].

We remark that the effect of ageing procedure increases with thickness. While $Pd_{7\ ML}$/Au(111) isotherms seems to be slightly affected, α_{max} and H/Pd_{max} significantly vary with ageing for the higher thickness, eg. 10 ML.

We believe that this behavior finds a major explanation in the way substrate induced constraints extend over the film layers. As explained in the previous paragraph, substrate influence rapidly decreases for Pd/Au(111), Pd films becoming more and more rough and relaxed (3D growth) with thickness. They rapidly present Pd bulk behavior, showing upon ageing irreversible morphological deformation, beyond elastic range.

IV.3 Conclusions

We obtained electrochemical isotherms of Pd/Au(111) films for various thicknesses, from 2 ML up to 15 ML.

Compared to bulk Pd, maximum insertion rate is smaller even for the thickest film $Pd_{15\ ML}$/Au(111) and isotherm presents a sloped two-phase region. We could highlight the influence of the film thickness on the thermodynamic parameters. $(H/Pd)_{max}$ decreases by about a factor three from 15 ML down to 2 ML. The two-phase plateau width diminishes and completely disappears for $Pd_{2\ ML}$/Au(111), while its slope behaves the opposite, being the most pronounced for the thinnest Pd film.

Compared to Pd/Pt(111) films with the same thickness, isotherm more rapidly bulk Pd like behavior, with hydrogen insertion at higher potential, higher $(H/Pd)_{max}$ values and smaller slope of the two-phase plateau. According to the results for Pd/Pt(111) films discussed in the thesis of Chrystelle Lebouin, these findings are mainly relied to substrate's effects and they are very different between gold and platinum. Geometric and electronic effects must be considered to take into account for higher hydrogen absorption ability and larger two-phase region in Pd/Au(111) isotherms compared to Pd/Pt(111). In

particular, $(H/Pd)_{max}$ not only depends on the nanometric size of the system, but also on its morphology and in particular on the constraint 2D or relaxed 3D atomic arrangement.

The comparison with non-supported Pd nanoparticles confirms that the slope is mainly due to the substrate induced constraints, which result in non-equivalent absorption sites.

The presence of hysteresis between insertion and desorption branches for $Pd_{15\ ML}$/Au(111) supports the idea that hysteresis does not depend on thickness, at least down to this thickness.

Hydrogen insertion/desorption cycling on Pd/Au(111) films cause irreversible inelastic deformations inducing isotherm's evolution with ageing, this phenomenon worsening with thickness.

Reference:

1 S. Bliznakov, E. Lefterova, N. Dimitrov, Int. J. Hydrogen Energ., 33 (2008), 5789.

2 I. Jain, M. Abu Dakka, Int. J. Hydrogen Energ., 27 (2002), 395.

3 M. Eriksson, I. Lundström, L. G. Ekedahl, J. Appl. Phys. 82 (1997) 3143.

4 M. Enyo, T. Maoka, Surf. Technol., 4(1976), 277.

5 M. Bhardwaj, Int. J. Hydrogen Energ., 34(2009), 1655.

6 L. Birry, A. Lasia, Electrochim. Acta, 51 (2006), 3356.

7 C. Lebouin, Y. Soldo-Olivier, E. Sibert, P. Millet, M. Maret, R. Faure, J. Electroanal. Chem., 626 (2009), 59.

8 Y. Soldo-Olivier, M. C. Lafouresse, M. De Santis, C. Lebouin, M. de Boissieu, E. Sibert, J. Phys. Chem. C, 115 (2011), 12041.

9 A. Pundt, M. Suleiman, C. Bähtz, M.T. Reetz, R. Kirchheim, N.M. Jisrawi, Mater. Sci. Eng. B, 108 (2004), 19.

10 M. Baldauf, D. M. Kolb, Electrochim. Acta, 38 (1993), 2145.

11 A. Sieverts, E. Jurisch and A. Metz, Z. Anorg. Chem., 92 (1915), 329.

12 F. A. Lewis, Platinum Metals Rev., 5 (1961), 21.

13 J. R. Kitchin, J. K. Nørskov, M. A. Barteau, and J. G. Chen, Phys. Rev. Lett., 93 (2004), 156801.

14 A. Roudgar, A. Groβ, J. Electroanal. Chem. 548 (2003),121.

15 C. Lebouin, Y. Soldo-Olivier, E. Sibert, M. De Santis, F. Maillard, R .Faure, Langmuir, 25 (2009), 4251.

16 A. C. Makrides, J. Phys. Chem., 68 (1964), 2160.

Chapter V. Summary and outlook

V.1 Summary

Ultra-thin films of palladium deposited on a mono-crystalline surface represent an interesting model to study the palladium properties towards the insertion/removal of hydrogen at the nano-scale, which may reveal specific properties compared to solid palladium samples. Such deposits may also present a mono-crystalline character, allowing the elimination of grain boundaries and thus short-circuit diffusion paths.

The present study deals with the elaboration and characterization of Pd films on Au(111) and the electro-insertion of hydrogen.

Well-defined signatures for each deposition step have been obtained for Pd deposition experiment. Electrochemical characterizations of the films in 0.1 M H_2SO_4 show a huge effect of the scan rate. Only scan rates lower than about 1 $mV \cdot s^{-1}$ allow to evidence and correctly separate the several features of the voltammetry. We could successfully ascribe the various peaks to specific reactions. Adsorption/desorption and reorganization reactions have been highlighted on the first Pd layer, on the free surface of the 2nd Pd monolayer and on the 3rd and following almost relaxed layers. The evolution of the electrochemical characterization with thickness is in agreement with the fact that the growth is pseudomorphic up to the second layer, with the 3rd layer growth beginning before the completion of the 2nd layer. The attribution of the various peaks is in complete agreement with the structural model proposed by in situ SXRD characterization of the films, where the strong 3D growth beyond the second pseudomorphic layer is characterized by huge “towers” leaving unchanged the ratio of free second layer surface at least up to 10 ML. The large lattice misfit between substrate and ad-layer is likely to be the main origin for the rapid loss of pseudomorphic character compared to Pd/Pt(111).

As shown by current transient measurements, Pd UPD deposition seems to follow a two steps mechanism: adsorption with partial discharge with one electron transfer followed by an instantaneous nucleation and 2D growth. Such model is in agreement with in situ SXRD and electrochemical results.

We obtained electrochemical isotherms of Pd/Au(111) films for various thicknesses, from 2 ML up to 15 ML. Compared to bulk Pd, maximum insertion rate is smaller even for the thickest film $Pd_{15\ ML}$/Au(111) and isotherm presents a sloped two-phase region. Our results confirm the presence of hydrogen insertion into $Pd_{2\ ML}$/Au(111). We could highlight the influence of the film thickness on the thermodynamic parameters. $(H/Pd)_{max}$ decreases by about a factor three from 15 ML down to 2 ML. The two-phase plateau width diminishes and completely disappears for $Pd_{2\ ML}$/Au(111), while its slope behaves the opposite, being the most pronounced for the thinnest Pd film.

Compared to Pd/Pt(111) films with the same thickness, isotherm more rapidly approaches a bulk Pd like behavior, with hydrogen insertion at higher potential, higher $(H/Pd)_{max}$ values and smaller slope of the two-phase plateau. The comparison with non-supported Pd nanoparticles confirms that the slope is mainly due to the substrate induced constraints, which result in non-equivalent absorption sites. The substrate's effects have been underlined, being very different between gold and platinum. The presence of hysteresis between insertion and desorption branches for $Pd_{15\ ML}$/Au(111) supports the idea that hysteresis does not depend on thickness, at least down to this thickness.

Hydrogen insertion/desorption cycling on Pd/Au(111) films cause irreversible inelastic deformations inducing isotherm's evolution with ageing, this phenomenon worsening with thickness.

V.2 Outlook

The work described in this Ph. D thesis contributes to better comprehension of the Pd growth modes, with a deeper comprehension of the electrochemical deposition and characterization of the deposited surface, as well as original properties of electrochemical isotherm. However, there still remain challenges in this field.

- It is a challenge to completely understand the voltammetric profile for the Pd/Au(111) films in sulfate solution due to the complicated interactions among adsorbents. CO displacement and Infrared experiments are suggested for further investigation.

- In the potentiostatic transient measurement, it is still a challenge to record all the current of initial adsorption process due to the time resolution limitation. This could be solved by the advancement of potentiostat technology.

- It is interesting to determine the temperature dependence of H-$Pd_{x\ ML}$/Au(111) system by electrochemical methods. Physical characterization of Pd film in the hydrogen absorption/desorption cycle also can be done by *in situ* SXRD since we ascribe the evolution of isotherm to film deformation in hydrogen absorption/desorption cycle.

Annex: A

Relation between electrochemical and gas-phase hydrogen isotherms

According to the literature [1], thermodynamic parameters of material can be derived from their electrochemical PCT isotherm too. First, the enthalpy change ΔH and entropy change ΔS during the hydrogen absorption/desorption is corresponding to the logarithm of hydrogen absorption/desorption pressure by the van't Hoff relation:

$$\ln[\frac{p(H_2)}{p^0}] = \frac{\Delta H}{RT} - \frac{\Delta S}{R} \qquad \text{Equation 1}$$

Where $p(H_2)$ is the equilibrium hydrogen pressure of transition from α phase (solid–solution phase) to β phase (hydride phase), which determined from the mid-plateau values [1] of the PCT isotherms, p_0 is the standard pressure, R is the universal gas constant and T is the temperature. The hydrogen absorption/desorption PCT isotherms in the gas/solid-phase system at different temperatures could be plotted by kinds of experimentally methods, such as volumetric or gravimetric techniques [1]. Then the pressure logarithm can be plotted as a function of the reciprocal value of the temperature (van't Hoff plots), hence the enthalpy and the entropy of hydride formation/decomposition can be derived from the slope and intersect of the accordingly obtained linear.

Second, only potential-composition-temperature isotherm is registered by electrochemical technique, it is presented as hydrogen charging/discharging curves in different temperature. However, the electrode potential (E) measured in solution and equilibrium pressure $p(H_2)$ measured in gas phase has a strong thermodynamic correlation according to Nernst equation.

As it is known, there are two ways for hydrogen insertion into Pd: indirect way and direct way [2,3]. They are represented by reaction (1) and (2) respectively.

$$Pd + H^+ + e^- \leftrightarrow Pd - H_{ads} \leftrightarrow Pd - H_{abs} \qquad \text{reaction 1}$$

$$Pd + H^+ + e^- \leftrightarrow Pd - H_{abs} \qquad \text{reaction 2}$$

For simplification, we consider following reaction only.

$$H^+(aq) + e^- \leftrightarrow H_{abs} \qquad \text{reaction 3}$$

If the equilibrium between gaseous hydrogen and dissolved hydrogen $\underline{H_{abs}}$, can be assumed to be:

$$\frac{1}{2} H_2(gas) = H_{abs} \qquad \text{reaction 4}$$

At equilibrium, from reaction (3) and (4), we can get:

$$\mu^E_{H^+} + \mu^E_{e^-} = \mu_{H_{ads}} \qquad \text{Equation 2}$$

$$\frac{1}{2}\mu_{H_{gas}} = \mu_{H_{ads}} \qquad \text{Equation 3}$$

Respectively, where μ_A and μ^E_A are chemical potential and electrochemical potential of species A, respectively, and for non-changed species: $\mu^E_A = \mu_A$.

Combining reaction (3) and reaction (4), we have: $\frac{1}{2}\mu_{H_2} = \mu^E_{H^+} + \mu^E_{e^-}$

$$\frac{1}{2} H_2(gas) = H^+(aq) + e^- \qquad \text{reaction 5}$$

From which, we can write $\frac{1}{2}\mu_{H_2} = \mu^E_{H^+} + \mu^E_{e^-}$ Equation 4

And as we know:

$$\mu_{H_2} = \mu^0_{H_2} + RT \ln \frac{P_{H_2}}{P^0} \qquad \text{Equation 5}$$

Where P^0=1 atm. Now, we have to chose the standard for measuring electrochemical potential and chemical potential. If electrode potential is quoted against RHE, it means the solutions are the same for working electrode (WE) and reference electrode (RE). For the gas, we define that $\mu_{H_2} = 0$, when $P_{H_2} = P^0$.

$$\frac{1}{2}\mu_{H_2(RHE)} = \mu^E_{H^+(RHE)} + \mu^E_{e^-(RHE)} \qquad \text{Equation 6}$$

Because the solution are the same, thus $\mu^E_{H^+(RHE)} = \mu^E_{H^+}$, meanwhile $P_{H_2} = P^0$. From Eq. 5, we have $\mu_{H_2(RHE)} = \mu^0_{H_2}$, by substituting these equations into Eq. 6. We have:

$$\frac{1}{2}\mu^0_{H_2} = \mu^E_{H^+} + \mu^E_{e^-(RHE)} \qquad \text{Equation 7}$$

Eq. 4 – Eq. 7,

$$\mu^E_{e^-} - \mu^E_{e^-(RHE)} = \frac{RT}{2}\ln\frac{P_{H_2}}{P^0} \qquad \text{Equation 8}$$

$$\text{i.e. } -F(E_{vs\ RHE}) = \frac{RT}{2}\ln\frac{P_{H_2}}{P^0} \qquad \text{Equation 9}$$

$$\text{So } E_{vs\ RHE} = -\frac{RT}{2F}\ln\frac{P_{H_2}}{P^0} \qquad \text{Equation 10}$$

And we can get:

$$E_{vs.\ RHE} = -0.03\log\frac{P_{H_2}}{P^0} \qquad \text{Equation 11}$$

For T=298 K. According to this equation, the equilibrium potential in electrochemical PCT actually has the same means as equilibrium hydrogen pressure in volumetric measurement.

Reference:

1 L. Bozukov, A. Apostolov, T. Mudlarz, J. Magn. Magn. Mater., 83(1990), 555.

2 M. H. Martin, A. Lasia, Electrochim. Acta, 54 (2009), 5292.

3 L. Birry, A. Lasia, Electrochim. Acta, 51 (2006), 3356.

Annex: B

Schematic of electrochemical cell for *in situ* SXRD measurement

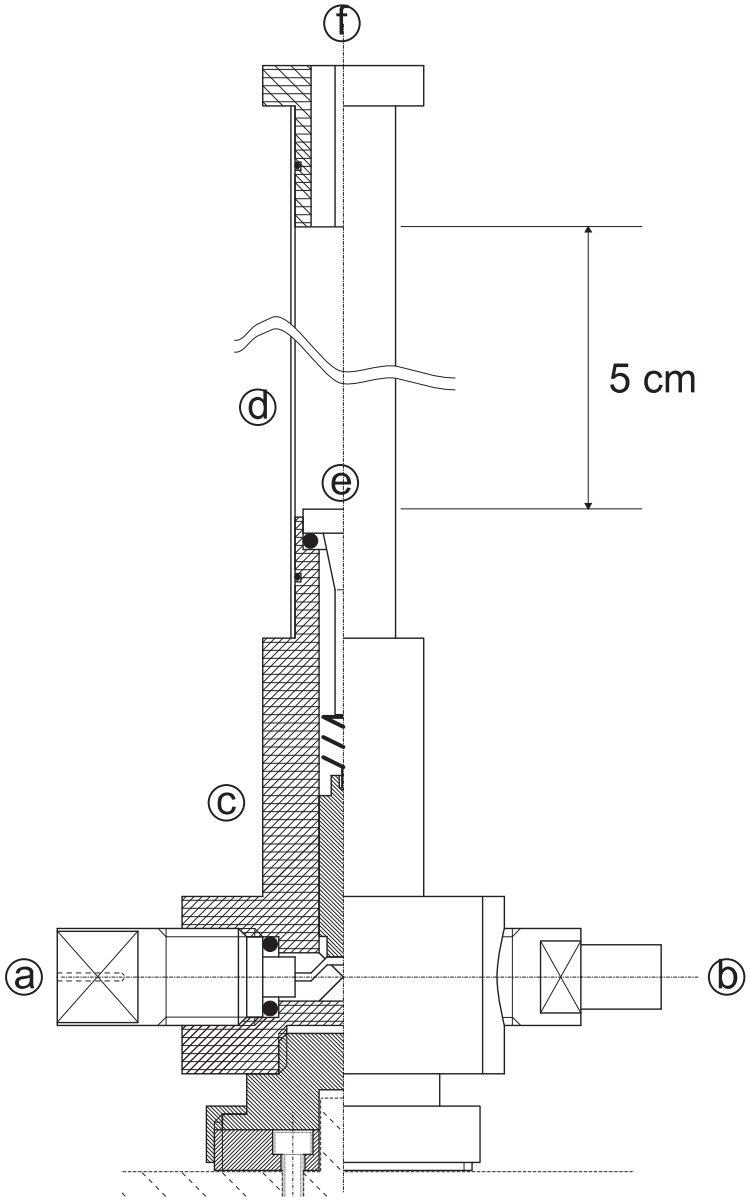

Figure A: Schematic of the electrochemical cell for *in situ* SXRD measurements. a: electrical contact; b: vacuum pumping; c: sample holder (Kel-F); d: electrochemical cell walls (Nylon cylinder); e: single crystal; f: electrochemical cell cover (Kel-F) including electrolyte inlet/outlet, counter and auxiliary electrodes.

Résumé

Ce travail de thèse s'est intéressé au dépôt électrochimique de films de palladium ultra-minces sur Au(111), à leur caractérisation et à l'insertion d'hydrogène dans ceux-ci. La caractérisation des nanofilms en milieu sulfurique montre des signatures bien définies, qui évoluent avec l'épaisseur des dépôts. Nous avons pu attribuer à chaque pic une réaction spécifique, en accord avec les mécanismes de croissance révélés par les mesures SXRD in situ. La croissance pseudomorphe de la 1ère couche se fait avec une première étape d'adsorption, suivie par un mécanisme de nucléation et croissance. La croissance 3D de la troisième couche démarre avant la fin de la deuxième couche pseudomorphe.
L'absorption d'hydrogène dans les nanofilms a été étudiée en milieu sulfurique. L'isotherme d'insertion présente un élargissement du domaine de la solution solide, un plateau avec une pente dans le domaine bi-phasique et une diminution du taux maximal d'insertion de l'hydrogène par rapport au Pd massif. Ce taux diminue avec l'épaisseur mai approche celui de Pd massif au déla delà de 15 MC. Deux éléments ont été considérés pour expliquer le comportement des isothermes: les deux premières couches pseudomorphes sont contraintes par le support et des « tours » tridimensionnelles relaxées se forment au delà de la 2ème couche.

Mots clés : dépôt électrochimique de Pd, UPD, Au(111), mécanismes de croissance, nanofilms, insertion de l'hydrogène, SXRD in situ.

Abstract

This thesis focused on electro-deposition, characterization and hydrogen strorage of ultrathin palladium film over Au(111). The electrochemical characterization of the nanofilms in sulphuric medium shows well-defined features evolving with the deposit thickness. We could assign each peak to a specific reaction, in agreement with the growth mechanisms revealed by in situ SXRD measurements. The pseudomorphic growth of the 1st layer firstly undergoes an adsorption step, followed by nucleation and growth mechanism, as shown by current transient measurements. 3D growth of the 3rd layer begins before the completion of the second pseudomorphic one.
Hydrogen absorption in the nanofilms was studied in sulphuric medium as well. Isotherms show an enlargement of the solid solution domain, a sloppy plateau in the two-phase region, a decrease of maximum insertion ratio (H/Pd)max compared to bulk Pd. This last value decreases with film thickness, approaching bulk Pd beyond about 15 ML. Two contributions were considered to explain the isotherm behaviour: the two first Pd layers heavily constraint by the substrate and the 3D "towers like" relaxed structures growing on the second pseudomorphic Pd layer.

Keywords: Pd electrochemical deposition, UPD, Au(111), growth mechanism, nanofilms, hydrogen absorption, in situ SXRD.